Growth and advanced characterization of solution-derived nanoscale $La_{0.7}Sr_{0.3}MnO_3$ heteroepitaxial systems

Jone Zabaleta Llorens

Departament de Materials Superconductors i Nanoestructuració a Gran Escala, ICMAB-CSIC
Supervisors: Prof. T. Puig Molina and Dr. N. Mestres Andreu
Tutor: Prof. A. Sánchez Moreno

Departament de Física
Programa de Ciència de Materials
Universitat Autònoma de Barcelona

Bellaterra, December 2011

Growth and advanced characterization of solution-derived nanoscale $La_{0.7}Sr_{0.3}MnO_3$ heteroepitaxial systems

Dissertation presented in candidacy for the degree of
Doctorate of Philosophy in Materials Science by

Jone Zabaleta Llorens

Departament de Física
Programa de Ciència de Materials
Universitat Autònoma de Barcelona

Departament de Materials Superconductors i Nanoestructuració a Gran Escala, ICMAB-CSIC

Supervisors: Prof. T. PUIG MOLINA and Dr. N. MESTRES ANDREU

Tutor: Prof. A. SÁNCHEZ MORENO

Bellaterra, December 2011

Para Santi y Lourdes

Contents

Acknowledgments

I would like to thank the people and institutions that have made this thesis possible.

In the first place, I give thanks to my supervisors Prof. Teresa Puig and Dr. Narcís Mestres for the opportunity given to me to realize this work, the shared discussions, and their trust in my judgment. To Prof. Teresa Puig and Prof. Xavier Obradors for inviting me to come to ICMAB and for letting me be part of the *Superconducting Materials and Large Scale Nanostructures* group.

I want to acknowledge the Spanish *Ministerio de Educación* for the FPU fellowship, as well as the Spanish Government through the CONSOLIDER program for the financial support of the last six months. I also acknowledge the EU (HIPERCHEM, NESPA, European Light Sources Activities-ELiSA), to CSIC (CANAMUS), the Spanish Government (NANOARTIS, MAT2008-01022, NANOFUNCIONA), and the Generalitat de Catalunya (XARMAE, Pla de Recerca).

I give thanks to Prof. J. Mannhart, Prof. X. Obradors, Dr. A. Asenjo, Prof. C. Ocal, and Dr. J. Santiso for accepting being part of the jury of this thesis.

This work would have not been possible without the collaboration and interaction with a good number of scientific experts in various fields:

Special thanks go to Dr. A. Asenjo and Dr. M. Jaafar, from ICMM-CSIC, who started the Magnetic Force Microscopy investigations on my systems, which I later undertook in the context of a short stay in their laboratory. Thank you very much for your willingness to teach me how to use your equipment, your care in the investigation, and for all the discussions. Thanks also to O. Iglesias-Freire for his simulations on the behavior of the magnetic nanoislands.

I am also very grateful to Prof. M. Salmeron from LBNL in Berkeley, California, for having me in his group during a short 3 month stay, and for giving me full access to the equipment for Kelvin Probe Force Microscopy measurements. I am deeply indebted to Dr. A. J. Katan, who dedicated a great amount of his time teaching me how to be autonomous in the use of the equipment. I want to acknowledge his expertise, his detailed and rigorous explanations, and his disposition to answer my (many) questions.

The TEM experts in our group, Dr. P. Abellán, Dr. F. Sandiumenge, Dr. J. Gázquez, and F. Belarre are deeply acknowledged. Prof. J. Arbiol is acknowledged for his *Rhodius* simulations. Special thanks go to P. Abellán, for the time dedicated to my samples, her enthusiasm and know-how.

To Dr. S. Valencia, Dr. F. Kronast, and Dr. J. Herrero-Albillos, I would like to give thanks for the time I spent with them in BESSY II synchrotron, Berlin, making measurements on the manganite nanoislands. Thank you very much Sergio for your feedback concerning the preparation of the experiments and the data treatment and interpretation.

I also want to acknowledge Dr. J. A. Martín Gago, and the whole group of *Structure of Nanoscopic Systems* in ICMM-CSIC for having me during a short stay at their laboratories,

and for the time devoted to XPS and STM measurements of my samples. Special thanks go to Dr. L. Martínez who later undertook the measurements and the data treatment.

Thank you Dr. C. A. Ramos and Dr. R. Zysler from the Centro Atómico-Instituto Balseiro, in Bariloche, for the ferromagnetic resonance measurements, and thanks to Dr. C. Montón, from our group, who took the initiative and leaded these experiments.

I want to deeply thank Dr. M. Stengel for his fundamental contribution in the interpretation of the KPFM results and his enlightening explanations.

I want to thank Prof. A. Sánchez and Dr. C. Navau from the UAB for coming to the rescue in the understanding of the micromagnetic behavior of the LSMO nanoislands. I hope that their theoretical efforts will be fruitful and will shed light into the experimental evidence.

Prof. C. Ocal, M. Paradinas, and C. Munuera, thanks so much for your expert advices in the use of Scanning Probe Microscopies and for your help.

Dr. J. Santiso and Dr. X. Marti are also acknowledged for the efforts done in X-rays measurements on my difficult samples.

I would like to thank all the members, former and present, of the SUMAN group, for their help and support. I thank N. Romà for teaching me, when I arrived, how the laboratories worked, and both her and Dr. S. Ricart, for their willingness to answer my chemical doubts. To M. Gibert and C. Moreno, for their great support during our AFM experiments. To Dr. A. Palau for her transport measurements and for her readiness to try new experiments. A very special thanks go to A. Crespi for the time spent with my samples trying to get as much as we could from X-rays, as well as to N. Dix, whose expertise and creativity are awe-inspiring. Thanks to C. Montón for his patient explanations on how the SQUID worked, to R. Vlad for the cerium oxide buffer layer synthesis, to V. Rodríguez for the precursor solution preparation, to B. Bozzo, and A. Pérez and N. Alonso for the magnetometry and AFM measurements, respectively; special thanks go to M. Simón from the AFM laboratory for her reliability and patience.

A special mention goes for the group secretary, P. Alvarez, for her efficiency and organizational skills.

Thank you very much, Max, for your fine comments and suggestions, and for the time devoted to them. You made me realize there is always room for improvement, and, most importantly, you made me want to pursue it.

El apoyo moral que he recibido de tanta gente del ICMAB, miembros antiguos y presentes del grupo, podría llenar muchos párrafos. Mis compañeros de despacho, César, Patricia Ab., Anna Ll., y más tarde Jaume; ha sido un verdadero placer compartir despacho con vosotros, así como tantos momentos fuera del mismo. Neus, cómo puedo agradecer tu calidez y tu sentido común, en la acepción más pura de la palabra, que es tan poco común. Mariona C., voy a echar de menos las charlas contigo y tu empuje. Todo el tiempo compartido amb la Marta G., Roberto, Markos, Mariona de P., Josh, y con mi equipo de 'spinning'; muchísimas gracias Marta V., Anna P. y Patricia Al., por tantísimas risas.

No puedo olvidar a toda la gente de fuera de la ciencia, de Bilbao y de Barcelona, que me ha apoyado tantísimo, muchas gracias a todos. Los jueves de risas con las chicas; Mai e Isa, gracias por vuestra complicidad y apoyo incondicional, ha sido una suerte teneros cerca. And you too, Bene, a breath of fresh air and a flawless, solid support.

Y por supuesto, gracias a toda mi familia, siempre tan pendiente. Sois mi mayor fortaleza. Gracias Santi, gracias aita, gracias ama.

Motivation

The boost of nanoscience and nanotechnology witnessed by this last decade has brought the discovery of new physical phenomena and the promise of a wide range of new devices and applications with real impact in fields such as medicine, industry, communications, or energy production and storage. On one hand, the downscaling of materials to nanometer sizes, while maintaining or even enhancing their performance, is imperative in the present context of, among others, energy efficiency and data storage: ultra-strong permanent magnets generated from nanosize features could, for instance, be used in lighter motors, while, the call for ultra-high density data recording can be met by effectively reducing the size of the magnetic bits. These examples belong to the field of nanomagnetism, which holds the promise to meet some of the many current worldwide scientific and technological challenges [1, 2]. The trend towards materials miniaturization is motivated, on the other hand, by the novel properties arising from geometries confined in the 10^{-7} m-10^{-9} m length, which impose new relationships between the atomic and molecular constituents. Unraveling the behavior of these small building blocks, and, ultimately, predicting new phenomena, is the essential goal of nanoscience. Nanotechnology, in turn, aims at exploiting such phenomena in real applications, which demands mastering the fabrication of nanosize materials with tuned properties, and, furthermore, it requires to do so in a controlled way, scalable and cost effective, for a real social impact to be produced.

In the context of scalability and high-throughput required for application purposes, *bottom-up* fabrication approaches offer a great potential. They are based on the spontaneous gathering of atoms and molecules, under specific growth conditions, to form more complex architectures. Ranging from organic self-assembled monolayers and supramolecular arrangements, to self-assembled metal and semiconductor nanostructures, the fabrication of many functional materials relies on this principle of 'let nature do it' [3]. Moreover, self- assembly can yield narrow size distributions of highly uniform nanostructures. This is particularly desirable in heteroepitaxial semiconductor and oxide systems, where nanostructuring is classically attained by lithography-based techniques [4, 5]. Although highly precise, these *top-down* approaches, including optical lithography and the more recent X-ray, electron-beam or Focused Ion Beam lithographies, are typically serial procedures, with costly vacuum requirements, and, often, high energies that may damage the material. A step forward towards scalability and low cost within the bottom-up strategy for nanostructure fabrication is typified by solution-based methods, still scarcely explored but with demonstrated potential [6–9].

Among the large amount of materials and combinations of materials that can be manipulated, miniaturized, or assembled to form nanoscale entities with potential functionalities, metal oxides constitute a vast and interesting family, exhibiting a myriad of properties already in the bulk state. Ferroelectric, ferromagnetic, multiferroic or superconducting

are some of the behaviors found among the large variety of metal oxides, which range from rather simple binary oxides such as Fe_3O_4, ZrO_2, TiO or ZnO, to more complex materials like ternary perovskites or spinels ($SrTiO_3$, $La_{0.7}Sr_{0.3}MnO_3$, $BiFeO_3$, $CoFe_2O_4$...), and compounds like the high-critical temperature superconductors $YBa_2Cu_3O_7$ (YBCO) or $Bi_2Sr_2Ca_2Cu_3O_{10}$ (BSCCO). The downscaling of these oxides in the form of nanometric thin films, 3D nanodots and 1D nanowires, nanocomposites, or superlattices, has shown that new and fascinating phenomena may emerge [10–15]. This fact highlights the impact of lattice strains, surface to volume ratios, interfaces, and chemical and structural defects on the physical properties of nanoscale oxide systems.

The complex mixed-valence manganese oxides (manganites) $(RE_{1-x}AE_x)MnO_3$, with RE a trivalent Rare-Earth ion and AE a divalent Alkaline Earth ion, are paradigmatic examples of how the properties of a nanostructured oxide material may differ from those of its bulk compound. In the bulk state, manganites constitute one the most fascinating families within the complex oxides, where the interrelated electric, magnetic, and structural properties give rise to intriguing phenomena such as Colossal Magneto Resistance (CMR) [16, 17], and a high degree of spin polarization [18, 19]. These properties make them especially appealing for nanoscale applications in electron-spin based electronics (spintronics), among others [20, 21]. Regarding the influence of size decrease, it has been shown that thickness reduction down to a few nanometers of coherently strained lanthanum mixed-valence manganite thin films may decrease its Curie temperature [22–24] and suppress its characteristic metal-insulator transition [24–26]. The same compound was shown to change its easy magnetization axis, from in-plane to out-of-plane, in nanometer thick films subject to compressive strain, reflecting the competing shape and magnetoelastic anisotropy contributions in nanometric epitaxial systems [27–30].

In the present thesis we undertake the challenge of realizing and exploring different oxide heteroepitaxial systems with nanoscale $La_{0.7}Sr_{0.3}MnO_3$ (LSMO) mixed-valence manganite as the common ingredient, either in ultra-thin film or in 3D nanoisland configuration. We have optimized a solution-derived bottom-up approach, scalable and cost-effective, which will be demonstrated to yield room temperature ferromagnetic nanostructures. In particular, the election of the single crystal substrate onto which the LSMO is grown will determine whether the LSMO arranges into atomically flat films with thickness below $\sim$10 nm ($SrTiO_3$ (STO) and $LaAlO_3$ (LAO) substrates) or 3D self-assembled nanostructures with lateral sizes below the 200 nm (YSZ and MgO substrates). In addition to the effort done in controlling the growth of these ferromagnetic nanoscale systems, we have also explored them in depth, performing a comprehensive characterization of their morphology, crystallography, microstructure, and magnetic properties. In the specific case of self-assembled LSMO nanoislands we present a detailed investigation of their local magnetic and electrostatic properties by using advanced characterization tools. These techniques include Magnetic Force Microscopy, Photoemission electron microscopy, and Kelvin Probe Force Microscopy, all of them applied for the first time in nanometer-size LSMO features with the characteristics of the nanoislands shown in this work.

Chapter 1

Introduction

This brief introduction is intended to give a very general perspective on the applications, recent trends, and properties of nanoscale ferromagnetic systems, with emphasis in the components that, from an energetic point of view, will rule the magnetic domain structure at the nanoscale. We also shortly describe the general properties of mixed-valence lanthanum manganites, in particular $La_{1-x}Sr_xMnO_3$, in order to provide the reader with the general view of the physical phenomena that have made manganites one of the condensed matter physics hot topics of the last few decades. The chapters following this Introduction deal with largely different topics and techniques which will be there conveniently introduced. Because of the diversity of topics treated, an effort has been made to make each chapter self-consistent, although the report in the actual form follows a logical thread. A guide through the contents of the thesis is given at the end of this Introduction.

1.1 General trends in ferromagnetic nanostructures

The vast range of **applications** of nanoscale magnets covers disciplines as diverse as biomedicine, energy conservation, or the broad field of information technology and communications. In the diagnosis of diseases (e.g. magnetic biosensors), in therapeutic applications (nanomagnets for drug delivery), or in the quest for ultra-strong permanent magnets, the common ingredient appears in the form of nanometer size magnetic nanoparticles and nanoparticle ensembles [1, 31]. In the context of communication technologies, magnetic nanoscale materials offer a great potential for non-volatile magnetic random access memories (MRAMs), the building blocks of instant boot-up computers. MRAMs are based on magnetic tunnel junctions of magnetoresistive materials integrated in silicon-based microelectronics, and, contrary to charge-based RAMs, they maintain the stored information after the power is switched off [32]. Our information-based society also requires enhanced data storage capabilities. Going beyond the recently reached $1Tb/in^2$ density has prompted the size reduction and the nanometer resolution positioning of the magnetic bits. Magnetic storage devices are commonly based on *longitudinal recording systems*, where the bits consist of a number of in-plane magnetized grains ($\sim$10 nm diameter) within a Co-alloy granular medium such as CoCrPtB [33, 34]. However, the reduction of the nanoparticle size finds its limit the moment thermal fluctuations spontaneously reverse the grain magnetization (i.e. when $k_BT \gtrsim KV$), where k_B is the Boltzmann constant, T is the temperature,

K is the anisotropy constant, and V is the particle volume. At this so-called 'superparamagnetic limit', therefore, the stored information is thermally unstable and the device no longer fulfills its function [35]. *Perpendicular recording* is one of the current strategies for increasing the storage capacity while avoiding the superparamagnetic limit: the recording medium now exhibits out-of-plane anisotropy and the bits are stored perpendicular to the film surface. This configuration allows for thicker bits more closely packed to each other [33, 34]. Beyond these two approaches, recent advances head towards magnetic recording based on *lithographically patterned* or *self-organized individual magnetic nanoparticles*, where each nano-object equals one bit of information. Effective nanofabrication approaches are thus crucial for the control of nanomagnet size, shape, and positioning [33, 34].

The technological impact of size miniaturization in magnetic materials is intimately related to the **new and interesting phenomena** that arise when the size of magnetic materials approaches that of characteristic magnetic lengths (e.g. the ferromagnetic (FM) exchange length or the domain wall width of materials, both in the nanometer range). The magnetic configuration of nanosize objects greatly depends on their geometric restrictions, i.e. on their shape (including geometry and aspect-ratio) and size. In isotropic FM systems subject to no strain fields, the general picture is that of competing exchange energy and magnetostatic energy terms, which attempt to reach their corresponding minima in opposite ways: the minimum exchange energy is attained by parallel aligned spins, in a single domain or giant spin configuration. Meanwhile, the magnetostatic term seeks to minimize the magnetic energy within the free space surrounding the object, causing the single domain to divide into multiple domains [36]. The distance where the atomic exchange interactions prevail over the magnetostatic fields is given by the exchange length $l_{ex} = \sqrt{\frac{A}{\mu_0 M_S^2}}$, with A the exchange stiffness constant of the material, M_S its saturation magnetization value, and μ_0 the vacuum permeability. For iron and cobalt, for instance, l_{ex} takes the values l_{ex}(Fe)=1.5 nm and l_{ex}(Co)=2 nm, respectively. On the other hand, the existence of a domain wall within the nanomagnet depends on both the energy required to form such wall, as calculated from the global energy balance, and on the domain wall thickness δ. The former gives a minimum size at which the presence of the domain wall is favorable, known as the *critical single domain radius*, R_{SD}, while the latter reflects the competition between the exchange energy (favoring wide walls) and the anisotropy energy (favoring narrow walls), i.e. $\delta \propto \sqrt{\frac{A}{K}}$, with K the anisotropy constant of the material. Interestingly, while the R_{SD} for a spherical Fe single crystal is R_{SD}=6 nm, the domain wall thickness is close to an order of magnitude higher, δ=40 nm. From here it follows that Fe spherical particles below 40 nm won't exhibit multidomain structure, despite being well above the R_{SD} value. However, this fact does not imply the nano-object to exhibit a uniform magnetization. Indeed, in between the tendency of small objects to exhibit single domain configuration and of larger particles to split into domains, there may exist, for nanostructures of particular geometries and aspect-ratios, an intermediate ground state known as the vortex state [37–39]. The vortex configuration appears when the reduction of the size below the submicron range forces complex multidomain structures into a magnetic flux closure state, rather than into a uniform magnetization state.

Recent **advances in characterization techniques** have greatly improved our understanding of nanoscale magnetic structures. In addition to 'averaging' macroscopic techniques like superconducting quantum interference device (SQUID), ferromagnetic resonance (FMR), or magneto-optical Kerr effect (MOKE), local techniques with sub-micron resolution are essential in order to gain insight into the physical phenomena taking place

within the nanostructures. The progress in Scanning Probe Microscopies such as Magnetic Force and Spin-polarized scanning tunneling microscopies (MFM and SP-STM) [40–42], as well as the enhanced spatial resolutions of synchrotron radiation sources making use of X-ray magnetic circular dichroism (XMCD) have allowed, among other achievements, the observation of the magnetic vortex core [10, 43], and have made its internal structure accessible [44–46]. The magnetic vortex configuration displays a continuous variation of the magnetization direction in the plane of the dot (which reduces the magnetostatic energy) and an out-of-plane perpendicular magnetization in the core [38, 47]. In fact, the vortex core has become an appealing memory unit candidate for data storage [48, 49]. Also, recently, various types of emerging devices such as microwave oscillators [50, 51] and amplifiers [52, 53] based on the properties of magnetic vortices were proposed.

The vast majority of the work done up to date in the context of ferromagnetic nanosize objects, however, has focused on nanostructures of simple ferromagnetic metals. Both experimental and theoretical investigations have thus aimed at understanding the behavior of nanomagnets made out of iron, permalloy ($Fe_{20}Ni_{80}$), cobalt, nickel, or their alloys, and, most commonly, in polycrystalline form. In their review of 2003, Martín and co-workers gather substantial bibliography on the fabrication and properties of magnetic metal nanostructures based on the above soft ferromagnets [54]. Nevertheless, the models valid for these materials, based mainly on the above picture of competing exchange and magnetostatic energies, are insufficient for the case of strained materials featuring single crystal or preferential textures, i.e. the case precisely inherent to epitaxially grown materials. This new context requires taking into account the magnetoelastic and magnetocrystalline anisotropy terms, with the corresponding added complexity.

Certainly, magnetoelastic and magnetocrystalline anisotropies, together with the exchange and magnetostatic contributions mentioned before, also decide on the magnetization processes of bulk materials. The fundamental difference is that, within confined geometries, their individual and collective influences are subject to new boundary conditions and, consequently, they give rise to novel effects. One example of the key role of anisotropies in the nanometer length concerns spin-reorientation transitions (SRT) in monolayer-thick Fe and Co films grown on Ag, Cu and Au. Theoretical and experimental studies have shown that a strong perpendicular surface anisotropy pulls the spins of the FM layer out of the film plane, overcoming the large demagnetizing field. The latter, however, pulls the magnetization back in-plane when the film thickness exceeds a certain limit, in the few monolayers range [55–58]. The geometric shape of 3D nanoparticles, whether triangular, square, circular...etc., is also a crucial parameter which gives rise to new anisotropies. For instance, the fact that only ellipsoids have uniform demagnetizing fields results in inhomogeneous magnetizations within nano-objects with sharp edges (like squares, rectangles, triangles...). Such *configurational anisotropy*, as named by Cowburn and co-workers, produces diverse magnetization patterns that slightly deviate from uniform magnetizations [59–61].

Although less studied, the striking properties of complex oxides such as the ferromagnetic mixed-valence lanthanum manganites make them especially appealing in a nanotructured configuration, as they are strong candidates for the aforementioned technological applications in magnetic sensors, data storage, and spin-based devices. In the next section we will briefly review the main properties of the strontium-doped lanthanum manganites. The multicomponent character of these oxides, in addition to the high sensitivity of their properties to the precise stoichiometry (chemical doping, oxygen content), make them of-

ten challenging to process from a materials point of view, especially in the sub-micrometer length. The last decades' advances in the field of heteroepitaxial growth permits nowadays optimal control of stoichiometries and crystalline quality of oxide thin films. A considerable amount of work thus exists concerning colossal magneto-resistive manganite thin-films [22, 25, 29, 62–65]. We will have the opportunity to go through some of this work when discussing the ultra-thin manganite films in Chapter 3. Conversely, the studies devoted to nanoislands and nanowires are much more scarce [66, 67], if not practically non-existent, as it is the case of the bottom-up fabrication approach followed in this thesis. As most transition metal oxides, these materials are notably harder than the classic metal ferromagnets and they are also chemically stable, which makes them especially challenging to process by wet and dry etching procedures [68, 69].

1.2 Main properties of mixed-valence manganites

Mixed-valence manganese oxides with a perovskite structure, which we shall in the following simply call *manganites*, are given by the general formula $A_{1-x}B_xMnO_3$; here A is a trivalent rare earth cation (La, Nd, Pr...) or bismuth, and B is a divalent alkaline earth cation (Ca, Sr, Ba...) or Pb. Manganites belong to the family of strongly correlated materials, in which diverse and complex phenomena arise from the subtle balance of many competing effects [70]. These competing mechanisms typically concern charge, orbit, spin, and lattice degrees of freedom, which, in turn, are governed by the electron-electron and electron-lattice interactions taking place in these compounds.

The field of manganites has been one of the most active within condensed-matter physics in the last few decades, and therefore the amount of literature concerning their growth, properties, and fundamental physics is vast. Here we attempt to give a very brief and general overview of the fundamental properties of manganites, with particular emphasis in the strontium-doped lanthanum manganite $La_{1-x}Sr_xMnO_3$, the relevant compound for this thesis. For a more in-depth treatment the reader is directed to the many excellent reviews that comprehensively cover the state of the art in the field [17, 68, 71–74].

Main features of manganites: colossal magnetoresistance and half metallicity

The striking discovery of a simultaneous ferromagnetic and metallic behavior in the mixed compounds $LaMnO_3$- $BMnO_3$, with B=Ca, Sr and Ba, by Jonker and Van Santen, dates back to 1950 [75]. Such a behavior was soon explained in the context of the Double Exchange Model (DE) by Zener [76], Anderson and Hasegawa [77], and de Gennes [78]. A renewed interest in manganites, however, arose decades later, in the 1990s, with the discovery that the application of a magnetic field induces a large change in the electrical resistance of $La_{0.67}Ca_{0.33}MnO_3$ thin films, in the vicinity of their Curie temperature T_C [79]. Furthermore, this effect is accompanied by an intriguing metal-insulator transition occurring at T_C. Such negative magnetoresistance (MR) (the resistance decreases with the applied field) is three orders of magnitude larger than the Giant magnetoresistance (GMR) characteristic of multilayer and granular metals. For this reason this new effect became known as Colossal magnetoresistance (CMR). The GMR effect is based on the spin-dependent tunneling of electrons from one ferromagnet to another across a thin insulating barrier (e.g. two ferromagnetic grains separated by a grain boundary) [20, 80]. This tunneling can occur at low

fields ($\lesssim$0.1 T) and is largest when the alignment of ferromagnetic (FM) domains is parallel. It also increases with decreasing temperature and particle size [81]. Conversely, the CMR effect occurs in perfect manganite single-crystals, requires rather large fields, and is maximum at T_C, i.e. at the metal-insulator transition. Fig. 1.1 shows the temperature-dependent resistivity of a $La_{1-x}Sr_xMnO_3$ crystal (x=0.175) for different applied fields. The magnitude of the magnetoresistance is given by the expression $\Delta\rho/\rho$=$[\rho(H \neq 0) - \rho(H = 0)]/\rho(H = 0)$ (in %). Open circles in Fig. 1.1 correspond to the negative MR for the case of H=15 T [82]. CMR is a phenomenon intrinsic to manganites, and the physics behind have raised, and still do, many fundamental questions [71]. On the other hand, the exploitation of these large resistance changes opens a wide range of technological opportunities in spin-based electronics.

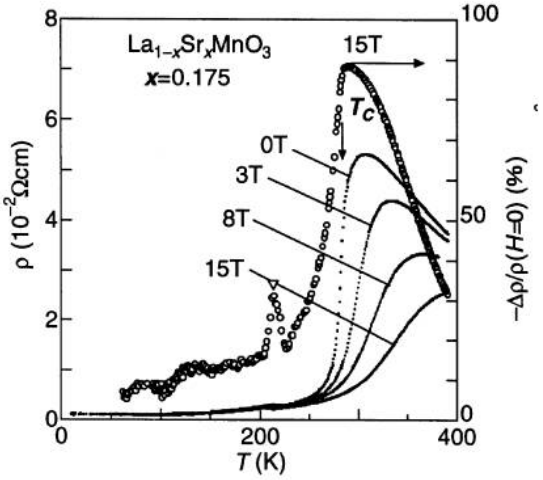

Fig. 1.1: *Temperature dependent resistivity of a $La_{1-x}Sr_xMnO_3$ (x=0.175) crystal for different applied magnetic fields. The curves show a metallic character (dρ/dT>0) below T_C and an insulator (dρ/dT<0) behavior above T_C. The negative magnetoresistance -Δρ/ρ (in %) for a 15 T applied field is given with open circles. Reproduced from [82].*

Another essential characteristic of manganites is their high degree of spin polarization. Together with some exotic compounds like Mn-based Heusler alloys [83] or chromium (IV) oxide [84], manganites are among the few compounds that exhibit half-metallic character, as first demonstrated by Park and co-workers [18]. In particular, while in most ferromagnetic metals (like Fe or Ni) both up and down spin sub-bands are partially occupied, in manganites the Fermi Energy level E_F falls into the gap of one of the sub-bands (see Fig. 1.2). As a consequence, the spin polarization, given by the imbalance of up and down spin-dependent density of states n at the Fermi level, $P = (n^{\uparrow} - n^{\downarrow})/(n^{\uparrow} + n^{\downarrow})$, is in principle equal to one in half metals. Polarization values of ∼30-50% have been measured for Fe, Ni, Co, and their alloys [85], while reaching the ideal value of ∼100% for the case of $La_{0.7}Sr_{0.3}MnO_3$ [18]. This result is directly related to the predominant d-orbital character at the Fermi level characteristic of transition metal oxides, which enhances the on-site exchange interaction. The half metallicity makes manganites especially appealing for spin-based devices like magnetic tunnel juntions [86–88].

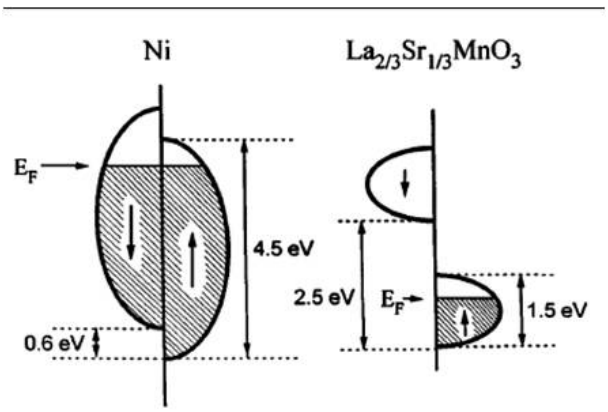

Fig. 1.2: *Sketch comparing the energy bands of a ferromagnetic metal (Ni) and of a fully polarized ferromagnetic half metal ($La_{1-x}Sr_xMnO_3$ with x=1/3). Reproduced from [81].*

Crystal structure of perovskite manganites

Despite exhibiting phenomena such as CMR and half-metallicity, the building blocks of these complex oxides are remarkably simple. Fig. 1.3 illustrates the perovskite unit-cell, ABO_3, where A is the trivalent La ion or the divalent Sr ion, in a ratio determined by the doping x, B is the manganese ion, with average valence $3+x$, and O is the oxygen anion. Manganese ions sit at the centers of oxygen octahedra, in a 6-fold coordination. Although the ideal perovskite holds a $Pm\bar{3}m$ cubic symmetry, many of the compounds with the perovskite-type structure show lower symmetries. This is the case of manganites, which generally adopt either rhombohedral or orthorhombic structures. For $La_{0.7}Sr_{0.3}MnO_3$ it is a common procedure, both in magnetic and structural studies, to describe its rhombohedral $R\bar{3}c$ structure in terms of the pseudo-cubic notation, which greatly simplifies the indexing and treatment of the structure [17, 22, 89, 90]. In such pseudo-cubic notation $La_{0.7}Sr_{0.3}MnO_3$ exhibits a lattice parameter a∼3.873 Å and an angle ∼90.26° [64], which implies a very slight deviation from a perfect cube. We will use this notation throughout the whole report.

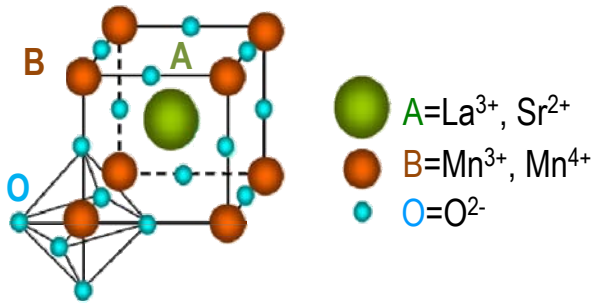

Fig. 1.3: *Unit cell of the LSMO perovskite structure.*

The tendency to distort from the ideal cubic perovskite may be understood via the relationship between the ionic radii of its constituents. According to Goldschmidt [91], we can define the *tolerance factor* f:

$$f = \frac{(R_A + R_O)}{\sqrt{2}(R_B + R_O)} \tag{1.1}$$

where R_A and R_B are the ionic radii of A and B, respectively, and R_O is the ionic radius of oxygen in an idealized model of rigid spheres. For an undistorted cubic perovskite structure, f takes a value close to the unity, whereas materials where f deviates from 1 tend to adopt lower symmetries. In most stable perovskites f ranges from $\sim$0.8 to 1.1. The average cation radius R_A critically influences the tilting and rotations of the oxygen octahedra, with a consequent impact on the Mn-O-Mn bond angle. Such bond angle, in turn, will determine the transport and magnetic properties of the manganite, as we shall mention later.

Electronic structure of manganites

The crystal field due to the octahedral oxygen cage surrounding the Mn ion partially lifts the degeneracy of the $3d$ Mn multiplet, splitting it into a triply-degenerate t_{2g} level and a doubly-degenerate higher energy e_g state. Fig. 1.4 shows the schematic diagram of the energy levels of Mn, and how the electrons fill the levels in Mn^{3+} ($3d^4$ configuration). A spontaneous distortion of the octahedron (elongation or compression along the axial direction), known as the Jahn-Teller (J-T) distortion, further lifts the degeneracy of the t_{2g} and e_g levels in the Mn^{3+} (see Fig. 1.4). This phenomenon, of electronic origin, does not occur in the Mn^{4+}, where the e_g level is empty. The alignment of the electrons is always parallel, following Hund's rules, and gives a total spin state S=2 and S=3/2 for Mn^{3+} and Mn^{4+}, respectively. The lower energy t_{2g} electrons, less hybridized with the oxygen $2p$ orbitals, are localized even in the metallic state of manganites. Conversely, the e_g electrons can be itinerant, and are responsible for electric conduction when there are empty e_g states available in the crystal. Those 'empty states' are achieved by hole-doping the parent compound ($LaMnO_3$, for instance, in the case of $La_{1-x}Sr_xMnO_3$): the substitution of the trivalent La by the divalent alkaline earth produces Mn^{4+} ions with empty e_g states. When there is no such hole-doping, strong correlation effects tend to localize the e_g electrons, which is the reason why $LaMnO_3$ is an insulator.

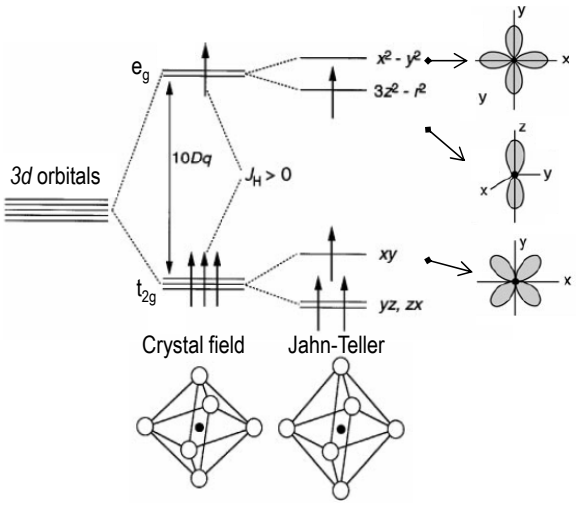

Fig. 1.4: *3d atomic levels of the Mn ion. The octahedral crystal field splits the five-fold 3d degeneracy into a triply-degenerate t_{2g} low energy and a doubly-degenerate e_g high energy level. For the case of Mn^{3+}, the spontaneous distortion of the octahedra (plotted in the form of an axial elongation) further lifts the degeneracy and stabilizes its electronic configuration. Adapted from [17].*

The reason why ferromagnetism and metallic behavior go hand in hand in these compounds is based on the electronic features outlined above, i.e. in the large exchange energy (large J_H∼2-3 eV) [17] or large on-site Hund coupling between the Mn $3d$ electrons. The *Double Exchange* (DE) mechanism consists in the jump of one e_g electron to a neighboring empty e_g state, mediated by the oxygen in between. In particular, the electron leaving Mn^{3+} jumps to the oxygen orbital while the electron in the oxygen with the parallel spin simultaneously jumps to the Mn^{4+} (see Fig. 1.5). In the strong coupling limit (i.e. J_H is much greater than the intersite hopping interaction t_{ij}^0) the effective hopping interaction t_{ij} depends on the relative orientation θ_{ij} of the spins of the neighbor i and j atoms in the following way [77]: $t_{ij} = t_{ij}^0 \cos\theta_{ij}$. Thus, the electron itineracy is largest when spins are

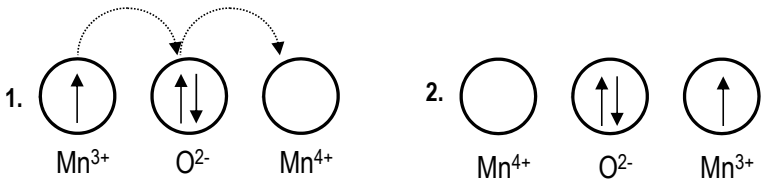

Fig. 1.5: *Double exchange model. Adapted from [71].*

parallel (ferromagnetic configuration), and zero if they are anti-parallel.

Complexity in manganite systems

Although intuitive and useful, the DE model briefly outlined above is insufficient to explain all the phenomena shown by manganites, like, for instance, the particularities of the insulator state above T_C [17]. In general, the more weight the insulating states acquire in the manganite, the greater the limitations of the DE model [71]. Other interactions like the electron-lattice interactions (such as collective Jahn-Teller distortions), charge/orbital ordering, or the antiferromagnetic superexchange, are all crucial for the understanding of the physics of manganites. Indeed, these interactions and their mutual competition are responsible for the rich phase diagrams characteristic of these compounds.

The fundamental parameters that characterize correlated systems like manganites are the electron hopping amplitude t (or one-electron bandwidth w) and the band-filling n (the density of carriers). Both parameters are changed in manganites by acting upon the chemistry of the compound: the change in the average cation radius leads to a change in the Mn-O-Mn bond angle of the perovskite structure (a change in the degree of lattice distortion), which affects the hopping amplitude of the itinerant electrons. On the other hand, by changing the doping x we vary the band filling n ($n = 1 - x$). Therefore, the greater the divalent ion doping, the more holes we are injecting into the structure. Fig. 1.6 shows the phase diagram of $La_{1-x}Sr_xMnO_3$, the prototypical large bandwidth manganite, where the DE model works best. It shows a stable ferromagnetic-metallic state, ranging from Sr dopings between x∼0.2 to x∼0.45, with a high T_C, maximum (∼360 K) for x=0.3. Decreasing the cation radius, by, for instance, doping the $LaMnO_3$ parent compound with Ca instead of with Sr, the Mn-O-Mn bond angle changes in a way that reduces the hopping amplitude. Upon bandwidth reduction, charge and orbital-ordered insulating phases become more dominant. Indeed, for further smaller cationic radius as in $Pr_{1-x}Ca_xMnO_3$, represen-

tative of 'small' bandwidth manganite*, there exists no stable ferromagnetic-metallic state at zero applied field [see Fig. 1.6 (b)].

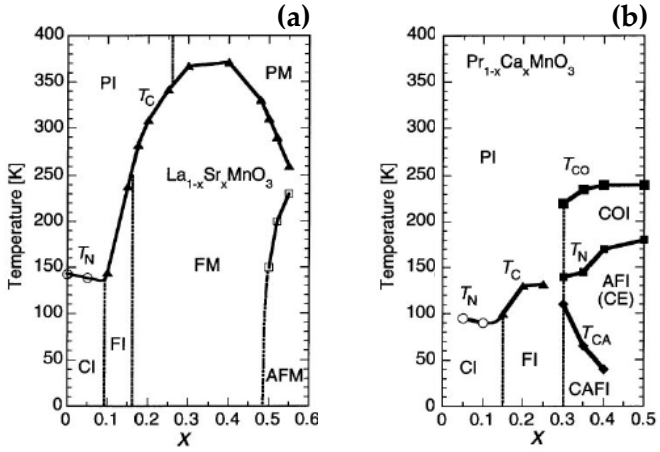

Fig. 1.6: *Magnetic and electronic phase diagrams for (a) $La_{1-x}Sr_xMnO_3$ and (b) $Pr_{1-x}Ca_xMnO_3$. FM, PM, PI, FI, CI, and AFM stand for ferromagnetic metallic, paramagnetic metallic, paramagnetic insulating, ferromagnetic insulating, spin-canted insulating and antiferromagnetic (A-type) metallic, respectively. In the $Pr_{1-x}Ca_xMnO_3$ phase diagram, COI denotes charge-ordered insulating state, and AFI (CE) and CAFI are an antiferromagnetic and canted antiferromagnetic insulating states, respectively, within the more general COI charge-ordered state. T_C and T_N are the Curie and Néel temperatures, respectively. Reproduced from [17].*

1.3 Outline of the thesis

Manganites exhibit a large number of interesting physical phenomena due to their interrelated structural, electronic, and magnetic properties. A flavor of this complexity was given in the above brief overview. The present thesis deals with the synthesis and characterization of chemically-derived nanoscale $La_{0.7}Sr_{0.3}MnO_3$ (LSMO) systems grown onto different single crystal substrates. The understanding of how the physics of correlated electron systems works in such nanoscale heteroepitaxys is thus beyond the scope of the present thesis, and, hence, left for future studies. We here set the basis for the fabrication of ultrathin films and 3D self-assembled nanoislands of ferromagnetic LSMO, using a scalable and versatile bottom-up approach, and provide a comprehensive characterization of the synthesized systems by means of both macroscopic and nanoscale experimental techniques. The manuscript is organized as follows:

Chapter 2 presents the experimental procedure followed to grow the nanoscale LSMO heteroepitaxys object of this work. We give an overview of the different oxide substrate materials we have used, and we discuss the effect of heat treatments on the surface conditioning of these substrates. The necessary steps for the growth of nanoscale LSMO onto such substrates, by means of the chemical solution deposition method (CSD), are also described.

*Note that the average cation radii are <r>$_{(La,Sr)}$~1.4 Å and <r>$_{(Pr,Ca)}$~1.32 Å for $La_{1-x}Sr_xMnO_3$ and $Pr_{1-x}Ca_xMnO_3$, respectively [71].

The results of applying the procedure previously explained in Chapter 2 are extensively analyzed in *Chapter 3*. We show how the same methodology gives two distinct system configurations depending on the substrate underneath: ultra-thin LSMO films, below 10 nm thick, grow on top of perovskite-type $SrTiO_3$ and $LaAlO_3$ substrates, and are discussed in Part I. In contrast, LSMO arranges into a homogeneous dispersion of self-assembled LSMO nanoislands when grown onto fluorite-type and rocksalt-type structures, as shown in Part II. For each case we have accomplished the study of the system morphology, its crystal orientation and epitaxy, its microstructure, and the macroscopic magnetic and transport properties. Our results highlight the capability of this solution approach to generate epitaxial ultra-thin films and sub-200 nm lateral size nanostructures with Curie temperatures around $\sim$350 K.

Given the interest of nanoscale 3D structures, highlighted in this Introduction, and considering the scarce studies regarding 3D manganite nanostructures, we have devoted *Chapter 4* and *Chapter 5* to the local analysis of self-assembled ferromagnetic LSMO nanoislands grown on fluorite-type insulating substrates.

Chapter 4 describes the magnetic force microscopy (MFM) investigation of the aforementioned system. We first discuss the experimental concerns linked to measuring fairly small (sub-200 nm wide) LSMO nanoislands, and we describe the optimization of the magnetic signal by choosing the adequate magnetic tip. Subsequently, we focus on the study of the variety of magnetic structures displayed by nanoislands, among which we identify the geometric parameters that promote the vortex state in these LSMO nanostructures. The effect on the magnetic nanoislands of an external in-plane magnetic field is also discussed.

Two advanced characterization techniques, novel in their application to a system of these characteristics, are used in *Chapter 5* to further investigate the local properties of the LSMO nanoislands. The first part of the chapter concerns a local chemical and magnetic study of the nanoislands using photoemission electron microscopy (PEEM) at synchtrotron facilities. We discuss the crucial role of the metal capping of the insulating substrates and explain the results that give simultaneous access to the nanoisland surface and bulk chemistry. We also describe the results and limitations of the X-ray magnetic circular dichroism experiments on our system of self-assembled LSMO nanoislands. The second part changes the topic to the electrostatic properties of the LSMO nanoislands, addressed by means of Kelvin Probe Force microscopy (KPFM). Here again, the insulating character of the substrate adds complexity to the experiment as well as to the interpretation of the results. We demonstrate that KPFM is sensitive to a change in contrast between different LSMO crystallographic planes. We argue that this contrast variation is directly related to a difference in the work function between those planes.

The main conclusions of the work are collected in the *General Conclusions*. An appendix at the end of the manuscript gathers the main specifications on the techniques used to characterize the samples. MFM, PEEM, and KPFM are not included there, since they are introduced in the corresponding chapters.

Chapter 2

Experimental procedure

This chapter describes the substrate materials and the methodology followed to generate the $La_{0.7}Sr_{0.3}MnO_3$ (LSMO) heteroepitaxial systems that are the object of this thesis. Far from being passive components that only provide mechanical support, oxide substrates play a key role in heteroepitaxial growth, especially at the nanoscale, where interfacial effects are important. We will first review their main crystallographic properties and then describe the protocols that we followed to treat their surfaces. The growth of nanostructured manganite oxides through the chemical solution deposition (CSD) route will be described afterwards. We will briefly present the growth procedure, postponing the detailed analysis and discussion of the results to Chapter 3.

2.1 Single crystal oxide substrates

Single crystal oxide substrates are one of the two ingredients that constitute the heteroepitaxial systems described in this thesis. Nucleation and growth of the oxide nanostructures is determined by the presence of the solid oxide substrate underneath and hence, its crystal structure and surface properties are crucially important. Oxide substrates are widely used for the heteroepitaxial growth of high temperature cuprate superconductors, multiferroic and magnetoresistive thin films (for a review on these topics see [92, 93] and references therein). The relevance of the substrates in relation with the grown species, is, in fact, one of the main points of this thesis as it will become evident throughout the manuscript. We have used four different oxide substrates, perovskite-type $LaAlO_3$ (LAO) and $SrTiO_3$ (STO), rock-salt structure MgO, and the fluorite-type yttria-stabilized zirconia (Y_2O_3:ZrO_2). This section is intended to give a general overview on such materials.

2.1.1 Perovskite-type substrates: $SrTiO_3$ and $LaAlO_3$

The perovskite structure was already introduced in the previous chapter, as it constitutes the building blocks of the manganites described in there. However, this structure is far from restricted to complex manganese oxides. Many inorganic crystalline solids adopt the ABX_3 perovskite structure, with two inequivalent A and B metal cations and X an anion that bonds to both. In particular, oxide perovskites, with ABO_3 general formula, in addition

to colossal magnetoresistance, can also exhibit superconductivity [94] and ferroelectricity [95]. In the ideal cubic perovskite, the larger A cation has 12-fold coordination to oxygen, while the smaller B cation sits at the centers of the octahedra formed by oxygens, in a 6-fold coordination (see Fig. 2.1). The structure may be also visualized as an alternate sequence of A-O and B-O_2 planes [Fig. 2.1(c)], stacked along each of its three orthogonal axes. The crystallographic parameters of the cubic ideal perovskite are written in Tab. 2.1. As we mentioned in Chapter 1, many of the compounds with the perovskite-type structure do not adopt cubic symmetry at room temperature. Instead, they commonly suffer cation displacements and tilting of the oxygen octahedra that give rise to lower symmetry structures such as tetragonal (e.g. $BaTiO_3$[96]), orthorrombic (e.g. the original Perovskite mineral $CaTiO_3$[97]) or rhombohedral (e.g. $LaAlO_3$[98]). The degree of deviation from the ideal cubic perovskite is quantified by the tolerance factor, the unity being the value of the undistorted cubic perovskite structure such as $SrTiO_3$ (STO). The value for $LaAlO_3$ (LAO) is $\sim$1.02.

Space Group	Atom	Wyckoff Pos.	(x y z) coordinates
$Pm\bar{3}m$	A cation	1b	$(\frac{1}{2} \quad \frac{1}{2} \quad \frac{1}{2})$
	B cation	1a	$(0 \quad 0 \quad 0)$
	O anion	3d	$(\frac{1}{2} \quad 0 \quad 0)$

Tab. 2.1: *Crystallographic parameters of the ideal cubic perovskite structure.*

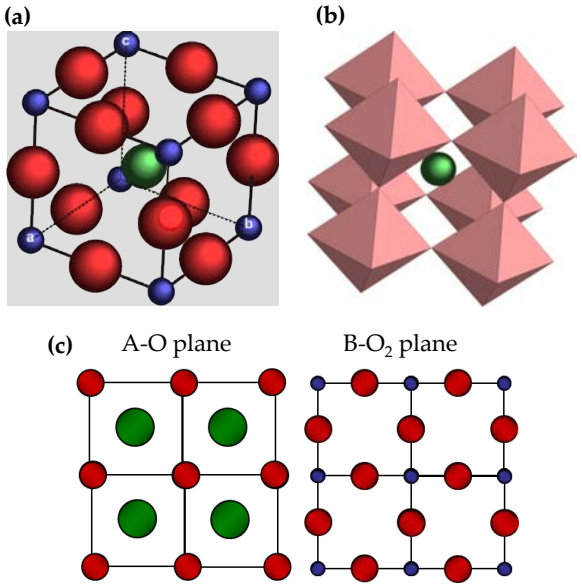

Fig. 2.1: *(a) 3D view of the ideal cubic perovskite unit cell with the A cation (green) at the center, B (blue) at the corners, and the oxygens (red) at half the edge length. (b) View of the perovskite illustrating the oxygen octahedra. In the idealized structure they remain untilted. (c) Top-view of the A-O and B-O_2 planes.*

$SrTiO_3$

The ideal cubic perovskite structure (space group $Pm\bar{3}m$) is the one adopted by $SrTiO_3$ (STO) (read *strontium titanate*) at room temperature. At around 110 K, however, it undergoes an antiferrodistortive phase transition to a tetragonal phase (space group $I4/mcm$) [99, 100], which is caused by the antiphase tilting of the oxygen octahedra. STO is widely used as substrate for the epitaxial growth of high T_c superconducting layers and other functional perovskite oxides like the magnetoresistive manganite. This is mainly due to the low lattice mismatch between STO and these isostructural materials.

The STO substrates used in this work are 5 mm x 5 mm x 0.5 mm single crystals commercially available from Crystec. They are one side polished, have a nominal (001) orientation, and a lattice parameter $a_{STO} = 3.905$ Å given by the supplier. We measured the out-of-plane lattice parameter by X-Ray diffraction θ-2θ scans (see Appendix A), which gave $a_{STO} = 3.90(7)$ Å, in good agreement with the value of the supplier and also with reported values in the literature [101].

$LaAlO_3$

Lanthanum aluminate, $LaAlO_3$ (LAO), displays a cubic ideal perovskite structure at high temperatures, but undergoes a well established second order phase transition to the rhombohedral $R\bar{3}c$ structure close to 800 K, with parameters $a = b = c = 5.3547(3)$ Å and $\alpha = \beta = \gamma = 60.113(4)^\circ$ [98, 102–104]. More conveniently, this rhombohedral distorsion is described in terms of the pseudocubic cell with $a_{LAO} = 3.79$ Å and $\alpha = 90.096^\circ$ [104]. As in most phase transitions to lower symmetry structures, the cubic to rhombohedral transition is accompanied by twin plane formation, which relieves the strain caused by the lattice distorsion. {110} and {100} twin planes have been both reported, although the latter is more frequently observed [105, 106]. Such twin domains can be seen with optical microscopy and scanning probe techniques [Fig. 2.2 (a) and (b)]; sometimes even with the naked eye. A thorough description of twinning in LAO is given in the work by Bueble and co-workers [104]: a surface cooled through its transition temperature T_C (∼800 K) down to room temperature, exhibits a *sawtooth* morphology, characteristic of the presence of such twin domains and caused by the relaxation of the macroscopic stress. Afterwards, this crystal is cut and polished into a flat surface. Under a subsequent annealing at $T>T_C$ the structure reorganizes and the footprints of the twinning emerge. When cooled down again at $T<T_C$, the phase transition triggers a new twinning so that the final surface topography is an superposition of footprints of previous domains and actual domains [Fig. 2.2 (c)].

The LAO substrates used in the present work are 5 mm x 5 mm x 0.5 mm single crystals commercially available from Crystec. They are one side polished, have a nominal (001) orientation and a given lattice parameter $a_{LAO} = 3.821$ Å. Literature values are closer to $a_{LAO} = 3.789$ Å [102, 104], in agreement with our X-Ray Diffraction measurements ($a_{LAO} = 3.79(2)$ Å).

2.1.2 Rocksalt-type substrates: MgO

Oxides with rocksalt structure (also called NaCl-type structure) are among the most widely studied oxides. They are simple insulators that can be described in terms of mixed ionocovalent bonds, as opposed to complex oxides with strongly correlated electrons. *Mag-*

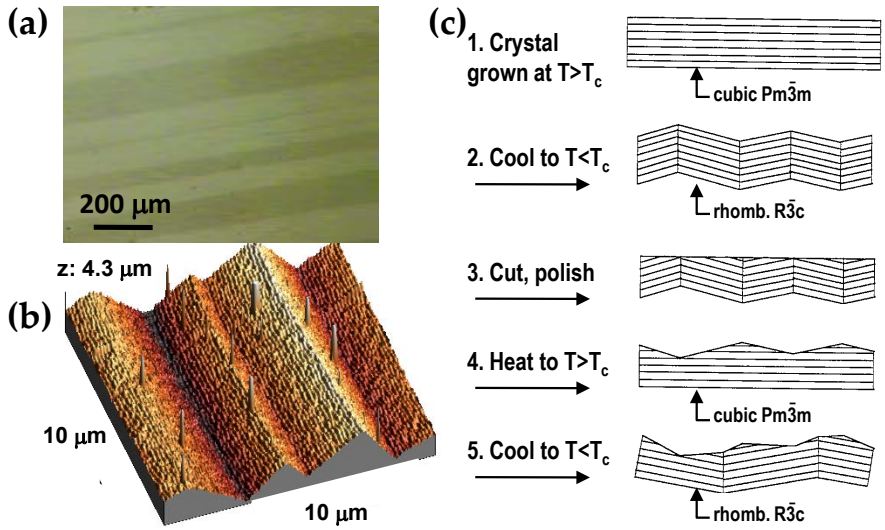

Fig. 2.2: *(a) Optical micrograph of a LAO substrate showing distinct contrast due to twin domains. (b) Atomic force microscopy 3D image of the characteristic sawtooth surface corrugation caused by twinning. (c) Schematic illustration of the process leading to overlaid twin domain 'footprints' and actual twin domains caused by consecutive cooling and annealing. Adapted from [104].*

nesium Oxide (MgO) is the paradigmatic example of this materials class and there are extensive literature studies concerning its structural and electronic properties from diverse theoretical perspectives [107–109]. MgO is used as support for metal catalysts [110] and also as substrate for high T_C superconductor films where its low dielectric constant makes it suitable for high-frequency applications [111, 112].

Rocksalt structure may be described as two interpenetrated facecentered-cubic (FCC) lattices of opposite charge. It contains one formula unit per primitive cell and belongs to the $Fm\bar{3}m$ spatial group. Fig. 2.3 below shows the atom coordinates that build up the MgO conventional unit cell, illustrated in the right panel.

Space Group	Atom	Wyckoff Pos.	(x y z)
$Fm\bar{3}m$	Mg cations	4a	(000)
	O anions	4b	$(\frac{1}{2}\frac{1}{2}\frac{1}{2})$

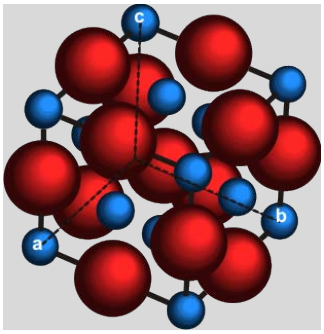

Fig. 2.3: *MgO crystal structure and its cubic unit cell displayed on the right. Blue spheres represent Mg cations and red spheres represent the oxygens.*

The MgO substrates used in thist work are 5 mm x 5 mm x 0.5 mm single crystals commercially available from Crystec. They are one side polished, have a nominal (001) orientation and a given lattice parameter $a_{MgO} = 4.21$ Å in agreement with literature [113]

and with our X-Ray Diffraction results ($a_{MgO} = 4.21(4)$ Å).

2.1.3 Fluorite-type substrates: Y_2O_3:ZrO_2 (YSZ)

Pure Zirconia, ZrO_2, displays a monoclinic structure at ambient conditions (room temperature and atmospheric pressure) and only reaches the cubic phase at very high temperatures (∼2650 K), after going through an intermediate temperature transition to tetragonal symmetry [114]. However, the doping of zirconia with a considerable amount of yttria (between 8-40 mol % Y_2O_3) stabilizes the cubic fluorite structure, space group $Fm\bar{3}m$, at ambient conditions [115]. In addition to an increased resistivity against thermal stresses, such a doping introduces oxygen vacancies that make *yttria-stabilized zirconia* (YSZ) a remarkable ionic conductor, very commonly used as electrolyte in Solid Oxide Fuel Cells (SOFC) [116]. Fig. 2.4 displays the crystal structure parameters and the illustration of the conventional unit cell.

Space Group	Atom	Wyckoff Pos.	(x y z)
$Fm\bar{3}m$	Zr cations	4a	(000) Occ.0.81
	Y cations	4a	(000) Occ.0.19
	O anions	8c	$(\frac{1}{4}\frac{1}{4}\frac{1}{4})$

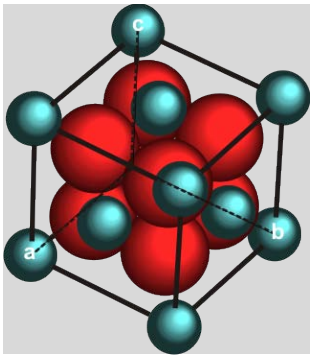

Fig. 2.4: *Crystallographic parameters of the YSZ structure (left panel) and the illustration of the unit cell containing 4 cations (blue) and 8 oxygens (red). The occupancy (Occ.) of the cations corresponds to an Y_2O_3 doping of 9.5 mol %.*

The YSZ substrates used in the present work are 5 mm x 5 mm x 0.5 mm one side polished single crystals from Crystec. The data sheet available from the provider sets the Y_2O_3 doping at 9.5 mol %, which means we have the cubic compound $Y_{0.19}Zr_{0.81}O_{1.9}$. They give a lattice parameter of 5.12 Å. However, from literature, a larger lattice parameter would be expected for such doping concentrations: values from $a_{YSZ} = 5.13$ Å to $a_{YSZ} = 5.14728$ Å are reported for 9.4 mol % [117] and 10 mol % [118], respectively. Indeed, our X-Ray Diffraction measurements for the 9.5 mol % doping gave a value $a_{YSZ} = 5.14(7)$ Å, which is in reasonable agreement with the literature values.

2.2 Substrate surface conditioning

The surface of the substrate, in contact with the phase grown on top, is decisive in heteroepitaxial growth. A clean surface free of contaminants, with roughness in the atomic scale and high crystallinity is required. A single-terminated surface in complex oxides such as perovskites is often also desirable, as in the case of superlattices, where an atomic-scale control of the alternating planes is necessary for tailoring their physical properties [11, 119].

There are extensive works on thermal and chemical treatments of substrates for the generation of surfaces with the above characteristics. We will review a few here, focusing on their application to our own substrates. These methodologies improve along with the advances in the techniques that enable substrate surface characterization: scanning probe microscopies, surface-sensitive spectroscopies, and surface diffraction techniques are among those used to characterize the structure and chemistry of surfaces. It is also worth noting the large amount of theoretical studies of oxide substrate surfaces. These works discuss the surface atomic and electronic structure and can predict energetically favored terminations and facets, among other characteristics. A substantial amount of experimental and theoretical studies are reviewed in the 1996 book by Noguera [120]. The number of works in the field has, from then on, remarkably increased.

Single crystals are cut through rational crystallographic planes such as (001), (011), and (111) for the cubic case. However, an unavoidable misorientation in the cutting process results in the well-known step-terrace morphology, where atoms reorganize into the nominal low-energy surface planes (Fig. 2.5). Specific thermal and chemical treatments provide atomic diffusion towards a well defined terrace-step structure and also trigger the desorption of contaminant adatoms. After such treatments, surfaces exhibit atomically flat terraces and steps that are integer or half-integer multiples of the crystal unit cell height a [i.e. na or $(n+\frac{1}{2})a$]. The smaller the miscut, the wider the terrace will be, as it follows from Eq. 2.1, where λ is the width of the terrace. In most as-received substrates both na and $(n+\frac{1}{2})a$ types of steps are typically present, which, for perovskites, implies that both A-O and B-O_2 terminations coexist.

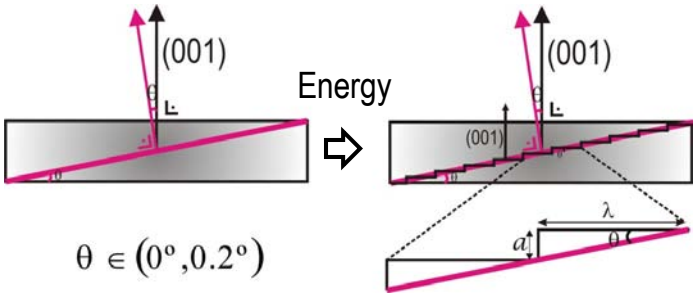

Fig. 2.5: *The real cut and polished surface differs typically in θ ∼0-0.2° from the rational crystallographic (001) plane. Under the effect of heat, surface atoms are able to diffuse to form (001) oriented terraces.*

$$\tan\theta = \frac{a}{\lambda} \tag{2.1}$$

2.2.1 (001)-oriented $SrTiO_3$ and $LaAlO_3$ surfaces

In the case of the widely studied STO surface, Kawasaki and co-workers were the first to develop a method, based on variable pH acid solutions, that attacks the most basic Sr-O termination and yields a single Ti-O_2 terminated surface [121]. Koster and colleagues proposed a similar method, although less dependent on the pH of the etching solution [122]. Here, the Sr-O termination reacts with CO_2 and water to give $SrCO_3$ and $Sr(OH)_2$, respectively. The latter hydroxide dissolves in acid solutions and leaves the more stable Ti-O_2 termination. These works have boosted many efforts in the development of procedures

to achieve the ultimate control of the surface structure and chemistry. Recent advances in this context include the nanopatterning of STO substrates with a controlled coexistence of the two terminations, achieved using simple high temperature annealing [123].

Fig. 2.6 shows two Atomic Force Microscopy (AFM) images of (001)-oriented as-received STO and LAO substrates after cleaning with acetone and methanol in an ultrasonic bath to eliminate non-polar and polar impurities, respectively. The terraces due to the miscut angle θ are observable, but they are not well defined. To improve the quality and achieve well defined step-terraces, after the cleaning, the substrates are put in a covered alumina crucible. This is then placed in a quartz tube that goes inside a high-temperature tubular furnace. Substrates are annealed at 900°C for 5 h under flowing oxygen (0.5 $l \cdot$ min^{-1}, regulated with a mass-flow controller). Heating and cooling rates are 15°C $\cdot$ min^{-1} and 10°C $\cdot$ min^{-1}, respectively. Such process is reported in the literature to generate atomically flat terraces with a majority of Sr-O termination [124]. We will hereafter refer to it as *standard treatment*.

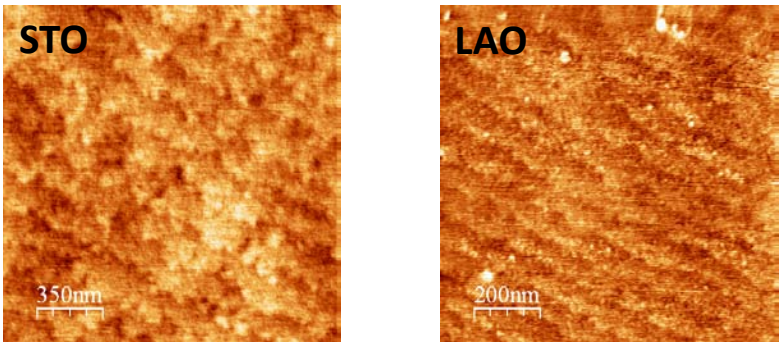

Fig. 2.6: *AFM topography images of as-received (001)-STO and (001)-LAO surfaces. The measurements were done after cleaning the impurities with acetone and methanol in an ultrasonic bath. The scale in* ***z*** *is 1.5 nm (STO) and 2.5 nm (LAO).*

The result of the described annealing process is shown in Fig. 2.7, which displays 1 µm $\times$ 1 µm AFM images of three different STO substrates, identically treated. In every case the presence of terraces is clearer than in the as-received substrates. However, the morphologies show an increasing step-edge roughness with increasing terrace width. These terraces appear very poorly defined in the $\lambda\sim$500 nm-wide case. Note also the presence of holes on the terraces. This is an evidence that atomic diffusion on the wide terraces was not enough to fully reconstruct them. In other words, for substrates with smaller miscut more energy is required to obtain smooth and well defined morphologies (higher temperature or longer annealing times). Nevertheless, even for the highest quality terrace structures, step heights of na and $(n + \frac{1}{2})a$ were identified, indicative of coexisting Sr-O and Ti-O_2 terminations.

In order to obtain single Ti-O_2-terminated substrates, we chemically attacked the surface, following the procedure described by Koster et al. [122]: substrates were first ultrasonically cleaned in a Milli-Q purified water bath for 3 min, and then attacked with a buffer ammonium fluoride-hydrofluoric acid mixture solution for 30 s ($NH_4 \cdot HF$, pH 6.5, Sigma Aldrich). The acid was rinsed with more Milli-Q water and the substrate was finally put in the furnace and heat-treated at 900°C for 5 h. As we said above, such acid attacks the $Sr(OH)_2$ formed at the Sr-O termination in contact with water, leaving the more stable

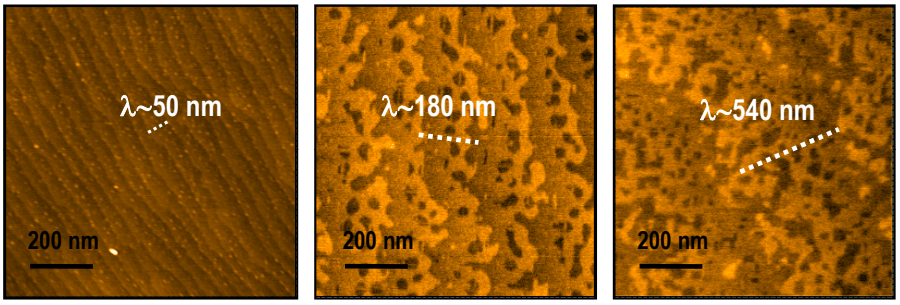

Fig. 2.7: *$1\mu m \times 1\mu m$ AFM topography images of three different STO substrates after the same thermal treatment. The scale in* **z** *is ∼2 nm.*

Ti-O_2 termination intact. The latter will be reconstructed into smooth terraces during the annealing. The comparison between a simply annealed and an etched and annealed STO surface is illustrated in Fig. 2.8.

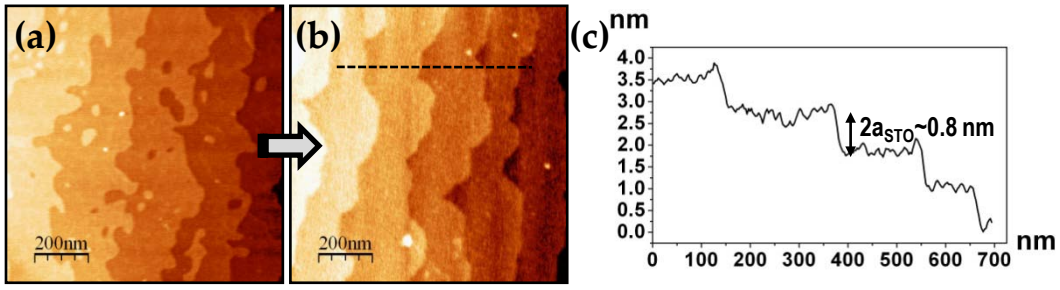

Fig. 2.8: *$1\mu m \times 1\mu m$ AFM topography images of the same STO substrate after the annealing process (a) and after the surface etching and final annealing (b). Note how the holes disappear and the edges straighten. (c) The line profile on the right shows the step height for the edged substrate is twice the STO lattice constant. The scale in* **z** *is ∼4 nm in the two AFM figures.*

Although this method seemed to be most effective to obtain smooth and single-terminated STO surfaces, it proved occasionally to be too aggressive for our STO crystals: Fig. 2.9 shows a wider (4.7 µm $\times$ 4.7 µm) AFM image displaying very smooth terraces accompanied by a high density of etch pits. Such pits are holes of significant width (∼200 nm) and depth (∼4-20 nm). Representative length scales may be observed in the profile corresponding to the dashed line on the image. In some cases, the sum of many of them results in holes of large size, which propagate along the crystallographic [100] and [010] directions. Such features were reported in reference [122] to occur for more acidic etching solutions (pH 4.5) but not for the actual solutions and the etching time (30 s) used in our samples. The use of shorter times did not eliminate the etch pits. Note that most holes, although rounded from the high-temperature diffusion processes, appear faceted, consistent with the cubic structure of STO. From these results it seems that our STO substrates are characterized by defects that react to the acid attack: substantial chemical inhomogeneities (large amounts of Sr-O) or large numbers of structural defects like dislocations are likely to produce such etch pits. Indeed, identical treatments on different substrates such as the one from Fig. 2.10 showed a remarkably smooth surface with very few etch pits and holes, thus confirming our hypothesis. The critical point here, therefore, is the starting quality of the substrate.

We conclude from the above study that both the *standard treatment* and the *chemical etching plus annealing* process are capable of producing clean STO surfaces with well defined step-terrace morphologies. The latter also yields a single termination. However, the original miscut of the sample and its quality (e.g. the presence or absence of dislocations and other defects) will eventually determine the roughness and the presence of etch pits. In general, the standard treatment appears sufficient for having smooth and atomically flat STO surfaces, appropriate for the subsequent growth of LSMO.

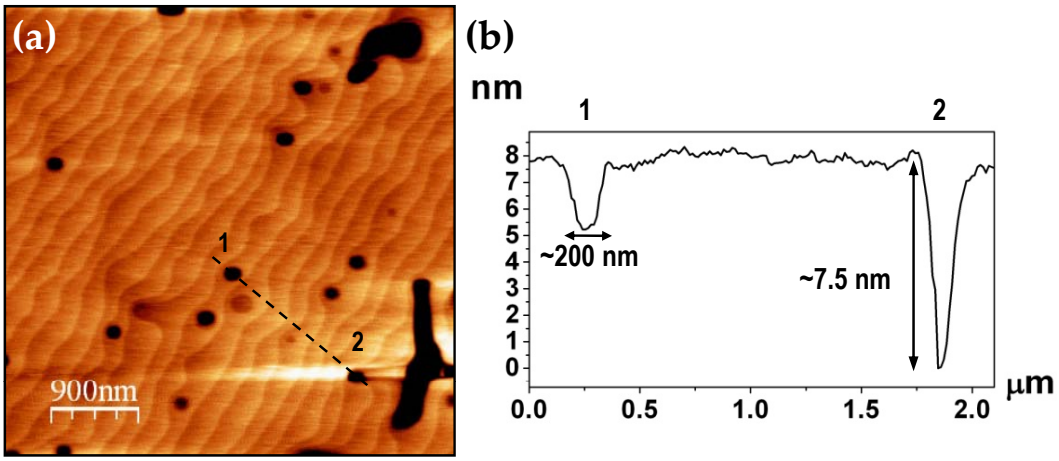

Fig. 2.9: *(a) 4.7µm × 4.7µm AFM topography image of an etched and annealed STO substrate displaying smooth steps along with holes from the acid attack. The image is thresholded in order to better distinguish the step-terrace morphology, the scale in z is ∼10 nm. (b) Line profile along the dashed line in (a) showing typical dimensions of the etch pits. Such holes can go as far as ∼20 nm into the crystal.*

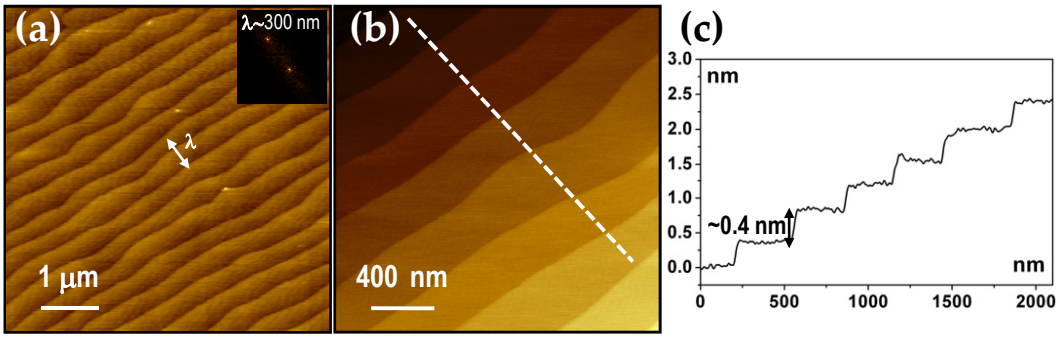

Fig. 2.10: *(a) 5.5µm × 5.5µm AFM topography image of an etched and annealed STO substrate displaying smooth steps and no visible holes from the acid attack. The Fourier Transform of the image shows the periodicity of the terraces, ∼300 nm wide. Scale in z is ∼3 nm. (b) 2µm × 2µm topography image of the same STO substrate. (c) Line profile along the dashed line in (b). The step corresponds to a single unit cell in height indicating single termination.*

The standard treatment described for STO was analogously applied to LAO substrates, for which no specific step-terrace forming procedure was available in the literature. We applied such a treatment in a great number of substrates, with very reproducible and satisfactory results. Contrary to STO, LAO substrates nearly always presented smooth and well

defined step edges, with unit-cell high steps. Fig. 2.11 presents the corresponding AFM image of a LAO substrate after the *standard treatment* and a line profile showing one unit-cell high steps. The etching procedure designed for STO was also tried on LAO substrates. Expectedly, neither an improvement nor a damage in the form of etch pits were observed, as such procedure specifically attacks the Sr-O termination.

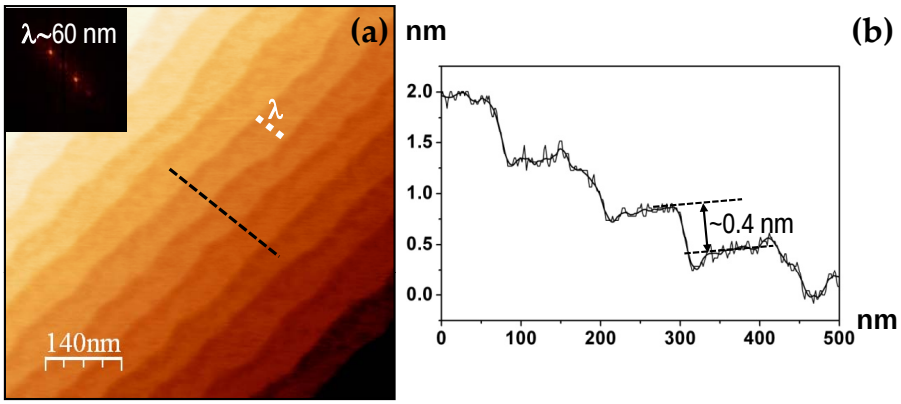

Fig. 2.11: *(a) 700 nm × 700 nm AFM topography image showing the λ ∼60 nm wide LAO terraces of a substrate after the standard treatment. (b) Line profile along the dashed line in (a) showing the unit cell step height.*

In (001)-LAO, the alternatively stacked La-O and Al-O_2 planes are positively and negatively charged, respectively. Several works point to the tuning of surface termination with temperature and atmosphere [11, 125–127]. In most cases, the annealings are performed in ultra-high vacuum chambers which is believed to favor La-O termination (poorer in oxygen) [125]. In contrast, in the X-Ray Photoelectron Spectroscopy (XPS) studies done in collaboration with Dr. J. A. Martín-Gago and Dr. Lidia Martínez (ICMM-CSIC Madrid), our air-treated LAO substrates showed a surface rich in Al, independent on whether the treatment atmosphere was oxidizing or reducing (Fig. 2.12). Specifically, the *La/Al* ratio decreased from ∼0.7 in the *as-received* substrates, to ∼0.3 in the substrates treated in O_2, Ar-H_2, or by successive oxidizing and reducing treatments. It is also worth noting that the oxidizing treatment promotes carbide formation, and how the carbide proportion has significantly decreased after the reducing treatments. The contamination carbon (C-C), on the other hand, remains constant, possibly because the surface was always measured after exposure to air. Besides, the morphology images in Fig. 2.13 show that no remarkable differences arise in the LAO substrates when heat-treated under different atmospheres, i.e. thermal energy appears to be the principal source of surface smoothening and step-terrace formation.

2.2.2 (001)-MgO surfaces

Regarding MgO substrates, abundant literature exists on their surface preparation and characterization, prompted by their wide use in film epitaxy and as support for metal particle growth. Already in 1990, Duriez and co-workers refer to many previous studies of UHV-cleaved and air-cleaved MgO crystals [128]. They also provide a comprehensive structural characterization using He diffraction, Auger electron spectroscopy, and Pd decoration to assess the crystallographic order, cleanliness and micro-topography of MgO sur-

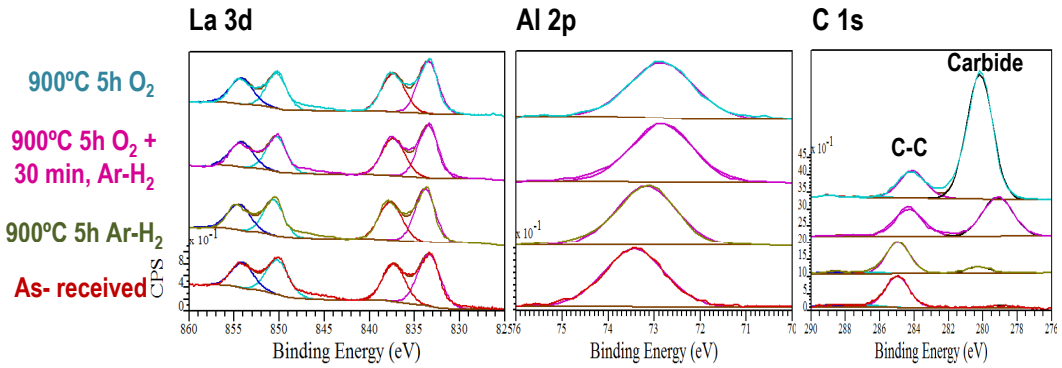

Fig. 2.12: *La 3d, Al 2p, and C 1s core level spectra as measured from XPS for heat-treated LAO surfaces (900°C) under different atmospheres. The area-calculation gives a* La/Al *ratio of ∼0.7 for the as-received and of ∼0.3 for the heat-treated surfaces. Note how the carbide content is maximum in the oxidized LAO and gradually decreases for reducing atmospheres.*

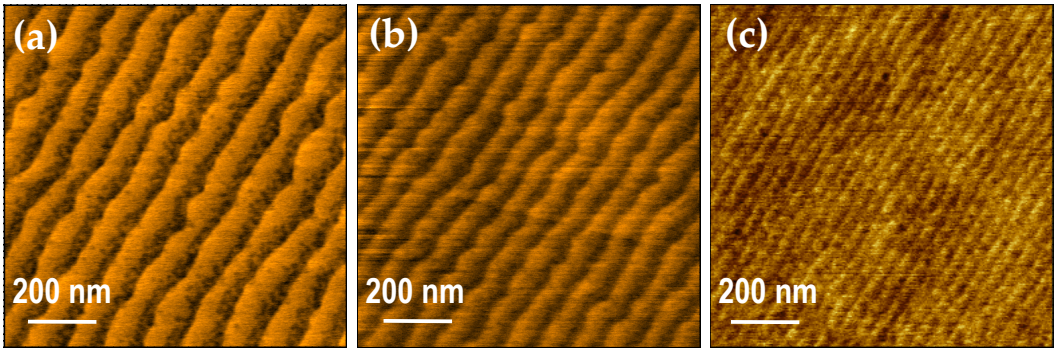

Fig. 2.13: *(a) 1$\mu m \times 1\mu m$ AFM topography images of heat-treated (900°C) LAO surfaces after (a) 5 h in O_2 atmosphere, (b) 5 h in Ar-H_2 atmosphere, (c) 5 h in O_2 plus 30 min in Ar-H_2 atmosphere.*

faces. A strong tendency from such surface towards water chemisorption and reaction, as well as towards ambient CO_2 adsorption are also described, in agreement with more recent theoretical and experimental works [129–132].

Fig. 2.14 shows AFM topography images of two different MgO substrates processed using the *standard treatment*. Little change is observed on their flat and step-free surfaces, although the presence of small pits (a representative pair is marked with green circles) seems larger before the annealing. Nevertheless, the root mean square (RMS) roughness actually increases a bit, from 0.2 nm to 0.3 nm, after annealing is performed. This is also the reason why the pits are less visible in the latter case, although their depth does not change (∼1.5 nm). Fig. 2.14 (b) displays a different substrate, which was not annealed, and that presents a very flat surface with neither terraces nor pits (RMS roughness 0.16 nm).

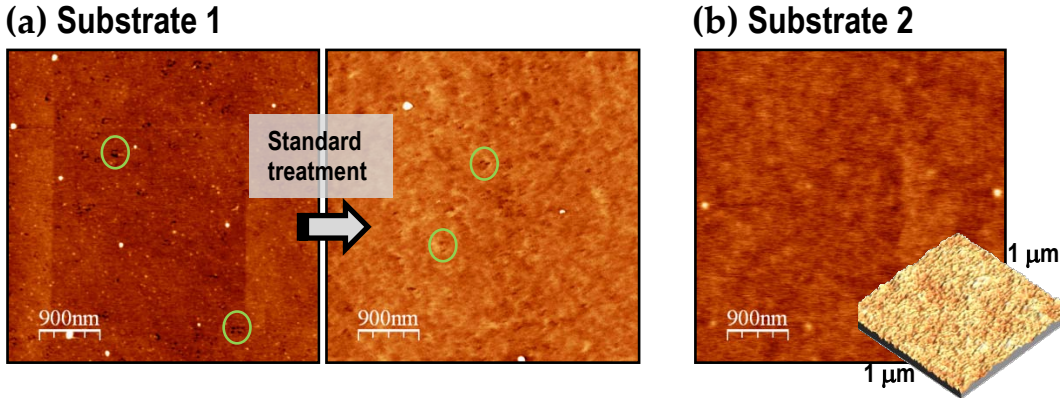

Fig. 2.14: *4.5µm × 4.5µm AFM topography images of two MgO surfaces. (a) Surface morphology of an organic-solvent cleaned MgO without thermal annealing (left) and after the 5 h treatment at 900°C in oxidizing atmosphere (right). (b) A different MgO substrate after just the acetone and methanol cleaning. z scale is ∼3 nm, ∼4.3 nm, and ∼2.4 nm (left to right).*

A large variety of surface morphologies have been described in the literature concerning the evolution of MgO with annealing temperature, time and atmosphere. Step-terrace morphologies, smoothening, or, conversely, considerable roughening (with microcrystal diffusion from the bulk) are among the features that have been reported [133, 134]. For instance, a diffusion-driven increase of terrace width has been observed after longer annealing times, while the terraces tend to narrow at higher temperatures due to evaporation processes [134]. These works also give a threshold temperature of 1000°C for the onset of step-terrace morphology formation, which is consistent with our findings at a lower temperature (900°C). However, the spread in the treatment parameters that were used in various literature works to achieve particular morphologies highlights the importance of the substrate quality. This includes the manufacturing conditions (whether it is air or UHV-cleaved), the presence of defects and impurities, and surface contaminants.

2.2.3 (001)-YSZ surfaces

A representative example of the effect of different treatments on YSZ substrate surfaces is shown in Fig. 2.15. Similar to MgO, YSZ substrates show no changes after the standard heat treatment [Fig. 2.15 (a)]: very flat and clean surfaces of RMS roughness ∼0.14 nm

are observed in both cases. Surface steps of width λ can also be inferred (their orientation is marked in green dashed lines in the image). This is further confirmed by the Fourier transform, from which an average terrace width λ $\sim$60 nm is deduced. A different as-received YSZ substrate shows identical characteristics (Substrate 2, cleaned with acetone and methanol just like Substrate 1), although steps here are very narrow and the image too large to be able to find the exact terrace size. In contrast, two other substrates (3 and 4), subject to a 1000°C annealing in oxygen for half of the time (0.5 l$\cdot$ min^{-1}, 2.5 h), display a clearer step-terrace morphology with very narrow terraces ($\lambda\sim$44 nm). Notice also how some of the steps, instead of being straight, meet at one point (some of these features are evidenced by green circles). Such coalescence has already been reported, although it was only observed at higher temperatures [135]. Substrate 3 appears homogeneously covered by similar round particles ($\sim$8 nm and $\sim$50 nm in height and diameter, respectively). Conversely, Substrate 4, from a different batch, did not exhibit such particles after undergoing an identical treatment as Substrate 3. On the contrary, it showed a remarkable cleanliness, hence ruling out the possibility that such treatment would produce segregation from the bulk.

In short, the cut and polished YSZ substrates used in this work came with little defects and showed highly planar surfaces. They can be either cleaned or cleaned and heat-treated (if further contaminant removal is desired), and they tend to form very narrow and smooth terraces, better reconstructed at 1000°C. A greater variety of morphologies, from planar surfaces to surfaces with holes or self-organized nanostructures was reported in the literature [136]. This again emphasizes the critical role of the quality of the substrate, determined by the growth and polishing methods used by the supplier.

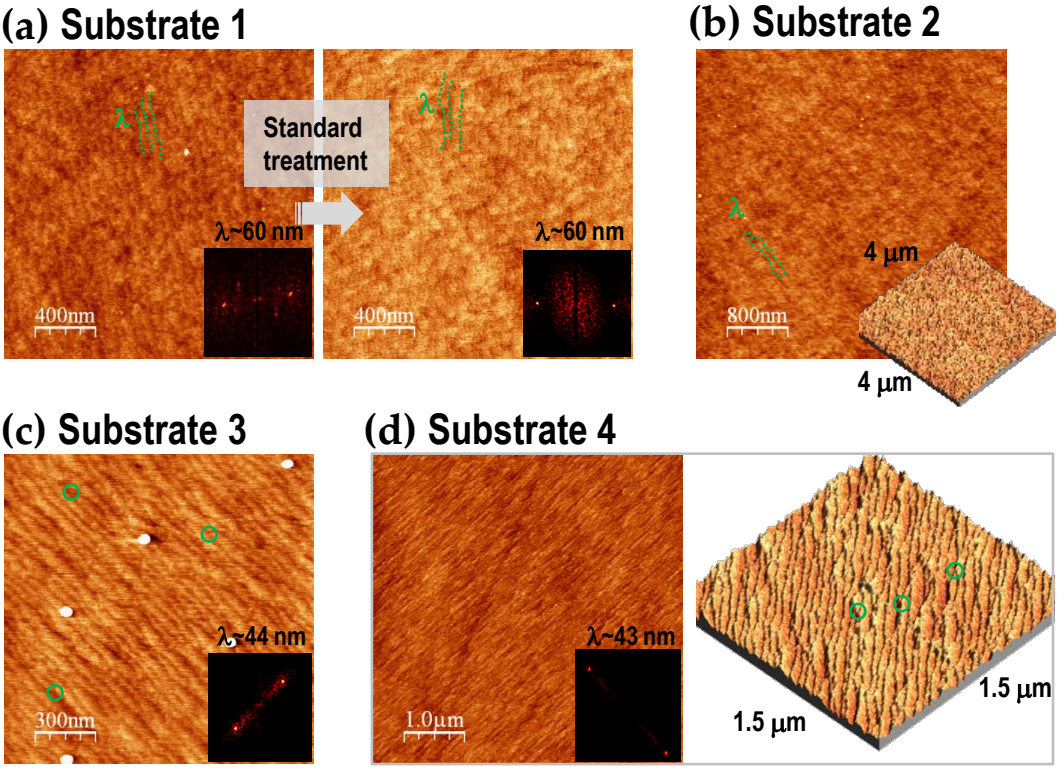

Fig. 2.15: *(a) 2μm × 2μm AFM images of an acetone and methanol-cleaned YSZ substrate before (left) and after (right) 5 h annealing at 900°C in O_2. The surfaces look identical except for a slightly greater presence of dirt particles in the non-annealed substrate (not shown). The step periodicity is observed, with indicative dashed green lines marking the terrace limits and the Fourier transforms of the images giving the spacing between them (∼60 nm). Scale in z is ∼1.4 nm in both. (b) 4μm × 4μm image of a different substrate just after the acetone and methanol bath, which shows little difference with respect to Substrate 1. RMS values are ∼0.13 nm and ∼0.16 nm (Subs. 1 and 2, respectively). (c) and (d) correspond to a 2.5 h 1000°C annealing in O_2 of two more YSZ substrates. Step-terrace morphology is more clearly discerned here than in (a) and (b), though terraces appear narrower (∼44 nm). Note also the coalescence of steps, some of them marked with green circles in (c) and in the 3D detail of (d). RMS values are very low, around 0.13 nm, z scale is ∼1.4 nm.*

2.3 Chemical Solution Deposition growth of $La_{0.7}Sr_{0.3}MnO_3$ films and nanostructures

In this section we describe the chemical solution deposition (CSD) method applied to the growth of $La_{0.7}Sr_{0.3}MnO_3$ nanoscale films and 3D nanostructures.

Our $La_{0.7}Sr_{0.3}MnO_3$ (LSMO) precursor solutions were prepared following the 'all-propionate' route described by Hasenkox et al. [137]. Briefly, stoichiometric amounts of metal propionates are mixed and dissolved in propionic acid under ambient conditions, stirred up for 30 min at room temperature and filtered with a 0.2 μm diameter filter. The initial solution concentration, 0.3 M with respect to the Mn, is diluted down to concentrations in the 0.006 M to 0.1 M range. The metal propionates used, i.e. $La(OOCC_2H_5)_3$, $Sr(OOCC_2H_5)_2$ and $Mn(OOCC_2H_5)_2$, are synthesized from commercially available acetates (Aldrich) in a large excess of propionic acid (Aldrich). The solution chemistry, hence, is kept simple and the main goals of the CSD route are achieved: inexpensive starting compounds, adjustability of concentration and stoichiometry, as well as solution handling at ambient atmosphere [137]. The solution at 0.3 M concentration has a viscosity of 2.5 mPa · s which falls down to 1 mPa · s for 0.03 M concentration (precisely the viscosity of the propionic acid solvent). Contact angle measurements of the 0.03 M solution on the STO, LAO, YSZ and MgO substrates, both as-received, and after the *standard treatment* gave values below 15°, i.e. the solution perfectly wets all of the substrates, also independent of the treatment.*

After the synthesis, 14 μl of precursor solution are deposited onto a clean and atomically flat substrate (see section 2.2), positioned at the center of the rotatory plate of a commercial spin-coater. The substrate attains 6000 rpm rotational speed in 1 s, which is kept constant for 2 min. At the end of the process the solvent has evaporated and the substrate appears covered with a homogeneous gel layer. Under identical deposited volume, angular velocity, acceleration, and spinning time, we expect the amount of deposited material to be the same, since the wettability is the same for all substrates. The main source of differences regarding the material quantity are rather small variations in the deposited volume. This is easily expected because the deposit is done by hand, approximately aiming for the center of the substrate.

The spin-coated sample is placed in an alumina covered crucible which is put inside a quartz tube, previously cleaned with water, soap and acetone. The tube is introduced in a high temperature furnace where metalorganic precursors decompose (∼300°C-400°C [138]) and the subsequent LSMO crystallization occurs (high temperatures $\gtrsim$ 700°C). The experimental conditions are tuned by modifying the growth temperature, the heating ramp and the dwell duration [see Fig. 2.16 (a)]. Rather slow heating and cooling ramps were used, $3°C \cdot min^{-1}$. Annealing was done in air and oxygen atmosphere (the latter typically at a flowing rate of $0.6\,l \cdot min^{-1}$, regulated with a mass-flow controller). Oxygen flow was introduced at around 800 °C and removed again at the same temperature during the cooling ramp. Both the slow ramp and the atmosphere settings were taken from previous works done in the group. Such studies optimized the parameters for the growth of magnetoresistive LSMO thin films [139, 140].

*Meaningful differences among contact angle values are only considered above ∼15°. We cannot resolve differences for smaller values, in practice saying that the solution *completely wets the substrate*.

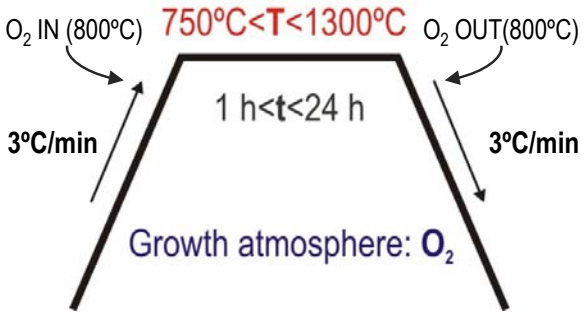

Fig. 2.16: *Typical heat treatment parameters for the generation of epitaxial* LSMO *on single crystal substrates. The O_2 flux was 0.6 $l \cdot min^{-1}$.*

2.4 Conclusions

In summary, we have introduced the principal characteristics of the oxide single crystal substrates used in this work. Along with a state-of-the-art on oxide surface conditioning, we have described our own strategy, mainly based on heat treatments performed at high temperature (900°C), ambient pressure, and under flowing oxygen. Such treatment succeeds in generating well-defined step-terrace morphologies in both STO and LAO substrates. In the case of LAO, it produces Al-rich surfaces with a considerable amount of carbides. The carbide content was seen to decrease when the treatment was performed under Ar-H_2 reducing conditions, with no observable change in topography or in the surface chemistry, as seen by XPS. Performed after an acid etching, the so-called *standard treatment* further selects a single termination in STO. On the other hand, the flat and clean surfaces of MgO and YSZ did not undergo appreciable variations after the *standard treatment*, although YSZ demonstrated a clearer tendency towards step-terrace morphology. Such terraces, very narrow, appear slightly better formed when the heat treatment is done at a higher temperature (1000°C). In the following, all of the STO and LAO substrates will be heat-treated following the *standard treatment*, while for MgO and YSZ we will use one or the other, as-received or heat-treated substrates indistinctly. Regardless of whether the thermal treatment is performed or not, the sonication with acetone and methanol is invariably done to clean the substrates from contaminants. An important point to keep in mind is that substrate variations should be expected from batch to batch, and hence AFM inspections of their topography will be carried out as often as possible.

Chapter 3

Nanoscale $La_{0.7}Sr_{0.3}MnO_3$ on single crystal oxide substrates

As outlined in the Motivation of this thesis, we establish the framework of our study in the context of nanoscale oxide heteroepitaxys, where the atomic arrangement of the substrate crystal determines the growth of the crystalline film on top. The procedure to chemically grow $La_{0.7}Sr_{0.3}MnO_3$ (LSMO) on top of single crystal oxide substrates was just described in Chapter 2. Whether this LSMO grows in a 2D film or in a 3D nanoisland form, epitaxial or random, strained or relaxed. . .etc., will define the functional properties of the system. In the present chapter we give the general description in terms of morphology, epitaxy, microstructure, and macroscopic magnetic performance of solution-derived LSMO nanoscale systems grown onto a variety of (001)-oriented single crystal substrates. Such oxide substrates, recently explained, include the perovskite-type $SrTiO_3$ (STO) and $LaAlO_3$ (LAO), the fluorite-type YSZ, and the rock-salt MgO. The influence of the substrate in the final heteroepitaxy, or, more specifically, the key role of the film-substrate interaction, is evidenced soon enough: the same ultra-diluted precursor solutions, under identical heat treatments, yield two disparate landscapes: atomically flat <10 nm thick LSMO films are obtained on STO and LAO single crystals while onto YSZ and MgO, the result is an homogeneous dispersion of self-assembled LSMO nanoislands. We have divided the chapter into these two naturally differentiated blocks: we start by addressing the main characteristics of ultrathin LSMO films grown on STO and LAO and devote the second part of the chapter to the analysis and description of self-assembled LSMO nanoislands.

3.1 Heteroepitaxial growth basics

The word *epitaxy* comes from the Greek, where *epi* means 'located on' and *taxis* means 'arrangement'. We understand epitaxial growth as the growth of a crystal (the film material) on top of another crystal (the substrate material) in such a way that the atomic arrangement within the substrate continues within the film on top. An epitaxial film-substrate interface thus implies that atoms of the film material will occupy lattice positions of the substrate and vice versa [141]. If film and substrate are the same material we talk of *homoepitaxy*, while the opposite case is known as *heteroepitaxy*. From a thermodynamic perspective, het-

eroepitaxial growth is commonly described in terms of the free surface/interface energies of substrate and film, and of their elastic strain energy.

The generation of a free surface involves the breaking of chemical bonds, with the consequent net increase of energy of the system. ***Surface free energy*** γ is hence directly related to the reversible work dW done on a material when its surface area is increased by dA, i.e. $dW{=}\gamma dA$ [141, 142]. Similarly, the chemical bonding between the atoms in the film and in the substrate also has an energy associated, the interface energy, which is less than the sum of their individual surface energies. Young's equation, $\gamma_s{=}\gamma_{fs}{+}\gamma_f\cos\theta$, is derived from minimizing the surface energy required to generate a spherical cap island (like the one sketched in Fig. 3.1) with respect to the wetting angle θ [141]. The relative values of the surface free energy provide a first classification of the *growth modes* in heteroepitaxial systems [143]: the film will grow layer by layer if $\gamma_s{>}\gamma_{fs}+\gamma_f$ (also known as Frank-van der Merwe or 2D growth) [144], or it will start by generating 3D islands if $\gamma_s{<}\gamma_{fs}+\gamma_f$, following the so-called Volmer-Weber growth [145]. A combination of 2D and 3D growths can also occur, known as Stranski-Krastanov growth mode [146], which typically implies the presence of lattice mismatch between the film and the substrate.

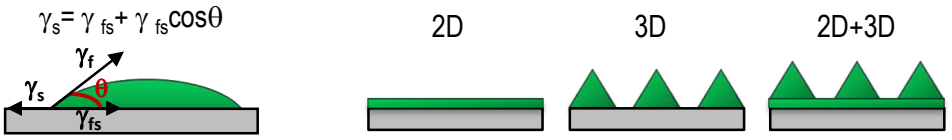

Fig. 3.1: *Liquid nucleus in equilibrium model. Young's equation represents the balance among the different components of the surface free energy γ. The growth mode can be 2D, 3D, or a combination of both, depending on the relative values of the substrate (γ_s), film (γ_f), and interface (γ_{fs}) surface energies.*

Lattice mismatch ϵ (Eq. 3.1) refers to the difference in lattice parameter between the film and the substrate, i.e.

$$\epsilon = \frac{a_s - a_f}{a_f} \tag{3.1}$$

where a_s and a_f are the equilibrium parameters of the substrate and film, respectively. ϵ is directly related to the other essential component in heteroepitaxial growth, the ***elastic strain energy*** $E_{elastic}$, which scales like $E_{elastic}{\sim}\epsilon^2$ with the lattice mismatch [141, 147]. In a 2D + 3D-like growth as the aforementioned, the film will initially grow adapting its in-plane lattice constant to the bulk substrate lattice constant. As the film grows thicker the elastic strain energy associated to the film deformation also increases. The formation of 3D islands provides a way for relaxing the built-up elastic energy: the upper lattice planes within the island can relax towards their intrinsic lattice constant because they are no longer constrained in the direction parallel to the interface [see Fig. 3.2 (a)]. The greater the island volume, the greater will be the relaxation provided with respect to a film of equal volume. And, for the same island, its volume strain relaxation is larger for the case of smaller lateral size to thickness ratio D/t [Fig. 3.2 (b)]. On the other hand, the generation of 3D structures implies an additional cost in surface energy, which scales with the area of the island. The trade-off between the energy gain due to island relaxation and the energy cost due to the new surface formation will determine whether the 2D to 3D transition occurs or not. This simplistic model neglects the kinetics of the process, such as material transport issues from one state to the other (which will, in turn, depend on the temperature, pressure, etc.) [148].

In addition to 3D island formation, a typical strain-relieving mechanism is the generation of misfit dislocations, i.e. the dislocations formed at the interface between substrate and film. It has been shown that the barrier to generate dislocations is proportional to ϵ^{-1}, while it scales with ϵ^{-4} for the generation of 3D islands [149]. In other words, the generation of islands is enhanced in large lattice-mismatched systems.

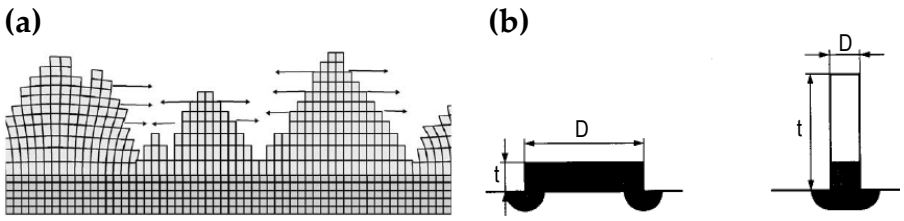

Fig. 3.2: *(a) Volume strain relaxation is achieved by 3D coherent (non-dislocated) nanoislands. Arrows indicate the direction of the elastic strain relaxation. Reproduced from [150]. (b) For a fixed nanoisland volume, coherent 3D nanoislands are capable of larger elastic relaxation in the case of low* D/t *values. Reproduced from [147].*

The driving force for the spontaneous ordering of nanostructures on a crystal surface is the long range elastic interaction. Such elastic interaction is caused by the strain fields that a 3D island exerts on the substrate due to island/substrate lattice mismatch. For instance, a compressively strained island on a substrate (a_f<a_s) will tend to expand along the direction parallel to the interface. The substrate will react against this tendency by compressing itself along the free surfaces adjacent to the edges of the island (see Fig. 3.3) [151]. The substrate strain fields cause islands to interact repulsively with each other, thus limiting coarsening processes. In this context of strain-driven structure formation we refer to *self-assembly* when the spontaneous features exhibit a narrow size distribution and we talk of *self-organization* when the structures show an additional tendency to form ordered arrays [150]. The substrate-mediated interaction between islands is sometimes neglected in self-assembled diluted nanoisland systems (nanoisland size $\ll$ nanoisland separation), but it cannot be ignored for denser arrays of nanostructures. This term includes, among others, the isotropic/anisotropic nature of the medium, the lattice mismatch, or the island to island distance [152]. Theoretical studies have demonstrated its effect on coarsening processes of nanoislands, while experimental results point at its influence on the shape transition of semiconductor heteroepitaxys [153].

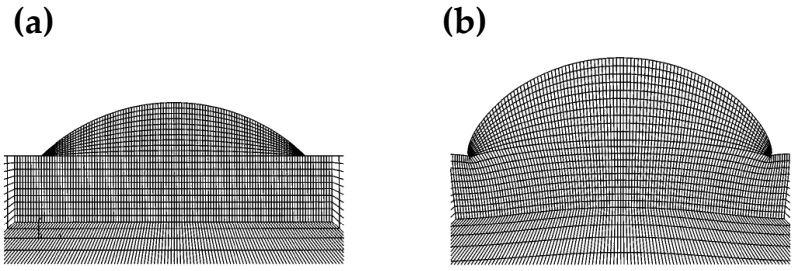

Fig. 3.3: *Finite element simulations of island and substrate. (a) Undeformed mesh showing the spatial island and substrate discretization. (b) The mesh deforms as a result of the mismatch strain between the island and the substrate. Reproduced from [151].*

At the beginning of the chapter we have anticipated that, under equal processing parameters, LSMO grows into a 2D film on STO and LAO substrates, whereas it arranges spontaneously into self-assembled nanoislands in the case of YSZ and MgO substrates. Equal processing conditions include the use of identical solution concentration, spin-coating parameters, growth ramps and temperature, annealing times, and atmosphere. The solution wettability of the different substrates was also tested to be the same. Equilibrium theories of heteroepitaxial growth based on the energetic concepts of surface and elastic strain energies depicted above provide the tools for evaluating whether the equilibrium state of the system is, effectively, 2D or 3D. Kinetic effects will then make the real observed system deviate more or less from the one predicted by thermodynamics [150]. Surface energy contributions can be calculated from analytical expressions, given a specific island shape [149, 154, 155]. Analytical expressions for the elastic strain energy of islands have also been derived [154–156]. The total energy of a system of islands is also influenced by other terms such as the interaction between islands explained above (more important the closer the islands are), and the contribution of island edges, which is short-range and positive. The latter, for simplicity, can be sometimes neglected [154], but it has also been explicitly taken into account, as in the work by Shchukin and Bimberg [147]. The application of the existing energetic models has been successfully used in our group for predicting shape selection and thermodynamic stability of strain-driven cerium oxide nanoislands grown on LAO [157]. There are no data, however, concerning the surface energy of LSMO, a multicomponent oxide with the additional complexity of having different possible surface terminations. The $(001)_{\mathrm{LSMO}}$ surface, for instance, could in principle have the Mn-O or the (La,Sr)-O_2 termination. Even if we could base the analysis on the scarce surface free energy data for other manganite systems like $La_{1-x}Ca_xMnO_3$ [158], there remains the generalized lack of knowledge regarding interface energies. The distinct nature of perovskite-perovskite, perovskite-fluorite, and perovskite-rocksalt interfaces suggests that the interface energy plays a substantial role in deciding the final heteroepitaxial configuration of each of our systems.

Part I

$La_{0.7}Sr_{0.3}MnO_3$ on perovskite-type substrates

The present section is concerned with the results of the growth of LSMO, by means of chemical solution deposition (CSD), onto STO and LAO perovskite-type substrates. As seen in the previous chapters, both LSMO and the chosen single crystal substrates have perovskite structure. The difference in lattice parameters between LSMO ($a_{LSMO} = 3.873$ Å) and STO ($a_{STO} = 3.90(7)$ Å) is very small, yielding a nominal tensile lattice mismatch of ϵ=(a_{STO}-a_{LSMO})/(a_{LSMO}) ∼0.9%. For LAO ($a_{LAO} = 3.79(2)$ Å), the lattice mismatch changes sign to compressive, with a larger magnitude of ϵ=(a_{LAO}-a_{LSMO})/(a_{LSMO}) ∼-2%. As anticipated in the introduction to this chapter, we find that CSD growth of ultradiluted LSMO solutions on STO and LAO yields ultra-thin films. We will describe these two systems in parallel, starting by the morphological and structural characteristics of the ultra-thin LSMO films and ending up by giving the main points regarding their magnetic and electrical properties.

3.2 Morphology and microstructure of ultra-thin LSMO films on STO and LAO

3.2.1 Morphological characteristics

For the growth of LSMO on top of perovskite-type STO and LAO substrates we followed the steps described in section 2.3 of Chapter 2. In brief, we used precursor solution concentrations in the 0.015 M-0.1 M range (in Mn) and spin-coated them onto STO and LAO single crystals. The subsequent annealing step was performed in a high temperature furnace under flowing oxygen, at 900°C for 1 h. Before the LSMO growth, the substrates were heat-treated according to the *standard treatment* procedure described in Chapter 2. We may recall that such treatment cleans the substrate surface from organic contamination and reconstructs the miscut surface into a step-terrace architecture.

LSMO on STO

The morphology of a LSMO film grown in such a way is shown in Fig. 3.4. The precursor concentration used was 0.03 M. Remarkably, the film entirely reproduces the underlying STO substrate step-terrace morphology, with atomically flat terraces and steps a LSMO unit cell (u.c.) high a∼4 Å. The root mean square (RMS) of the film is as low as half a unit cell (∼0.2 nm); this is comparable to the highest quality LSMO on STO films reported in the literature, e.g. grown layer-by-layer by pulsed laser deposition (PLD) [159]. The periodicity of the steps gives a terrace width λ of ∼110 nm, calculated from the Fourier transform of large atomic force microscopy (AFM) images [see Fig. 3.4 (b)].

It follows from Fig. 3.4 that the morphological features of the LSMO film are determined by the underlying substrate surface. Such influence is further confirmed by Fig. 3.5, where we show the AFM study of a bare STO substrate after the *standard treatment*. As remarked in Chapter 2, the wider the substrate terraces, the less effective is the thermal treatment in producing smooth, well-reconstructed terraces. This is the case of the STO surface in Fig. 3.5 (a), which exhibits rough edges and a great amount of small holes within the terraces. Expectedly, subsequent growth of LSMO [Fig. 3.5 (b)] results in a considerably rougher thin film than the one in Fig. 3.4, despite using identical processing conditions.

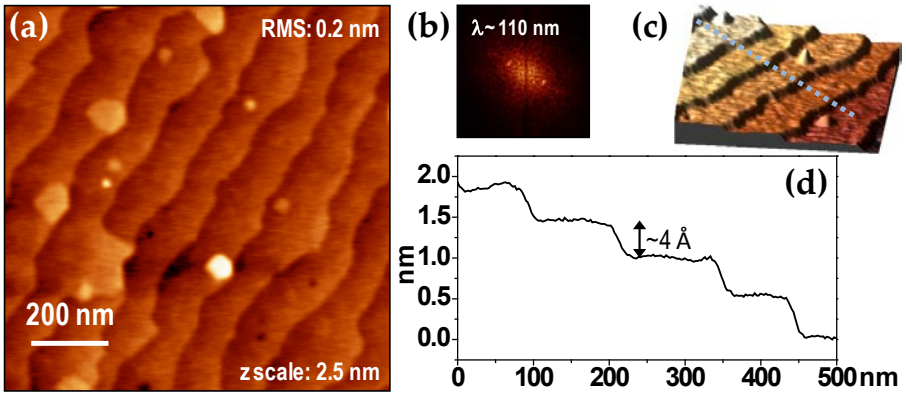

Fig. 3.4: *AFM topography analysis of a LSMO thin film grown onto a STO substrate (solution concentration 0.03 M and heat treatment at 900°C for 1 h.) (a) 1$\mu m \times 1\mu m$ AFM image showing the step-terrace morphology of the film, inherited from the underlying substrate surface. RMS roughness is ∼0.2 nm. (b) An average terrace width of λ∼110 nm is deduced from the Fourier transform of the AFM images. (c) 3D AFM image highlighting the staircase morphology of the LSMO thin film. (d) A line profile across the image in (c) reveals the height of the step is 1 unit cell.*

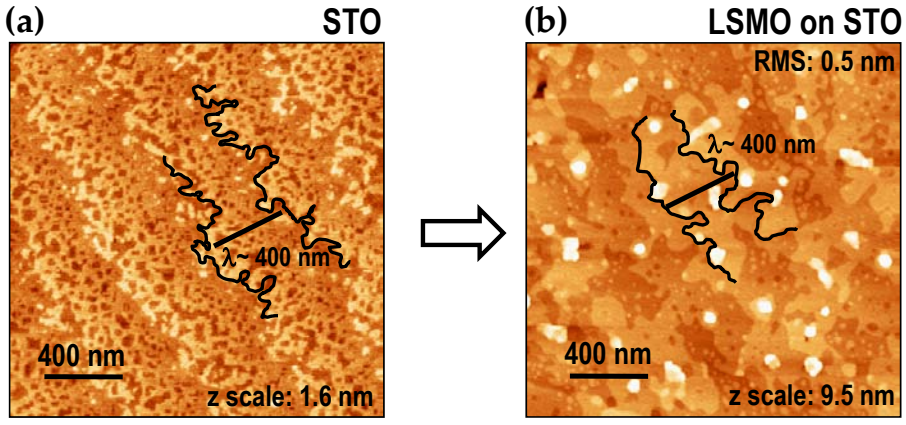

Fig. 3.5: *2$\mu m \times 2\mu m$ AFM image of a bare STO substrate after the thermal 'standard treatment' (a), and after the growth of LSMO on top of it (0.03 M, 900°C 1 h) (b). The rough edges and the presence of holes in the terrace give out a rougher LSMO film, compared to the film in Fig. 3.4.*

A natural question regarding these films, which reflect the architecture of the underlying substrate , is 'how thick they are'. We act upon the *film thickness* t by modifying the precursor solution concentration: the more concentrated the solution, the larger amount of material will crystallize, i.e. the thicker the film will be (provided that such material homogeneously covers the whole substrate surface). Previous works in the group have shown that LSMO precursor solutions from propionates with concentrations ∼0.3 M, (i.e. one order of magnitude above the actual solutions) result in LSMO films of t∼25-30 nm [140]. Our thin films, on the other hand, are too thin to be able to measure the step resulting from attacking part of the film. Nevertheless, the studies performed on self-assembled LSMO nanoislands grown from identical solution concentrations onto YSZ substrates, enable a rough calculation of the thickness values at these low concentrations. Such estimation is further supported by the extrapolation of the existing data for thicker films [140], and with the local measurements from transmission electron microscopy cross-sections (next section). Overall, we find that the average expected film thickness t for 0.015 M, 0.03 M, and 0.1 M precursor solution concentrations is around ∼1.5 (±0.5) nm, ∼3.5 (±0.5) nm, and ∼10 (±5) nm, respectively. The procedure for estimating these numbers in nanostructured LSMO on YSZ samples will be discussed later in section 3.4.1 of this chapter.

More examples of the various LSMO thin-film morphologies that we obtained depending on the underlying substrate surface, are displayed on Fig. 3.6. Note that we have included a film grown from a 0.015 M solution. We see that it also exhibits well-defined atomically flat terraces, as the films with twice the amount of material. All these films were treated at 900°C for 1 h, after evidence that higher temperatures and longer annealing times resulted in a de-wetting process, where bare substrate spots coexisted with film-covered spots.

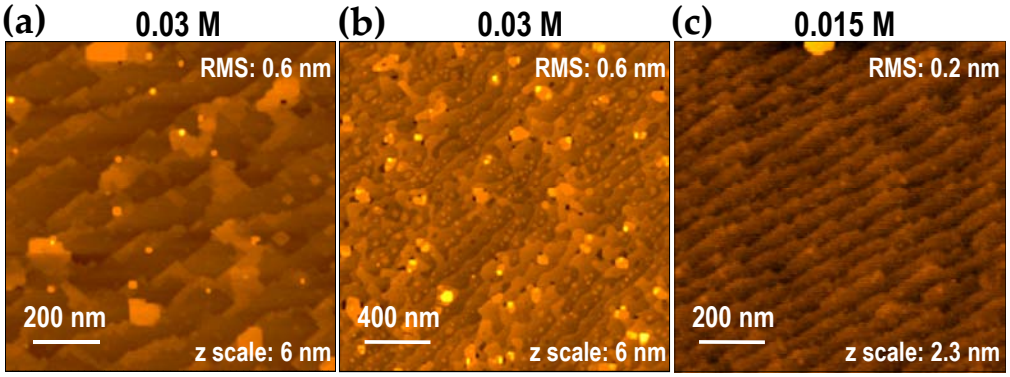

Fig. 3.6: *AFM topography analysis of three LSMO thin films grown onto three different STO substrates. The heat-treatment was 900°C 1 h for all.*

We have thus seen that the LSMO on STO ultra-thin film morphology is fully determined by the STO substrate surface underneath. The differences from one film to another simply reflect the substrate condition, from wider to narrower terraces, or from rougher to smoother films, depending on the quality of the substrate step-terrace structure. These results underline the high mobility of the LSMO/STO system at 900°C, with atoms finding their preferred positions, i.e. those which match the substrate crystalline structure. Furthermore, it would appear that the interface energy between LSMO and STO is very low: the lower the interface energy, the more 2D-like is the film growth, i.e. the smoother the

film tends to grow. The latter will be better understood in comparison with the 3D nanostructure results obtained on non-perovskite substrates, discussed in Part 2 of this chapter.

LSMO on LAO

Identical processing conditions were applied to the growth of LSMO thin films on LAO substrates, previously heat-treated as in the case of STO. Recall that the *standard treatment* of LAO substrates almost invariably led to well-defined stepped surfaces, displaying smooth terraces with well reconstructed edges, at variance with the less predictable STO surfaces (see Chapter 2). Remarkably, the resulting thin films were found to exhibit less reproducible morphologies than those obtained from LSMO on STO: not all of the films, although grown identically, reflected the underlying LAO step-terrace architecture. Fig. 3.7 shows three LSMO/LAO films (0.03 M) after 900°C 1 h heat-treatment. Narrow terraces can be easily distinguished in Fig. 3.7 (a) but not in Figs. 3.7 (b) or (c); in the latter samples the film surface shows either small islands (b), or holes (c), also evidenced in the line profiles below. We also observed that the films reproducing the underlying LAO surface have a tendency to segregate nanoislands as the ones, ∼20 nm high, seen in Fig. 3.7 (a). Such islands greatly increase the RMS roughness [∼2.4 nm for Fig. 3.7 (a)]. Although less pronounced, we also observed this same trend toward nanoisland segregation in LSMO on STO, where nanoislands had a typical height below ∼5 nm. Previous results in our group have reported the spontaneous outcropping of La-Sr oxide islands in the case of thicker LSMO films (t∼25-60 nm) grown on STO and LAO also by chemical methods [6, 140, 160]. Nevertheless, at this point, the specific composition of the nanoislands segregated in the present $t \lesssim 10$ nm ultra-thin films remains unclear.

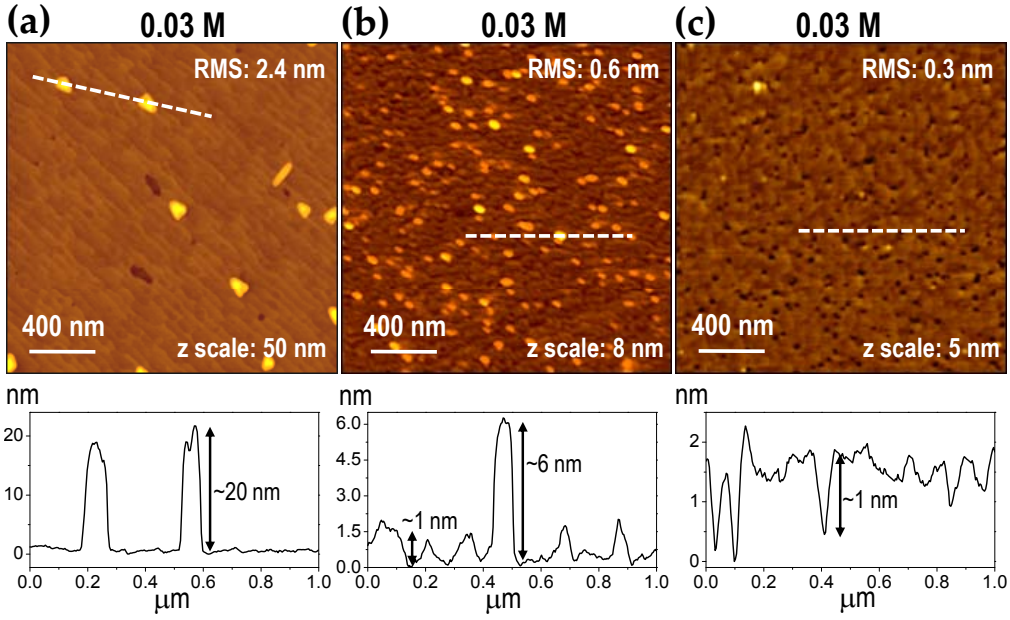

Fig. 3.7: *AFM topography analysis of three LSMO thin films grown onto three different LAO substrates, using 0.03 M solution concentrations and identical heat treatment of 900°C for 1 h. While (a) displays the underlying substrate step-terrace morphology, (b) and (c) exhibit rougher films with either little islands (b) or little holes (c). The outcropped islands in (a) are around ∼20 nm in height.*

Fig. 3.8 shows a magnified image of the step-terrace morphology exhibited by the sample of Fig. 3.7 (a). Note that an area featuring no outcropped nanoislands shows a very smooth surface, with RMS roughness of ∼0.2 nm and a low z height scale. Nevertheless, we also identify the presence of holes, with typical depths of around ∼1.5 nm, which correspond to around 4 LSMO unit cells. Besides, the heights of the LSMO film steps are not uniform, but combine instead integer and half-integer multiples of the LSMO unit cell, as observed in the line scan of Fig. 3.8 (b).

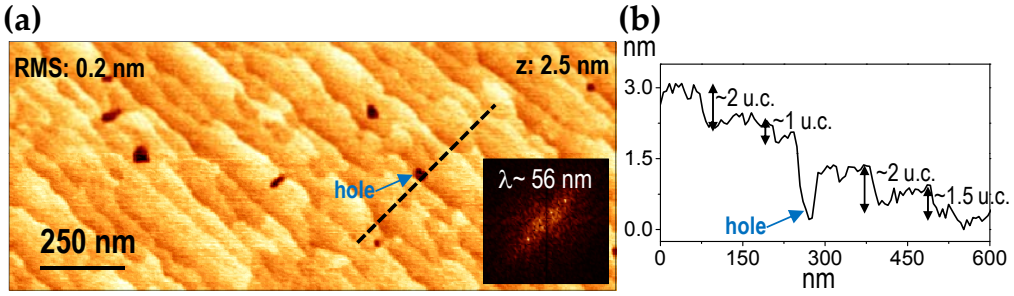

Fig. 3.8: *(a) AFM image of the sample in Fig. 3.7 (a) showing the detailed step-terrace morphology of the LSMO film. The terrace average width is λ∼56 nm. (b) Line scan along the dashed line in (a). The steps in the LSMO layer exhibit integer and half-integer multiples of the LSMO unit cell.*

We may conclude that, at variance with LSMO/STO ultra-thin films, LSMO/LAO films show a less predictable morphology, alternating step-terrace architecture with other rougher configurations that display small islands or even holes. The nominal lattice misfit for LSMO on LAO is notably larger than for STO (ϵ∼-2% against ϵ∼0.9%), in addition to changing sign from tensile to compressive. A tendency of the film towards relaxation caused by this larger strain energy could explain our observations of a greater surface disorder in LSMO/LAO systems. In other words, as a consequence of a partial or total relaxation, the film could exhibit a larger freedom with respect to the epitaxy imposed by the substrate, and, thus, a greater surface disorder. The main characteristics of the strain state of these ultra-thin films are examined in the following section.

3.2.2 Epitaxial relationship, strain, and microstructure

To be able to identify the LSMO structure we conducted X-ray diffraction (XRD) experiments (Theta-2Theta, phi-scans, and reciprocal space maps) and scanning transmission electron microscopy (STEM) cross-section analysis. The former, either using a X-ray diffraction standard diffractometer (Bragg-Brentano geometry) or a diffractometer with a 2D detector (GADDS D8, Advance System, Bruker) (see Appendix A), were unable to resolve the LSMO peaks in samples with 0.015 M and 0.03 M concentrations. The main difficulties stem from the small amount of material (which yields a low signal) and from the fact that the substrate peaks, very intense, fall next to the LSMO peaks. Nevertheless, we were able, in the case of LAO, to identify the LSMO peak in thin films grown from 0.1 M solution concentrations, which are expected to display a layer nominal thickness of around ∼10 (±5) nm. Fig. 3.9 shows the XRD intensity profile obtained from a phi-scan around the $(110)_{\mathrm{LAO}}$ reflection (2θ∼33.4°), for three different samples: a bare LAO substrate, heat treated at 900°C for 5 h following the *standard treatment* (named $\mathrm{LAO}_{s.t.}$), and two LSMO thin films grown on $\mathrm{LAO}_{s.t.}$ substrates from 0.05 M and 0.1 M LSMO solutions, heat-treated at 900°C

for 1 h. A shoulder is detected in the 0.1 M sample at a 2θ that coincides with the value expected for the $(110)_{\mathrm{LSMO}}$ reflection in bulk LSMO (2θ~32.7°). Since Theta-2Theta scans of the same film (not shown) give no peaks other than the (00l), (which are unidentified due to the proximity with the substrate) we can deduce that the LSMO grows epitaxially, i.e. $(001)_{\mathrm{LSMO}}||(001)_{\mathrm{STO}}$. A hint of a shoulder is also detected in the more diluted 0.05 M sample (red curve), but its resemblance with the tail from the substrate reflection (black curve) makes it difficult to unambiguously ascribe it to LSMO. We thus conclude that for 0.1 M concentrations [thickness t~10 (±5) nm] our XRD equipment is close to the limit of resolving the LSMO structure on LAO.

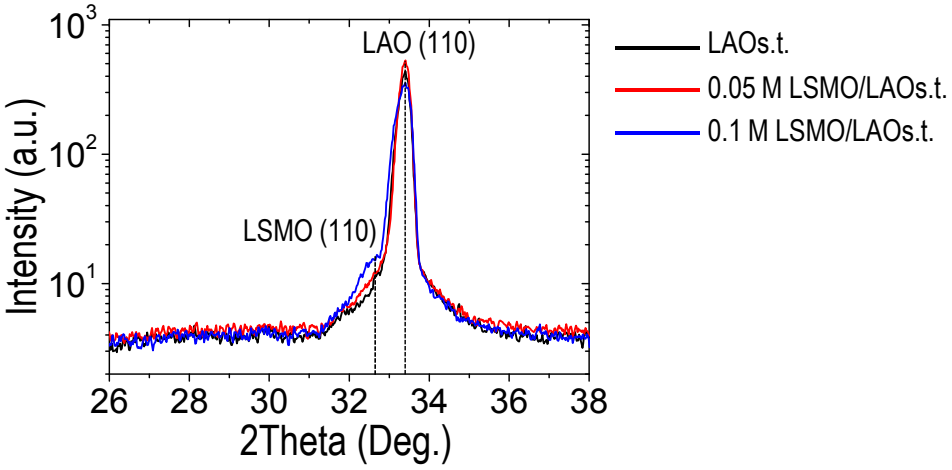

Fig. 3.9: *Comparison of the XRD measurements done around the $(110)_{LAO}$ reflection for three different samples: a bare LAO substrate after the standard heat treatment ($LAO_{s.t.}$), and two LSMO thin films grown out of 0.05 M and 0.1 M precursor solutions.*

The LSMO phase in samples from 0.03 M concentrations [nominal thickness t~3.5 (±0.5) nm] was identified by cross-section Z-contrast STEM studies*. Z-contrast imaging is indeed optimal for addressing the crystalline quality, the epitaxial relationship, as well as the strain state of nanostructures. Note that the contrast in a Z contrast image is roughly proportional to Z^2, Z being the atomic number of the imaged element. Consequently, heavy atom columns will appear brighter than those featuring light atoms. Fig. 3.10 shows two STEM images of a LSMO thin film (0.03 M) grown onto a STO substrate. The local thickness of the film derived from the image is t~2.4 nm (~6 u.c.). The film is highly crystalline and grows cube-on-cube on top of the STO substrate, i.e. $(001)_{\mathrm{LSMO}}[100]||(001)_{\mathrm{STO}}[100]$, which is precisely the configuration that yields the minimum lattice mismatch, ϵ~0.9%. The interface is abrupt and shows no structural disorder, i.e. no misfit dislocations are observed in scanned lengths as large as ~16 nm. These results indicate a fully strained film, where the LSMO has its bulk lattice value (a_{LSMO}~3.873 Å) slightly expanded in-plane in order to match the STO lattice parameter (a_{STO}~3.905 Å). In turn, such in-plane expansion results in the shrinking of the out-of-plane lattice parameter in an overall tetragonal distortion of the lattice.

It is expected that such ultra-thin LSMO films should be fully strained given their small thickness. Additionally, reciprocal space maps in CSD-grown ~25 nm thick LSMO

* Z-contrast imaging, high angular annular dark field (HAADF)-Z-contrast, or simply STEM will be indistinctly used throughout this chapter in reference to Scanning Transmission Electron Microscopy.

films on STO, done previously in the group, showed fully strained films [6, 140]. The Poisson ratio ν of a material relates its in-plane extension (compression) with the consequent out-of-plane compression (extension), by means of the expression ν=$\epsilon_{zz}/(\epsilon_{zz}$-$2\epsilon_{xx})$, where ϵ_{xx}=$(a_{xx}$-$a_{bulk})/a_{bulk}$ and ϵ_{zz}=$(a_{zz}$-$a_{bulk})/a_{bulk}$ are, respectively, the in-plane and out-of-plane deformations relative to the film bulk lattice parameter, (a_{bulk}=a_{LSMO}). Typical values for LSMO span from ν=0.34 [64] to ν=0.37 [65], which imply an out-of-plane lattice parameter between 3.840 Å and 3.835 Å (considering a fully strained LSMO film, i.e. a_{xx}=a_{STO}=3.905 Å). In addition to the strain state of the films, further data on the chemical composition of film and interface (for instance, on possible interdiffusion) can be obtained in principle from STEM measurements combined with EELS (electron energy loss spectroscopy). Such measurements are currently underway.

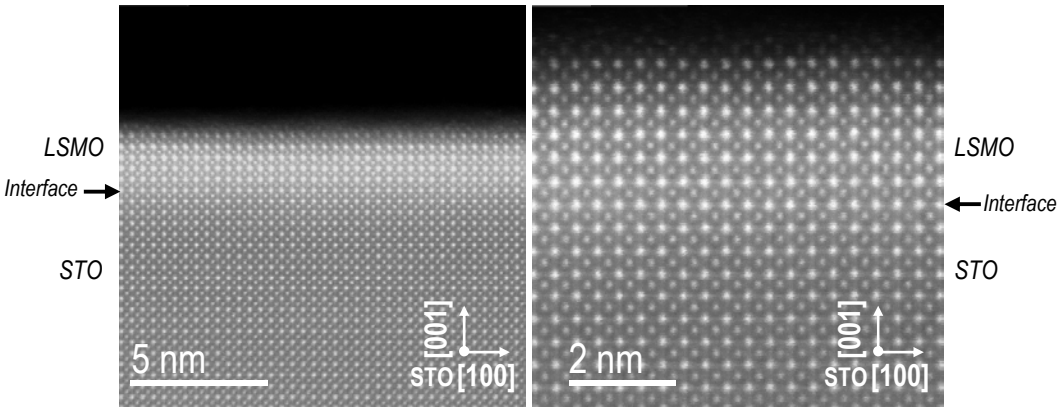

Fig. 3.10: *Z-contrast cross-section images of a LSMO thin film (t∼2.4 nm) on a STO substrate. The film grows coherently with a cube-on-cube epitaxy. Courtesy of M. Roldán and J.Gázquez.*

Analogously to LSMO on STO, LSMO films grown on LAO are also highly crystalline and show no secondary phases within the film matrix. Fig. 3.11 shows a Z-contrast image corresponding to the sample of Fig. 3.7 (a) and Fig. 3.8. Fig. 3.11 (a) reveals that the film has some discontinuities (recall the holes pointed out in Fig. 3.8), and that it is constituted of flat terraces of various thickness, with values mainly between 2-7 nm. A closer inspection of one of the terraces [Fig. 3.11 (b)] shows the transition from a region with bare substrate (a hole) to a LSMO terrace, which appears faceted in the $(101)_{\mathrm{LSMO}}$ lateral and the $(001)_{\mathrm{LSMO}}$ top planes. Remarkably, all of the steps present in the film exhibit lateral facets oriented along the $(101)_{\mathrm{LSMO}}$ crystallographic plane, suggesting that their surface energy is comparable to the surface energy of the $(001)_{\mathrm{LSMO}}$ planes. This is surprising as the {100} planes are commonly assumed to be the least energetic in other perovskite structures such as STO [161]. Concerning the epitaxial orientation, LSMO grows on LAO with a cube-on-cube epitaxy, i.e. $(001)_{\mathrm{LSMO}}$[100]||$(001)_{\mathrm{LAO}}$[100], as on STO. At variance with STO, however, films on LAO exhibit misfit dislocations with Burgers vector $\vec{b}$=a$_{LAO}$[100], spaced at distances ∼17 nm, in good agreement with the theoretical $|\vec{b}|/\epsilon$∼18 nm distance expected for a complete misfit relaxation of the film. Fig. 3.12 shows a high magnification STEM image of the LSMO film on LAO, featuring two misfit dislocations at the interface. Note that the presence of the dislocations produces a bending of the film surface. Such dislocations are easily detectable after Fourier filtering the image. As for LSMO on STO, EELS chemical analysis is currently underway for LSMO on LAO.

In summary, CSD-grown LSMO ultra-thin films on STO and LAO substrates (t∼2-5

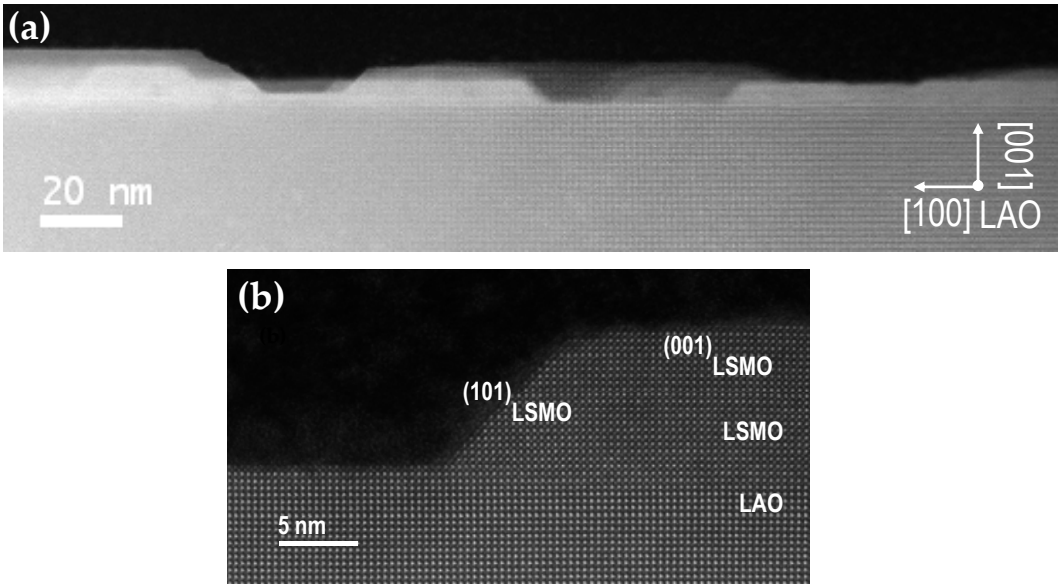

Fig. 3.11: *Z-contrast cross-section images of a LSMO thin film on a LAO substrate. (a) The film grows with a cube-on-cube epitaxy and features various thicknesses in the 2-7 nm range. (b) The LSMO terraces are faceted in the $(101)_{LSMO}$ lateral and $(001)_{LSMO}$ top planes. Courtesy of M. Roldán and J.Gázquez.*

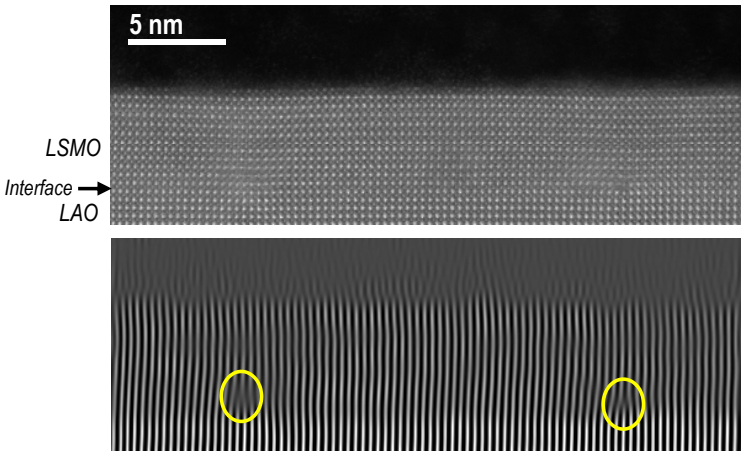

Fig. 3.12: *Z-contrast cross-section image (top-row) and its corresponding Fourier transform filtering image (bottom-row) of the LSMO ultra-thin film on LAO, which displays two misfit dislocations, ∼17 nm apart. Note the bending on the film surface produced by the dislocations at the interface. Courtesy of M. Roldán and J.Gázquez.*

nm) exhibit high crystallinity and no spurious phases within the matrix. They grow epitaxially with a cube-on-cube orientation. While on STO the LSMO films grow fully strained, they exhibit a completely relaxed structure when grown, after identical processing, onto LAO. We have also observed that LSMO terraces of different thickness coexist in the case of LSMO on LAO; these appear faceted in oblique $(101)_{\mathrm{LSMO}}$ and top $(001)_{\mathrm{LSMO}}$ crystal planes.

3.3 Macroscopic magnetic and transport properties of ultra-thin LSMO films on STO and LAO

We now move to the study of the magnetic and transport properties of the ultra-thin LSMO films described above. **Macroscopic magnetic measurements** were done using a superconducting quantum interference device (SQUID) at temperatures between 10 to 300 K and varying magnetic fields from 0 to 7 T. Both 0.03 M LSMO films grown on STO and on LAO (nominal average thickness t∼3.5±0.5 nm), annealed at 900°C for 1 h, showed ferromagnetic hysteresis in the whole temperature range up to room temperature (RT). Fig. 3.13 shows the resulting magnetization loops at 35 K. Both films exhibit very similar behavior, with a saturation magnetic moment m_S∼2×10^{-5} emu for LSMO/LAO and m_S∼1.8×10^{-5} emu for LSMO/STO. We can calculate the total volume of material from the estimated film thickness (t∼3.5 nm), which is assumed to be homogeneously distributed throughout the 5 ×5 mm^2 substrate surface. The corresponding saturation magnetization (for m_S∼2×10^{-5} emu) is then M_S=230±40 kA/m. The large error stems from the substantial uncertainty in the thickness value (±0.5 nm)[†]. Bulk LSMO (with 3.7μ_B per Mn atom) [64, 82] exhibits a magnetization of ∼590 kA/m, which is around 2.5 times higher than the value we measure in these ultra-thin films. In other words, only around t∼1.36 nm from the nominal average thickness t∼3.5 nm would contribute to the measured magnetic signal, if we should consider these 1.36 nm to contribute with a bulk-like 590 kA/m magnetization. The detailed inspection of the center of the hysteresis loops reveals some differences between the LSMO thin film grown on STO and on LAO: the latter exhibits higher remanence values (∼9×10^{-6} emu against ∼5×10^{-6} emu) and coercive fields ($\mu_0 H_c$ ∼140 Gauss against $\mu_0 H_c$ ∼115 Gauss). High coercive field values have been related to the presence of misfit dislocations at the film-substrate interface [22], which is in agreement with the dislocation-relaxed LSMO/LAO interface displayed by our solution-derived LSMO thin films.

The temperature dependence of the magnetic moment is given in Fig. 3.14. We have normalized both curves to the magnetic moment value at low temperature (T=16 K) to better compare them. We show, however, the high T range to avoid the paramagnetic slope present at low temperatures, which is most probably caused by impurities within the substrate[‡]. Note that the applied in-plane magnetic field was 100 Gauss for LSMO/LAO films and 500 Gauss for LSMO/STO films. The magnetic moment, deduced from each of the loops in Fig. 3.13, is m∼1.1×10^{-5} emu for these two field values, which constitutes a reasonable compromise between low applied magnetic field and a measurable magnetic signal. Both curves in Fig. 3.14 give similar Curie temperature T_C∼350 K, although LSMO on STO exhibits slightly lower magnetic moment values.

[†]More details on the uncertainty of the thickness are given in Part II of this chapter.
[‡]This issue will be further discussed in Part II of this chapter.

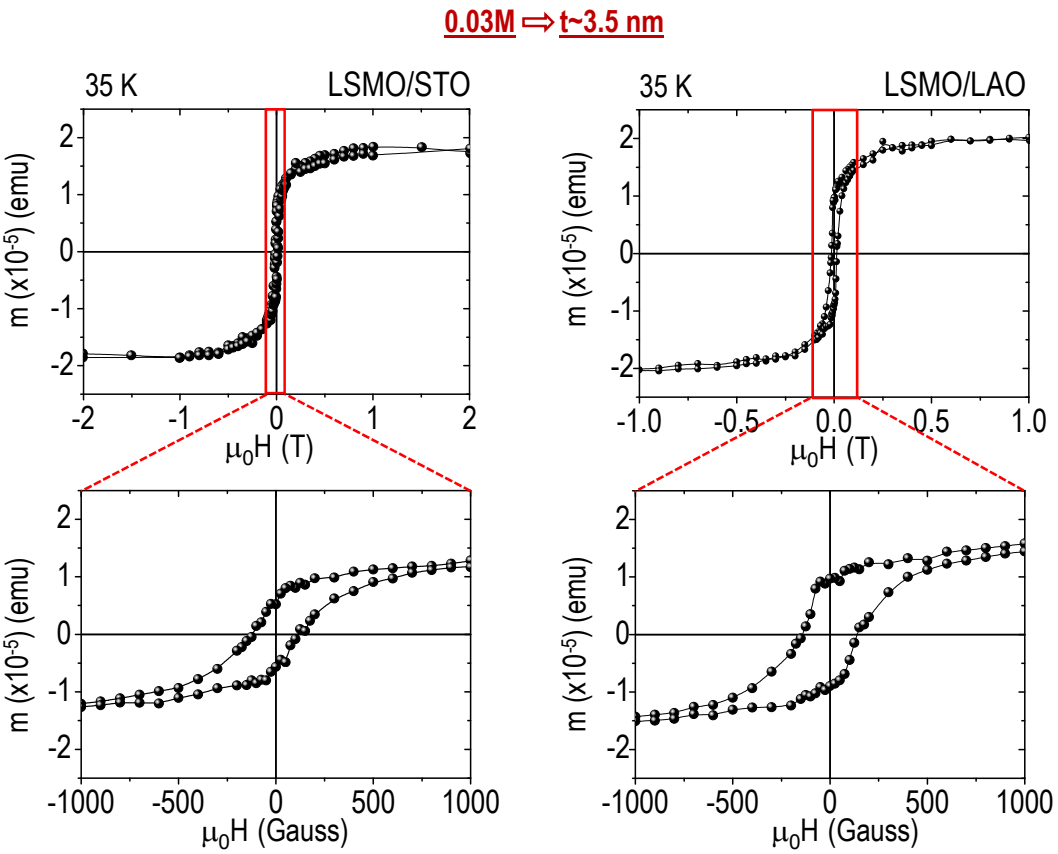

Fig. 3.13: *Magnetization loops (35 K) for 0.03 M LSMO thin films on STO and on LAO. Films display a saturation magnetization $m_S \sim 2\times10^{-5}$ emu, which corresponds to a volume magnetization M_S=230±40 kA/m, as deduced from the film thickness t=3.5±0.5 nm value.*

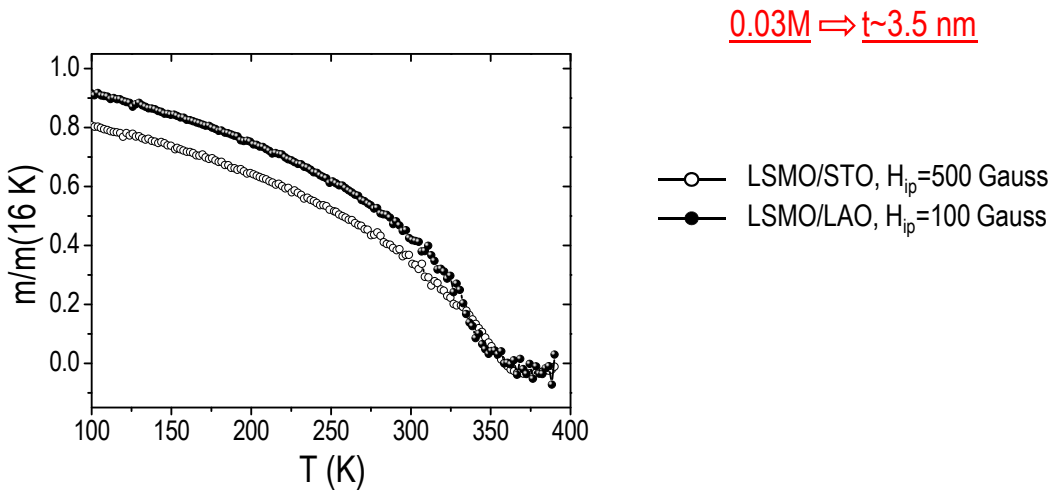

Fig. 3.14: *Normalized temperature dependent magnetic moment for LSMO ultra-thin films on STO (open dots) and LAO (full dots). The magnetic field (500 Oe and 100 Oe) was applied in-plane.*

There is large amount of work done concerning the study of the magnetotransport properties of LSMO thin films. Among these, many works have focused on the effect of epitaxial strain [22–25, 65, 162–165]. These works mainly examine the influence of strain by decreasing the film thickness and/or by growing the film onto different single crystal substrates. It is widely accepted that strain is accommodated by the tilt and/or distortion of the MnO_6 octahedra, hence influencing the Mn^{3+}-O^{2-}-Mn^{4+} bond angle and, in consequence, the hopping of the electrons responsible for the (ferro)magnetic and metallic behavior of manganites [17, 71]. The general trend observed is a decrease of T_C and of the magnetization with increasing strain and decreasing thickness. For instance, recently published data show that increasing tetragonal tensile distortions ($\epsilon\sim$-0.13% to $\epsilon\sim$2.5%) on the structure of PLD-derived $La_{0.67}Sr_{0.33}MnO_3$ thin films (thickness ∼10-40 nm) yield progressively lower magnetization and T_C values [22]. Previously, in their work of 2009, Adamo et al. gave evidence of how commensurately strained $La_{0.7}Sr_{0.3}MnO_3$ ∼22 nm films, grown by molecular beam epitaxy (MBE) over a large number of different oxide substrates, display T_C values in agreement with the theoretical predictions by Millis and co-workers [166]. According to their experimental results, fully commensurate compressively strained LSMO on LAO ($\epsilon\sim$-2.3%) shows a highly depressed T_C value around ∼290 K, while when grown on STO, i.e. under a tensile and substantially lower mismatch ($\epsilon\sim$+0.6%), T_C is ∼350 K, i.e. close to the bulk LSMO value.

Our STEM data for ultra-thin ($\lesssim$10 nm) LSMO films pointed at fully strained 0.03 M films (i.e. $t\sim$3.5 nm) on STO, while presenting a relaxed microstructure for the case of 0.03 M LSMO on LAO. The latter is certainly a remarkable result if we consider that for PLD films it is generally reported that full LSMO relaxation occurs at $t\sim$30 nm (see e.g. the work of Angeloni et al. [163]). Angeloni and co-workers also give evidence of fully strained films of $t\sim$8 nm thickness [163]. These results highlight that different growth techniques (i.e. CSD or PLD) have a different impact on the microstructure of the films. In line with the PLD films by Angeloni et al., Tsui and co-workers also report fully coherent $t\sim$25 nm thick LSMO films on LAO grown by sputtering [162]. On the other hand, regarding LSMO on STO, it is equally noteworthy that the solution-derived films here discussed (estimated average thickness ∼3.5±0.5 nm) show a clear ferromagnetic behavior, with T_C above 350 K. Although the theoretical model by Millis et al. (verified by Adamo et al. in ∼22 nm MBE LSMO films [65]), would not predict a substantial decrease in T_C, the actual majority of experimental results on ultra-thin LSMO films report highly suppressed T_C values. Fig. 3.15 reproduces the temperature dependent magnetization measurements on ultra-thin LSMO films on STO (PLD grown) of two state-of-the-art works in the literature. They both show the gradual suppression of T_C for decreasing film thickness values. At ∼8 u.c. (∼3.2 nm) either the fading of the ferromagnetic curve (Kim et al. [23]) or a clear reduction of T_C below 300 K (Huijben et al. [165]) are measured.

In addition to macroscopic magnetic properties, **electric transport properties** of the CSD-derived thin LSMO films were also investigated. The temperature dependence of resistivity, $\rho(T)$, was measured in the standard four-probe geometry, using a physical properties measurement system (PPMS, Quantum Design). Fig. 3.16 shows the ρ vs. T behavior of eight solution-derived LSMO films grown on LAO and STO from various precursor solution concentrations ranging from 0.03 M (nominal average thickness $t\sim$3.5 nm) to 0.1 M (nominal average thickness $t\sim$9 nm). The thinnest films (0.03 M), both on STO and on LAO, are insulating in the whole measurable T range, with LSMO/STO showing the most resistive behavior. This result suggests that the misfit dislocations present at the

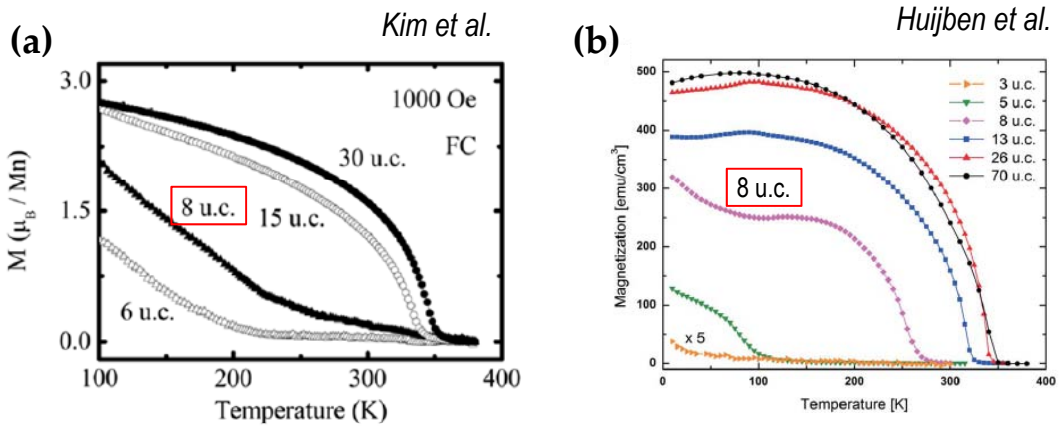

Fig. 3.15: *Temperature dependent magnetization measurements for PLD-grown LSMO ultra-thin films on STO. In-plane external magnetic fields of (a) 1000 Gauss [23] and (b) 100 Gauss [165] were used. At 8 u.c. (3.2 nm thick films) the FM behavior is highly depressed.*

LSMO/LAO interface, while increasing the H_C values, do not affect the transport properties of the film. Similar conclusions were reached for PLD-grown manganite films by Yang et al. [22]. Conversely, for films grown from $\geq$0.06 M concentrations a metal-insulator transition is measured, and the resistivity values of LSMO/STO systems appear below those obtained for LSMO/LAO films. Note also that the resistivity of the LSMO films decreases with increasing the concentration (i.e. with larger average film thicknesses). The estimated or nominal average thicknesses for 0.03 M, 0.06 M, 0.07 M, and 0.1 M are 3.5 nm, 5.5 nm, 6.3 nm, and 9 nm, respectively[§] Thus, summarizing, we observe that $\sim$5.5 nm sets a limit above which CSD-derived LSMO thin films show a metallic behavior for low temperature range, while for $\sim$3.5 nm and below we expect insulator behavior with no associated metal-insulator transition. In LSMO/STO multilayers grown by PLD, Kourkotis et al. recently measured metallic behavior in LSMO films as thin as $\sim$2 nm, provided that there is no disorder caused by chemical intermixing. With increasing disorder, however, identified by means of HAADF STEM, they observe that films with the same thickness become insulator [167]. The presence of a similar kind of disorder in our CSD-derived films cannot be ruled out at present. Indeed, further STEM measurements to identify oxygen vacancies, cationic intermixing...etc. are underway.

Concerning the values of the metal-insulator transition temperature, T_{MI}, Fig. 3.16 shows that for 0.06 M films ($\sim$5.5 nm) on LAO and STO T_{MI} is around 200-250 K, and that it takes higher temperature values for increasing concentrations. This tendency is further highlighted in Fig. 3.17, which shows explicitly the T_{MI} values for LSMO films grown from different solution concentrations. From Figs. 3.16 and 3.17, thus, it follows that T_{MI} varies with the thickness of the LSMO film and that it shows values below 350 K. Remarkably, all of these LSMO thin films, regardless of the solution concentration and of the substrate underneath (whether STO or LAO), showed a Curie temperature $T_C\sim$350 K. In other words, the metal-insulator transition and the ferromagnetic-paramagnetic transition appear decoupled in these thin manganite films.

Such striking result indicates that a mechanism different from the intrinsic physics re-

[§]The estimated thickness values are deduced from the LSMO on YSZ self-assembled nanoisland systems, as explained in section 3.4.1 of Part II of this chapter.

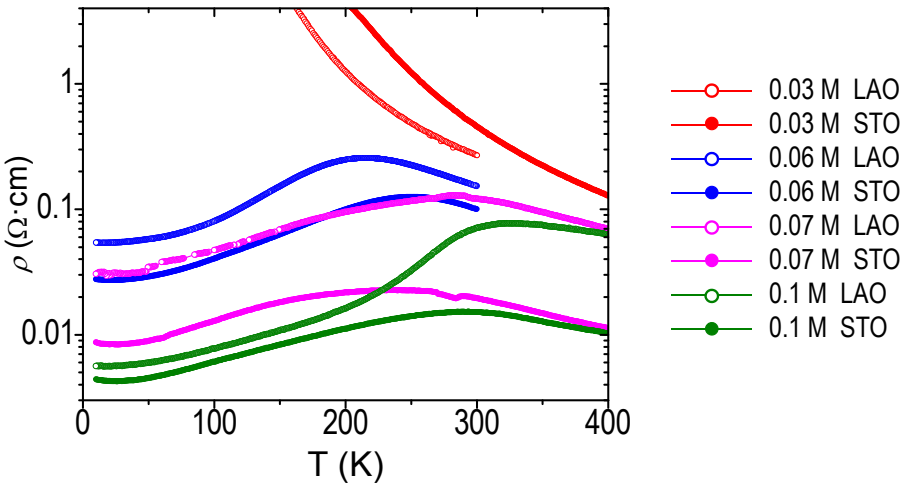

Fig. 3.16: *Temperature dependence of the resistivity for LSMO thin films grown on STO and LAO from precursor solution concentrations between 0.03 M and 0.1 M. Courtesy of A. Palau.*

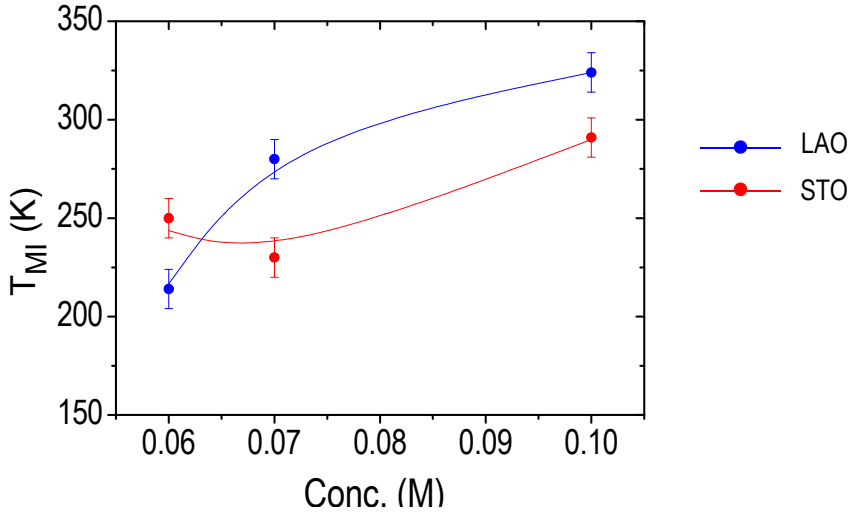

Fig. 3.17: *Metal-insulator transition temperatures for the different LSMO films grown on LAO and STO from different precursor solution concentrations. Courtesy of A. Palau.*

lated to manganites must be at play in our scenario of solution-derived LSMO films with nominal thickness below ∼10 nm. An Anderson type of localization in 2D films, where electrons are immobilized due to their multiple scattering with random defects in the potential of the solid [168], could, for instance, explain a metal to insulator transition in our very thin films, where the magnetic ordering is not necessarily affected. These interesting results, however, remain preliminary and thus future work is necessary to ascertain the physics behind them. Fig. 3.17 also reveals that T_{MI} increases with increasing solution concentration (e.g. for 0.1 M T_{MI} reaches room temperature). This suggests a good agreement with previous findings in our group concerning thicker (t∼25 nm) CSD-derived LSMO films (grown from 0.3 M solutions) [6, 140]: for such t values LSMO shows bulk-like properties with T_{MI}=T_C∼360 K, as expected in manganites. Although in our present case the decoupling of T_{MI} and T_C is clear for low concentration films, we must note that for very thin films below t∼10 nm the uncertainty in the value of t is large (recall, for instance, the thickness oscillations in LSMO/LAO films discussed previously). Thus, more statistics will be needed in order to ascribe exact T_{MI} values to different t values.

The magnetoresistance MR, defined as -$\Delta\rho$=[ρ(H=5)-ρ(H=0)]/ρ(H=0) (in $\%$), of two LSMO thin films (0.06 M, t∼5.5 nm) grown on LAO and STO is plotted in Fig. 3.18. The top panels show the temperature dependence of the resistivity (as already shown in Fig. 3.16) from where the MR curve is calculated (bottom panel). For zero applied field, these 0.06 M LSMO/LAO and LSMO/STO films exhibit maximum resistivity values of ρ∼2.56×$10^{-1}\Omega\cdot$cm and ρ∼1.26×$10^{-1}\Omega\cdot$cm, respectively. These numbers are around two orders of magnitude larger than the maximum resistivity value ρ∼1.4×$10^{-3}\Omega\cdot$cm obtained for CSD-derived 'standard' 0.3 M LSMO films [6]. By 'standard' we refer to the aforementioned LSMO 0.3 M films (t∼25 nm) that exhibit magnetotransport properties comparable to bulk LSMO [6]. Regarding magnetoresistance values, 0.06 M thin films show a maximum MR of ∼24$\%$ both on LAO and STO, which doubles the usual MR values registered for the aformentioned bulk-like LSMO thin films (MR∼11$\%$) [6]. Nevertheless, further work in our group has recently shown that nanocomposite LSMO films, where canonical LSMO coexists with inclusions from other phases, show enhanced values of magnetoresistance and broadening of the MR peaks. These are there argued to stem from chemical and/or structural disorder [169, 170]. Our current results in ultra-thin LSMO films bring new data to this discussion and are worth a much deeper investigation, beyond the scope of this thesis work.

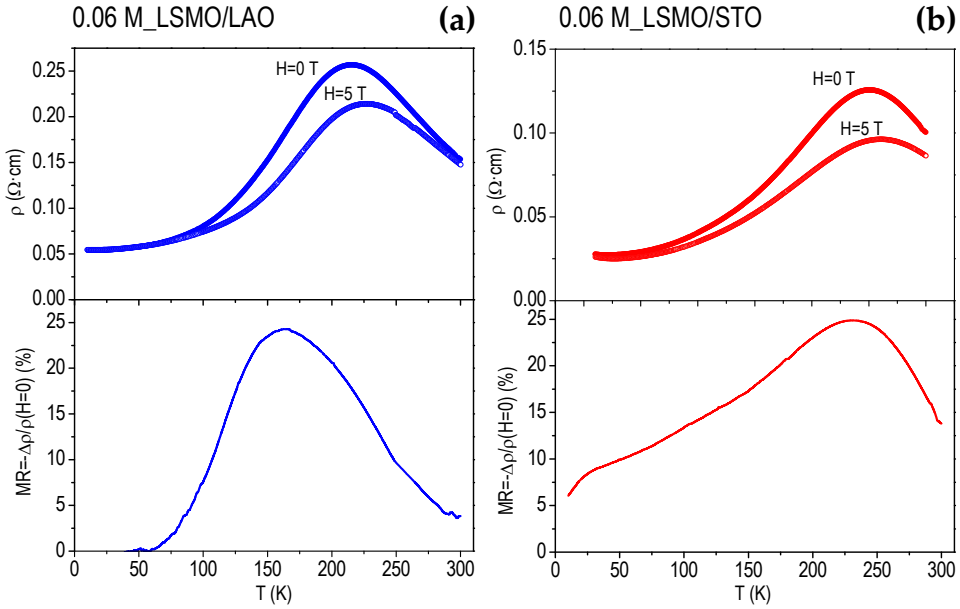

Fig. 3.18: *Magnetoresistance of chemically grown LSMO thin films (0.06 M, i.e. ∼5.5 nm average thickness) on (a) LAO and (b) STO substrates. Top panels show the resistivity dependence with temperature at zero applied field and at H=5 T, applied perpendicular to the film. Bottom panels show the magnetoresistance, MR, defined as -Δρ=[ρ(H=5)-ρ(H=0)]/ρ(H=0) (in %). Courtesy of A. Palau.*

Part II

$La_{0.7}Sr_{0.3}MnO_3$ on highly dissimilar substrates

We now turn to examine the main characteristics of CSD-grown LSMO onto non-perovskite substrates, namely YSZ and MgO. As described in Chapter 2, and also at the beginning of the present chapter, YSZ and MgO crystallize in a fluorite and a rocksalt structure, respectively. The nominal lattice mismatch with respect to LSMO ($a_{LSMO} = 3.873$ Å) is ϵ=(a_{YSZ}-$\sqrt{2}a_{LSMO}$)/($\sqrt{2}a_{LSMO}$)$\sim$-6% for YSZ ($a_{YSZ} = 5.14(7)$ Å), and ϵ=(a_{MgO}-a_{LSMO})/(a_{LSMO}) $\sim$+8.8% for MgO ($a_{MgO} = 4.21(4)$ Å). Note that the minimum mismatch occurs when the LSMO crystallographic axes are rotated by 45° with respect to those of YSZ. Still, the values are high, especially when compared to the mismatch in the LSMO/STO and LSMO/LAO systems. The difference in crystal structure and the high mismatches imply that the growth scenario is now very different from that for LSMO grown on STO and LAO. Indeed, the deposition and subsequent growth of ultradiluted LSMO solutions onto YSZ and MgO results in a homogeneous dispersion of self-assembled nanoislands, in striking contrast with the previously described ultra-thin LSMO films on STO and LAO. The following sections deal with the morphological, crystallographic, microstructural, and macroscopic magnetic study of these LSMO nanoislands.

3.4 LSMO on YSZ

3.4.1 Main features of solution-derived self-assembled LSMO nanoislands on YSZ

LSMO on (001)-YSZ was grown following the guidelines of the Chemical Solution Deposition (CSD) methodology explained in section 2.3 of Chapter 2, i.e. in an identical manner as in the case of the STO and LAO substrates. Unlike solution-derived LSMO thin films on STO and LAO, the study of which was already initiated within our group, the LSMO/YSZ system was unexplored at the time we undertook this work. Previous works in our group involving the growth of CeO_2 nanostructures proved helpful at the beginning, pointing at the use of very diluted solution concentrations (in the 0.005 M-0.05 M range), as a strategy for obtaining highly uniform self-assembled nanoisland dispersions [157, 171–173]. Nevertheless, the particularities of the LSMO/YSZ system required that the growth parameters be optimized in the present work, essentially starting from scratch. The present section is devoted to the description of solution-derived self-assembled LSMO nanoislands on YSZ, in terms of solution concentration, growth thermal treatments, and crystallographic structure.

Influence of precursor solution concentration

Our first goal was to analyze the role of the material quantity in the obtained heteroepitaxy and to determine the conditions for nanoisland growth. A straightforward way of influencing the amount of deposited material is to modify the precursor solution concentration, as we commented briefly for the case of LSMO on STO and LAO. For LSMO on YSZ we studied different solution concentrations in a diluted range, from 0.006 M to 0.09 M (in Mn), on the basis, aforementioned, that we sought nanoisland formation. The spin coating parameters (velocity, acceleration, time) were kept invariant for all the samples in the manuscript. Fig. 3.19 displays AFM topography images of representative samples grown from different starting solution concentrations. The growth temperature was 900°C for all samples and the annealing times varied from 1 h to 3 h.

Fig. 3.19 (a) shows a bimodal island distribution with a majority of small islands (thickness t∼8 nm, lateral size D∼50 nm) and a minority of larger ones (a total of six in the image, t∼25 nm, D∼200 nm). Note that the latter appear surrounded by a clean stepped substrate. This strongly suggests an Ostwald ripening type of coalescence at this specific evolution stage, in which large islands grow at expenses of smaller islands, which shrink and finally disappear, their atoms having diffused towards the large structure [174].

More uniform nanoisland dispersions, with no agglomerated nanostructures, are found for the 0.015 M-0.06 M concentration range. Figs. 3.19 (b), (c) and (d) show well-defined individual nanoislands, with increasing lateral size for increasing concentration, and a reasonably narrow size distribution, especially in the 0.015 M and 0.03 M case. Increasing the solution concentration to 0.09 M, the z scale drops to 20 nm and we no longer have nanoislands. Instead, we obtain a continuous granular film with RMS roughness of around 2 nm. This was further confirmed by testing for LSMO conductance with a standard two-probe multimeter, which gave a value in the order of hundreds of kOhms. Hence, the film not only is continuous, but also conducting, as expected for LSMO.

From these results we deduce that concentration ranges between 0.015 M and 0.06 M are required to obtain a self-assembled nanoisland system, i.e. a system in which the spontaneous gathering of atoms and molecules under the specific growth conditions leads to nanoislands with a narrow size distribution. After nucleation has taken place, the driving force for the particular nanoisland arrangement is the energy minimization, which, in our oxide heteroepitaxy case, involves surface and interface energies, and the elastic strain energy due to the lattice mismatch between LSMO and YSZ. In other words, we have a strain-induced nanoisland self-assembly in which the island interaction is substrate-mediated. This is the reason why the dispersion we see in the $5\ \mu m \times 5\ \mu m$ images extends uniformly all over the 5 mm $\times$ 5 mm substrate. We checked this by performing large AFM scans ($50\ \mu m \times 50\ \mu m$) at multiple different substrate spots.

Through the volume analysis of a large number of AFM images we are able to roughly deduce what amount of material we have in each sample. The equivalent thickness t_{eq} parameter represents the thickness of a hypothetical film made from uniformly distributing the totality of the island volume throughout the 5 mm $\times$ 5 mm substrate surface. The results of such measurements for samples grown from different precursor concentrations are plotted in Fig. 3.20. Data corresponding to 0.09 M, 0.2 M, and 0.5 M are from a different work, reporting the AFM profilometry measurements of acid-attacked LSMO films grown on LAO and STO, also by CSD [140]. The amount of material, represented by t_{eq}, increases linearly with increasing concentration. Equivalent thickness data t_{eq} and their associated errors, as well as the number of samples averaged, are listed in Tab. 3.1. It is worth noting that the estimated amount of thickness for the more diluted case, 0.006 M, is in the order of the monolayer. Such small amount of material implies that the first formed nuclei are likely to be inhomogeneously distributed, which may explain the subsequent non-uniform nanoisland distribution, with agglomerations, observed in Fig. 3.19 (a).

Influence of annealing time

In a closed system as the one we have, where the whole amount of material is present from the initial deposition stage, it is expected that kinetic events such as atomic diffusion should lead the system towards its thermodynamic equilibrium. By increasing the annealing time

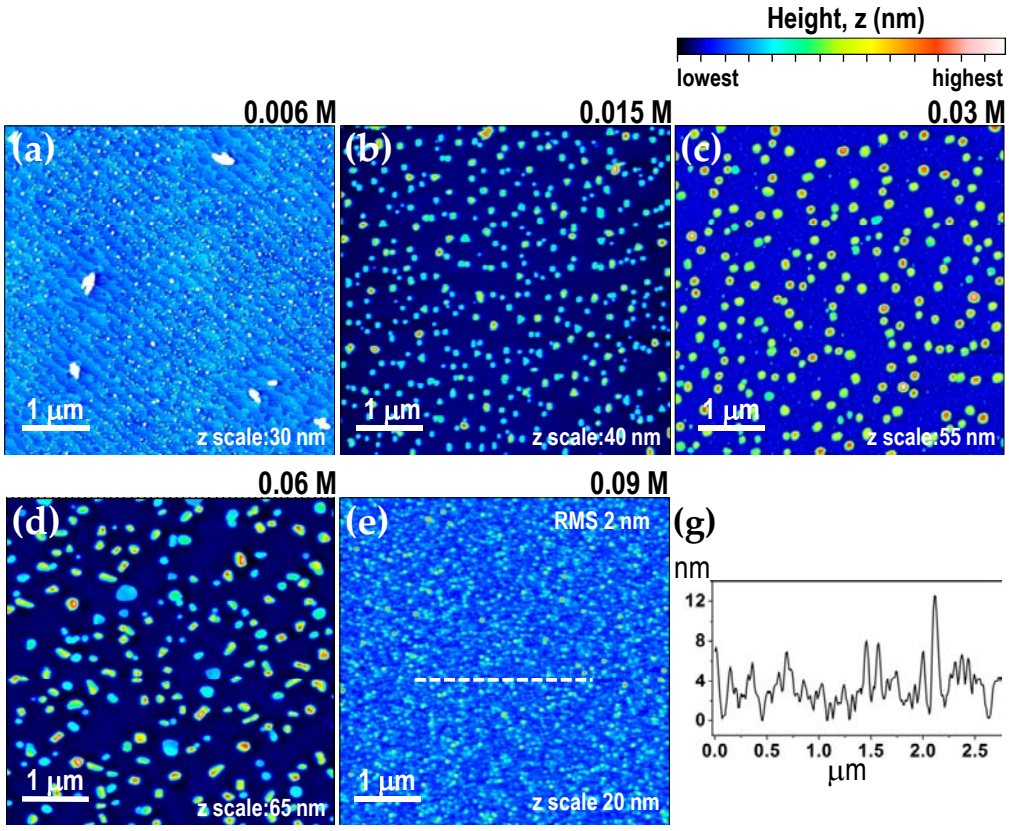

Fig. 3.19: *5µm × 5µm AFM topography images of the nanoscale LSMO systems resulting from deposition and growth of different solution concentrations. Growth T was 900°C and annealing times varied between 1 h to 3 h. (a) At 0.006 M, the little amount of material may lead to nucleation inhomogeneities, reflected in the bimodal nanoisland distribution. (b),(c)&(d) For concentrations in the 0.015 M to 0.06 M range we observe a homogeneous dispersion of well-defined nanometric islands, with narrower size distribution. (e) For 0.09 M, islands no longer develop and the resulting system is a continuous film with a ∼2 nm RMS roughness. (g) Line scan corresponding to the dashed line in (e), showing the roughness profile of the film.*

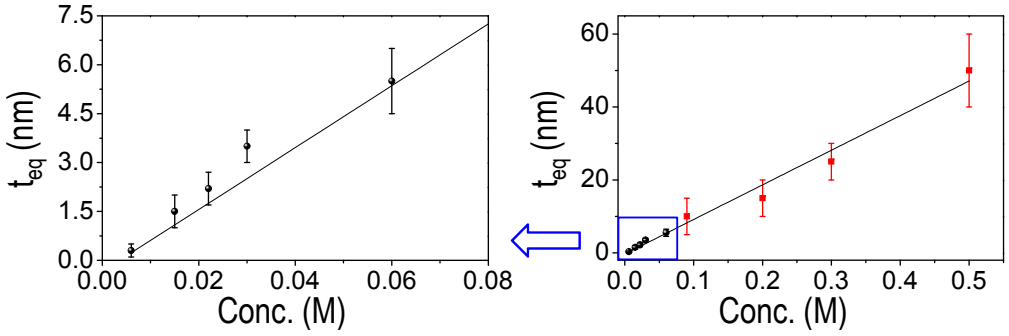

Fig. 3.20: *LSMO precursor solution concentration plotted against the equivalent LSMO layer thickness. Black dots are all from measurements on LSMO/YSZ systems of the present work.* t_{eq} *values are deduced from AFM volume estimations. Red squares at 0.09 M, 0.2 M, 0.3 M, and 0.5 M are from LSMO layers grown by CSD on STO and LAO substrates, obtained from measuring the step of a chemically attacked layer [140].*

Conc. (M)	t_{eq} (nm)	Δt_{eq} (nm)	No.Samples
0 .006	0.3	0.2	2
0 .015	1.5	0.5	5
0 .022	2.2	0.5	3
0 .03	3.5	0.5	11
0 .06	5.5	1	2
*0.09	10	5	_
*0.2	15	5	_
*0.3	25	5	_
*0.5	50	10	_

Tab. 3.1: *LSMO precursor solution concentration with its corresponding LSMO equivalent layer thickness.*Data taken from the thesis work of C. Moreno [140].*

and stopping regularly to analyze the system, we can follow its spontaneous evolution, study the coarsening processes that take place, or evaluate the system mobility.

Fig. 3.21 reproduces the result of the growth of a 0.03 M precursor solution at 900°C for 2 h, 3 h and 12 h. At first sight, the three images of Fig. 3.21 (a) look very much alike. A dispersion of well-defined nanoislands homogeneously covers the $5\ \mu m \times 5\ \mu m$ AFM topography images, with an area coverage below the 20%. The magnified views in Fig. 3.21 (b) reveal a tendency towards substrate surface cleaning for increasing annealing times: small particles will eventually diffuse and join the larger well-defined nanoislands. In addition to the square-shape islands of the 2 h sample, the 3 h sample exhibits some triangular nanostructures, although these were found not to be characteristic of the 3 h treatment (we sometimes observed them after shorter treatments). We will see later in the chapter that they exhibit a different crystal orientation. Additionally, both in the 3 h and 12 h treated samples, a few islands show polygonal shapes different from squares or triangles. Some of them appear highlighted with white squares in Fig. 3.21 (a). It is well known that, upon annealing, nanostructure facets tend to vary due to the adsorption of adatoms. These adatoms can come from material resting on the surface. This appears to be the case in here, given the progressive cleaning of the substrate surface that accompanies nanoisland evolution towards polygonal shapes.

Ostwald ripening processes refer precisely to the above-mentioned dissolution of small islands into larger islands [174]. Other coarsening processes may coexist together with Ostwald ripening. An example is static coalescence, in which two nearby islands grow towards their equilibrium shape, meet, and subsequently merge into a larger island [157, 175]. Fig. 3.22 (a) shows a zoomed image of what at first sight resembles a uniform hexagonal island. The 3D topography and amplitude images below reveal, however, that such large island is formed by two colliding triangles. Some of the large polygonal islands inside white squares in Fig. 3.21 (a) could be the result of such processes. Fig. 3.22 (b) displays two pairs of merging islands, taken from the 12 h sample of Fig. 3.21 (a).

Let's now examine the evolution of the system from a more general point of view, i.e. considering the statistical thickness t and lateral size D data for a collection of nanoislands. The histograms in Fig. 3.23 evidence that heat-treated samples at 900°C for 2 h and 12 h show very similar values: in the 2 h sample we have mean thickness and lateral size values around $t\sim$30 nm and $D\sim$120 nm, respectively. At 12 h, the system evolves to island

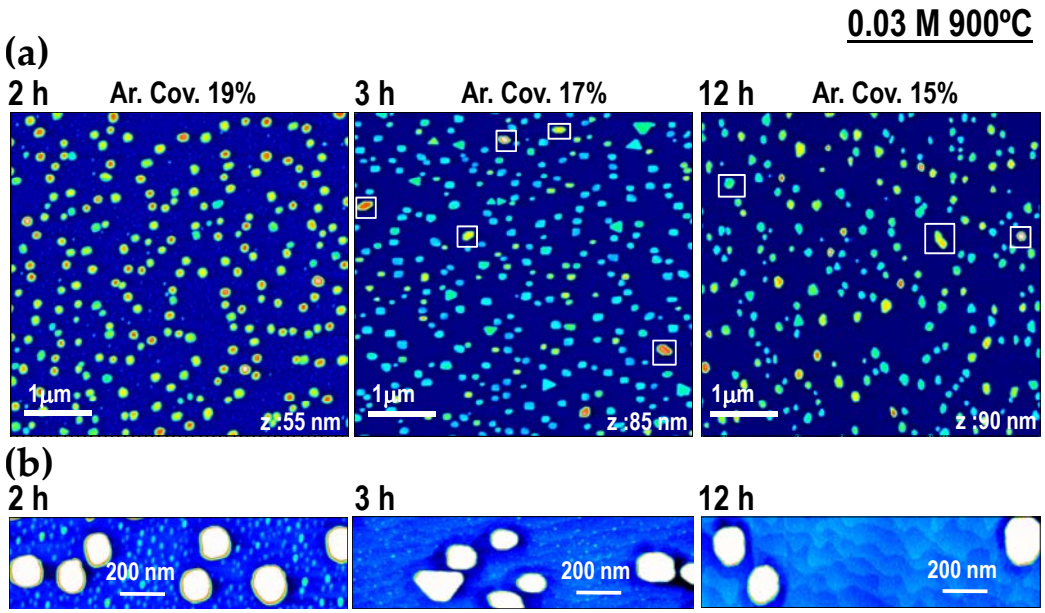

Fig. 3.21: *(a) 5µm × 5µm AFM topography images of self-assembled LSMO nanoislands grown at 900°C on YSZ for 2 h, 3 h, and 12 h. 0.03 M precursor solutions were used in each case. The majority of islands show square shape. Triangular islands are also observed, as well as a few polygonal structures, marked within white squares. (b) Zoomed-in images of (a) showing the progressive cleaning of the substrate upon sample annealing.*

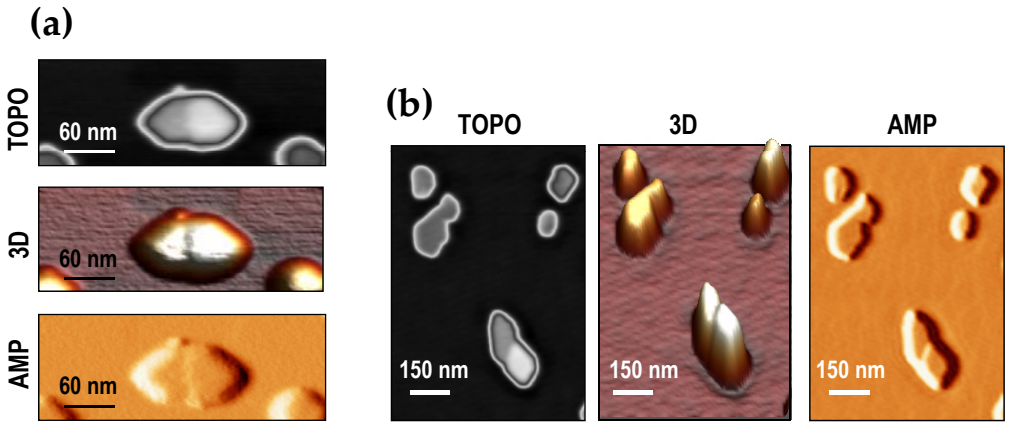

Fig. 3.22: *(a)&(b) 2D topography, 3D, and amplitude images of merging LSMO nanoislands. The presence of what originally were two islands is best seen in the 3D and amplitude images. It is expected that, let the system to evolve, atoms will diffuse and finally yield a fully reconstructed single structure.*

thicknesses of around t∼40 nm and lateral sizes D∼130 nm. This is also accompanied by a slight decrease in area coverage, as expected, since the same amount of material (corresponding to a 0.03 M solution) was deposited. Note that the lateral size values of islands are always much larger than their thickness values, with mean D/t aspect ratios of around 4. This is a general trend of LSMO nanoislands, as we will confirm throughout the thesis. Interestingly, it appears that at 2 h the system was already near its thermodynamic equilibrium, showing small size variations upon subsequent annealings, even after several hours. In other words, it seems that the kinetic events which push the system towards its equilibrium have already taken place by the time we looked at the system after 2 h of annealing. This indicates a high atomic mobility of LSMO on YSZ at 900°C. It is worth noting that the heating ramp used is very slow ($3°C \cdot min^{-1}$), so the system may be already near its equilibrium at the moment of reaching the annealing plateau.

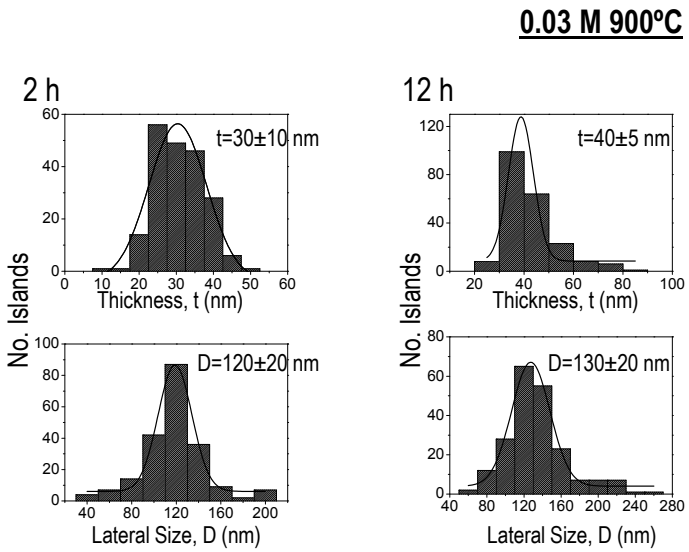

Fig. 3.23: *Thickness* t *and Lateral size* D *histograms extracted from 0.03 M 900°C heat-treated samples at 2 h and 12 h.* D *values were deduced from measuring the whole perimeter of each island and then assuming a perfect square. No triangles were taken in the measurement.* t *shows values in the 20-40 nm range, while* D *values are in the hundreds of nm range. The error is the standard deviation of the Gaussian fit.*

In summary, the above analysis illustrates the evolution of the self-assembled nanoisland system. This is showcased by small variations in the size range (t∼30 nm D∼120 nm) of the LSMO nanoislands on YSZ, when heat-treated at 900°C. A slight increase of the island volume in times as long as 12 h is accompanied by the substrate surface cleaning. In addition to Ostwald ripening processes (small islands coalescing into larger islands) other coalescence mechanisms have been identified, such as the static coalescence of already formed faceted islands. Overall, the slow evolution shown by the system at this temperature, along with the fact that nanoislands are well formed and faceted already in the 2 h annealing stage, suggest that, by that time, the system has already undergone the main kinetic events leading to its equilibrium state. A study of what happens at higher temperatures, where a new equilibrium might take place, results thus of great interest. Prior to this we will investigate the crystal structure of nanoislands and their epitaxial relationship with respect to (001)-YSZ.

LSMO nanoisland crystallographic orientation

$(001)_{\mathrm{LSMO}}$-ORIENTED NANOISLANDS

For the sake of simplicity, in the previous sections we have referred to the self-assembled nanoislands as LSMO nanoislands. However, XRD analysis is necessary to be able to determine whether the crystal structure of our islands corresponds indeed to LSMO. We also expect to ascertain the epitaxial growth imposed by the YSZ single crystal substrate underneath. Fig. 3.24 displays a θ-2θ scan corresponding to a system of self-assembled nanoislands grown from a 0.03 M solution on YSZ, processed at 900°C for 1 h. Along with the (001) intense substrate peaks we clearly identify the $(002)_{\mathrm{LSMO}}$ reflection peak at 2θ=46.9°. Weakly emerging from the background noise, the $(001)_{\mathrm{LSMO}}$ peak, expected less intense than the $(002)_{\mathrm{LSMO}}$, can also be observed at 2θ=23°. We have indexed the LSMO reflections in terms of the pseudocubic notation, as we already did for LSMO on STO and LAO ($a_{LSMO} = 3.873$ Å). This result already indicates epitaxial growth of the nanoislands, with their (001) planes parallel to the substrate (001) planes. The rocking curve in Fig. 3.24 (b) shows the out-of-plane texture of the nanoisland ensemble, with a large full width at half maximum (FWHM) value of$\sim$3.3°. If it were a continuous film, such broad peak would indicate a rather poor epitaxy. Nevertheless, for nanometric structures, a general peak broadening is not unexpected. Indeed, the nanoisland out-of-plane orientation is highly sensitive to the substrate structure such as surface roughness or the presence of steps and kinks on which islands nucleate and grow. This may induce the formation of tilted domains and other misorientations [176]. Also, it is well known that the accommodation of misfit strains through dislocations at the interfaces can trigger nanoisland rotations. In summary, a large number of slightly misoriented islands appears consistent with the observed rocking curve.

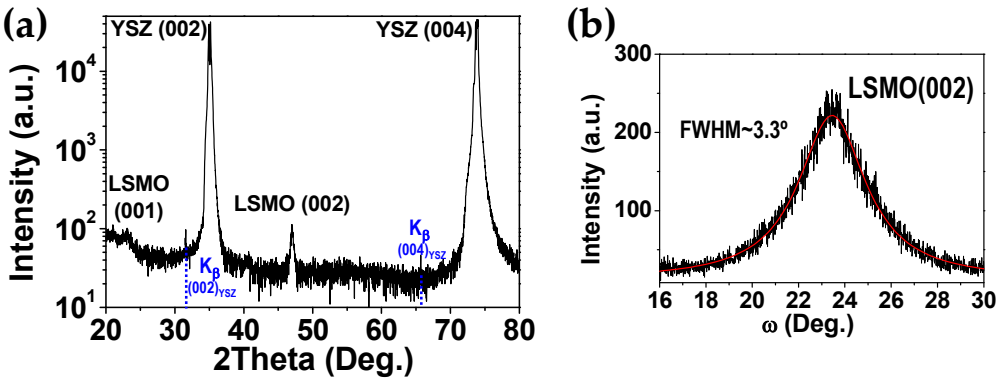

Fig. 3.24: *(a) θ-2θ scan showing the out-of plane epitaxial growth of a self-assembled LSMO nanoisland system grown onto YSZ from a 0.03 M solution at 900°C for 1 h. (b) Rocking-curve of the $(002)_{LSMO}$ reflection exhibiting a FWHM of 3.3°.*

In order to study the in-plane epitaxial relationship between the LSMO nanoislands and the YSZ substrate we conducted phi-scan measurements with a XRD diffractometer equipped with a 2D detector (XRD^2 measurements, see Appendix A). Integration in 2θ of the collected 2θ-χ frames (with $\Delta\phi = 2°$, 180 frames in total), leads to the pole figures shown in Fig. 3.25. Both the $(011)_{\mathrm{LSMO}}$ and the $(022)_{\mathrm{YSZ}}$ poles appear at χ=45° [consistent with the out-of-plane (001) orientation], but are rotated in-plane ϕ=45° with respect to each other, indicating that nanoislands adopt the epitaxial relationship $(001)_{\mathrm{LSMO}}[110]||(001)_{\mathrm{YSZ}}[010]$.

The interface arrangement $[110]_{\mathrm{LSMO}}||[010]_{\mathrm{YSZ}}$ of our heteroepitaxy would therefore correspond to a nominal misfit $\epsilon\sim$-6% between the [110] direction of LSMO ($\sqrt{2}\mathrm{a}_{\mathrm{LSMO}}$= 5.477 Å) and the [100] direction of YSZ ($\mathrm{a}_{\mathrm{YSZ}}$=5.14(7) Å). This significant difference in lattice mismatch at first sight suggests a highly strained heteroepitaxy. This, however, would entail an unfavourably large building up of strain energy. Thus, it is natural to expect the relaxation of the nanostructure via misfit dislocation formation. As a matter of fact, although very roughly estimated, the LSMO lattice parameter deduced from the θ-2θ scans corresponds to the bulk LSMO value, already indicating a relaxed structure.

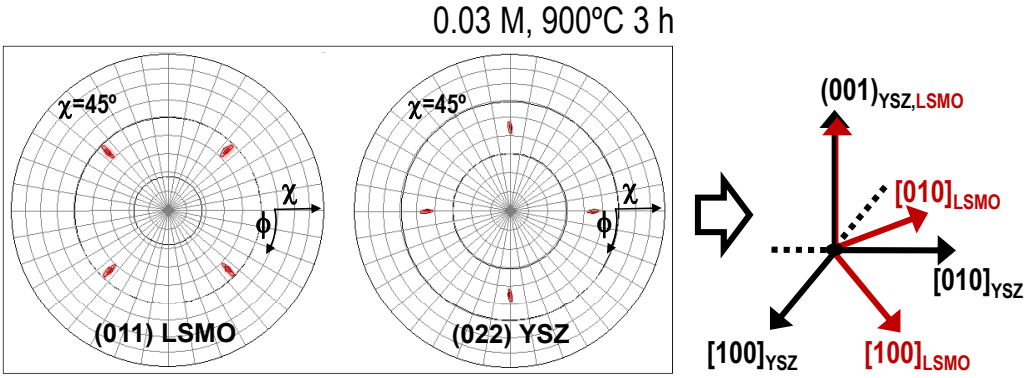

Fig. 3.25: *Pole figures of the $(011)_{LSMO}$ and $(022)_{YSZ}$ reflections indicating $(001)_{LSMO}$[110]//$(001)_{YSZ}$[010] oriented nanoislands. The epitaxial relationship is sketched on the right panel. The sample was 0.03 M, heat-treated at 900°C for 3 h.*

Further evidence of the nanoisland strain state and of the epitaxial arrangement was obtained using high resolution transmission electron microscopy (HRTEM) and electron diffraction (ED) measurements. Fig. 3.26 (a) shows an ED pattern of a selected area, containing both the YSZ substrate and a single LSMO nanoisland. The epitaxial relationship of the individual island with respect to the YSZ substrate agrees with the $(001)_{\mathrm{LSMO}}$[110]|| $(001)_{\mathrm{YSZ}}$[010] epitaxy, obtained from XRD measurements, for the whole nanoisland ensemble. Note also that the sublattices of the substrate and the nanoisland can be easily distinguished with the naked eye. Moreover, a measure of the lattice spacing separation is consistent with a complete relaxation of the lattice parameters for LSMO. A HRTEM image of an interfacial region is shown in Fig. 3.26 (b). Fourier filtering analyses reveal that the strain contrast observed at the interface corresponds to dislocations with Burgers vector $\vec{b}$=($\mathrm{a}_{\mathrm{YSZ}}$/2)[100] (evidenced with arrows in the image), with the extra half plane residing in the substrate in order to accommodate the compressive lattice mismatch in the island. The average distance between dislocations measured in the image, $\sim$4.0 nm, coincides with the theoretical value $|\vec{b}|/\epsilon$ for a complete misfit relaxation. Our results thus confirm that the LSMO islands on YSZ are free of misfit strains. They also demonstrate the good crystalline quality within an individual island.

$(111)_{\mathrm{LSMO}}$-ORIENTED NANOISLANDS

Despite constituting the vast majority of the nanoislands, the out-of-plane (001)-oriented nanostructures are not the only present in our LSMO/YSZ system. The triangular morphology observed in a number of samples, in fact, points at a different out-of-plane orientation. This was indeed proved in a sample exhibiting a notable amount of triangular features (around the 25% of the total island population). Fig. 3.27 shows the AFM topography im-

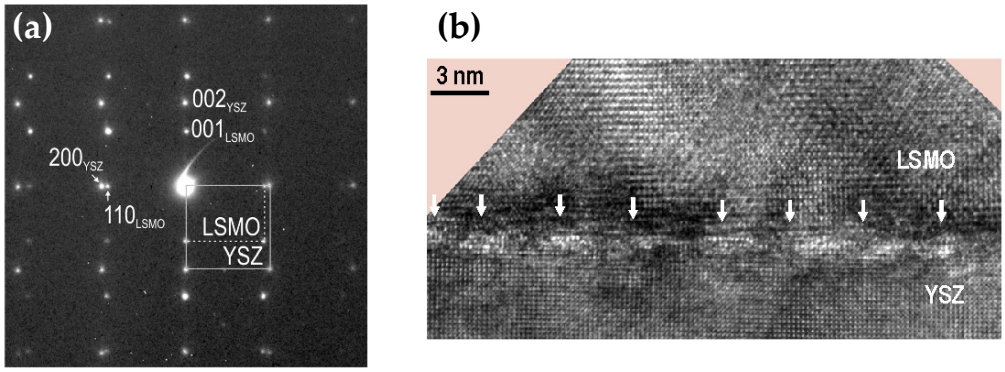

Fig. 3.26: *(a) ED pattern taken across the island-substrate interface. It shows the epitaxial relationship $(001)_{LSMO}[110]//(001)_{YSZ}[010]$. The LSMO and YSZ lattices are marked by dashed and continuous lines, respectively. (b) Cross-sectional HRTEM image of a (001)-oriented LSMO nanoisland, where the arrows indicate regularly spaced misfit dislocations at the island/substrate interface. The LSMO island and the YSZ substrate are viewed along the [110] and [010] zone axes, respectively. Courtesy of P. Abellán.*

age of the sample featuring both square and triangular nanoislands. The pole figure of the $(011)_{\mathrm{LSMO}}$ reflection, with poles falling at χ=35.3°, indicates the presence of the $(111)_{\mathrm{LSMO}}$ out-of-plane orientation, which coexists with the previously described $(001)_{\mathrm{LSMO}}$ population. The multiplicity of a reflection displaying the (111) out-of-plane orientation is 3. The fact that we observe 12 poles in total accounts for the four different in-plane orientations that the triangle can choose on the substrate. The presence of four populations is proved through AFM images; we have highlighted an example of each in Fig. 3.27 (a). The poles encircled in Fig. 3.27 (b) correspond to one of the four populations, separated 120° in ϕ.

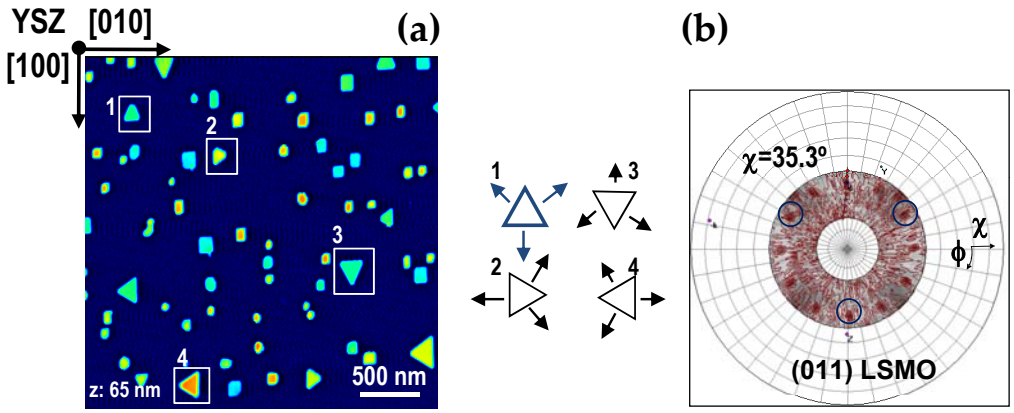

Fig. 3.27: *(a) $3\mu m \times 3\mu m$ AFM topography image of a 0.03 M LSMO nanostructured sample, processed at 900°C for 1 h. In addition to the square shape islands we may observe a large number of triangular islands. Examples of the four possible in-plane orientations are marked within white squares. (b) Up to 12 poles, at χ=35.3°, are detected in the $(011)_{LSMO}$ reflection pole figure due to the four possible in-plane orientations; each of them yields three 120° separated poles.*

The epitaxial relationship of the $(111)_{\mathrm{LSMO}}$ oriented islands is further supported by TEM and ED analysis. Fig. 3.28 (a) shows the ED pattern for one $(111)_{\mathrm{LSMO}}$-oriented nanoisland displaying the epitaxial arrangement $(111)_{\mathrm{LSMO}}$[11-2]||$(001)_{\mathrm{YSZ}}$[100]. Since there

are four possible ways for the island to orient on the substrate, the in-plane epitaxial relationship can also be $[1-10]_{\mathrm{LSMO}}||[100]_{\mathrm{YSZ}}$ for the 90° rotated triangle, and $[-1-12]_{\mathrm{LSMO}}||[100]_{\mathrm{YSZ}}$ and $[-110]_{\mathrm{LSMO}}||[100]_{\mathrm{YSZ}}$ for the corresponding mirror images. The four possible arrangements are sketched in Fig. 3.28 (b). It is also important to note that this epitaxial configuration imposes two different nominal misfit values on the in-plane matching directions. While the misfit for $[1-10]_{\mathrm{LSMO}}||<100>_{\mathrm{YSZ}}$ is $\epsilon\sim$-6% (the same as for the in-plane directions of the $(001)_{\mathrm{LSMO}}$-oriented square pyramids), the nominal misfit value for $[-1-12]_{\mathrm{LSMO}}||<100>_{\mathrm{YSZ}}$ is as large as $\epsilon\sim$-19%. These values are indicated in the sketch of Fig. 3.28 (b). Nonetheless, similarly to the case of the $(001)_{\mathrm{LSMO}}$-oriented nanoislands, the ED patterns indicate that these large strains are also relaxed in the case of $(111)_{\mathrm{LSMO}}$-oriented triangles.

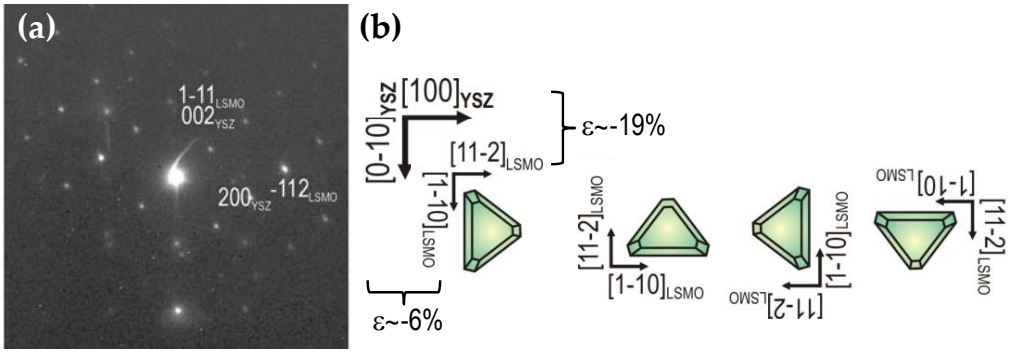

Fig. 3.28: *(a) ED measurement of a $(111)_{LSMO}$-oriented triangular nanoisland, zone axis $[110]_{LSMO}$, exhibiting a $(111)_{\mathrm{LSMO}}$[11-2]$||(001)_{\mathrm{YSZ}}$[100] epitaxial relationship. (b) Sketched diagram of the four possible in-plane epitaxial arrangements of the $(111)_{LSMO}$ nanoislands. The nominal misfit values between nanoisland and substrate are ∼-6% and ∼-19% for the two orthogonal directions.*

In summary, we have found that the solution-derived self-assembled structures that we grow are LSMO nanoislands of high crystalline quality and relaxed strain state. The vast majority of them exhibit a $(001)_{\mathrm{LSMO}}$ out-of-plane orientation with respect to the (001)-YSZ substrate and are oriented at 45° with respect to the plane. We have also identified a minority population of $(111)_{\mathrm{LSMO}}$-oriented nanoislands, which exhibit triangular morphologies. The analysis done here concerns nanostructured samples grown at 900°C. The next section deals with the system characteristics at higher annealing temperatures.

Influence of high annealing temperatures

In order to examine the effect of higher temperatures in the self-assembled LSMO nanoisland system we performed a series of experiments at 1000°C and 1300°C. Both LSMO and YSZ are reported to be thermodynamically stable at these temperatures and at the oxygen pressures that we use ($p_{O_2}\sim$1 bar) [177–180]. Fig. 3.29 shows 5 μm × 5 μm AFM topography images of two LSMO systems, both grown from 0.03 M solutions, and subject to $T\geq$1000°C annealings. The nanoisland *t* and *D* distributions are also shown. The first thing to note with respect to the 900°C examples of Fig. 3.21 is a clear decrease in area coverage together with a notable increase in both nanoisland *t* and *D*. At 1000°C islands easily attain lateral sizes around ∼180 nm and thicknesses in the ∼60 nm range. It appears that the atomic diffusivity at 1000°C is high enough to promote coarsening, i.e. the growth of large

islands at the expense of smaller islands. This yields a system in which 40 nm-thick and 100 nm-wide islands coexist with 100 nm-thick and 300 nm-wide structures. By increasing the temperature to 1300°C, islands attain even higher thickness and lateral sizes, i.e. $t\sim$80 nm and $D\sim$220 nm [see Fig. 3.29 (d)]. The inset in Fig. 3.29 (c) shows a thresholded image, where the color scale has been restricted (nanoislands appear saturated) to better see the substrate step morphology. We see that the high diffusivity at such high temperatures promotes the evolution of the terraces into curved and rounded-shape steps. These structures feature heights larger than one unit cell (what is known as *step bunching*).

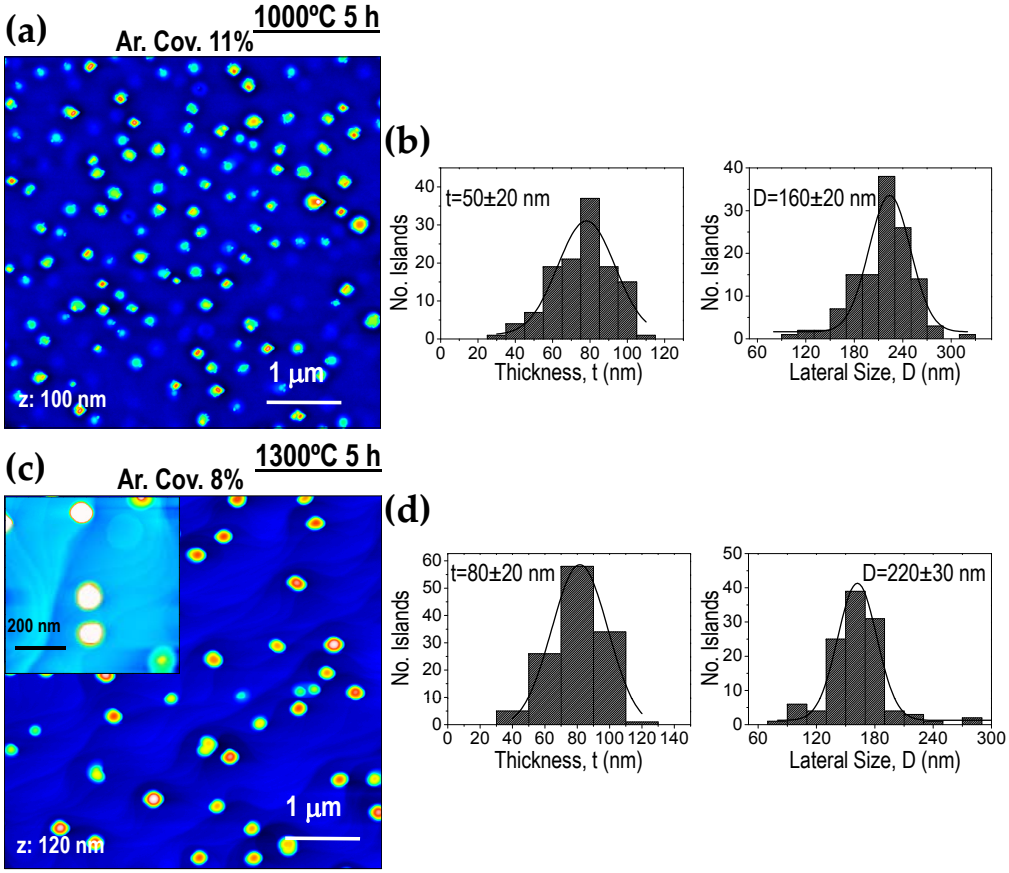

Fig. 3.29: *5μm × 5μm AFM topography images featuring self-assembled nanoislands after heat-treatments at (a) 1000°C for 5 h, and (c) 1300°C for 5 h. The solution concentration was 0.03 M. (b)&(d) Nanoisland thickness and lateral size histograms show larger and higher nanoislands with increasing annealing T.*

In order to examine the crystal structure of the systems annealed at high temperature we performed XRD measurements. Fig. 3.30 shows the θ-2θ analysis of two self-assembled nanoisland systems on YSZ (0.03 M), annealed at (a) 1000°C for 24 h, or (b) 1300°C for 5 h. The sample treated at 1000°C for 24 h exhibits an intense and narrow $(002)_{\mathrm{LSMO}}$ peak in addition to a small yet clear $(001)_{\mathrm{LSMO}}$ peak, which was hardly detectable in the 900°C 1 h sample of Fig. 3.24 (a). Such increase in the intensity suggests an improvement in the crystallinity of the LSMO phase at high temperatures. In contrast, the intensity of the $(002)_{\mathrm{LSMO}}$ reflection decreases substantially in the θ-2θ scan of the 1300°C sample, while two other peaks, marked with red arrows, appear. As a matter of fact, although less evi-

dent, there are also traces of these new peaks in the θ-2θ scan of image (a), also indicated with red arrows. No evidence for such peaks was found in 900°C treated samples (see e.g. Fig. 3.24).

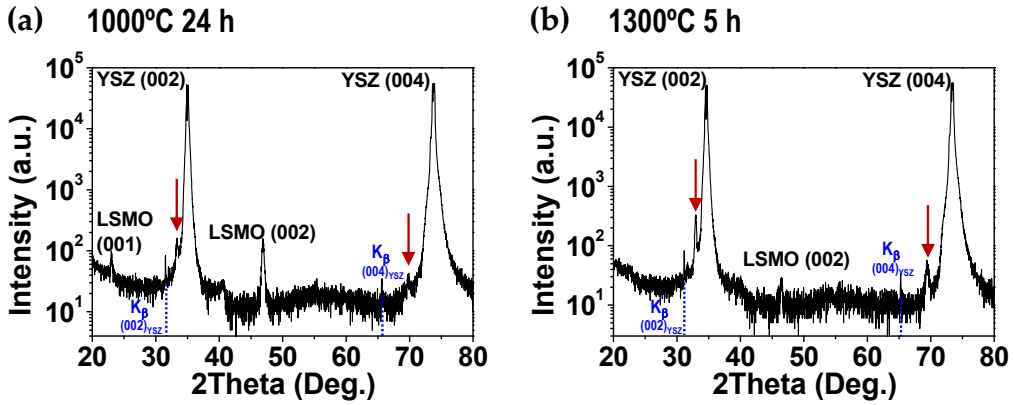

Fig. 3.30: *θ-2θ scans of self-assembled LSMO nanoislands on YSZ, heat treated at (a) 1000°C 24 h, and (b) 1300°C 5 h. Note how the LSMO reflections are clear in (a) and, in contrast, barely noticeable in (b). Two new peaks (marked with red arrows), particularly obvious in (b), also develop.*

Fig. 3.31 shows the zoomed-in θ-2θ scans from Fig. 3.30 (b), to better appreciate the two new peaks. Interestingly, the corresponding 2θ values, i.e. 2θ=33.2° and 2θ=69.7°, accurately match the (004) and (008) reflections of the cubic pyrocholore $La_2Zr_2O_7$ (read *Lanthanum zirconate*, LZO) compound [181–183]. Moreover, the I(004)/I(008) ratio of our measurement, around 5.6, is in fair agreement with the reported ratios found in the literature [I(004)/I(008)=5.34 [181], I(004)/I(008)=4.8 [182]]. The insets in Fig. 3.31 display the rocking curves of the $(004)_{\mathrm{LZO}}$ and $(008)_{\mathrm{LZO}}$ reflections, with FWHM values of ∼2° and ∼1.4°, respectively. From these results it follows that LSMO chemically reacts with YSZ to form LZO. Pole figures from XRD^2 measurements were also recorded for the most intense $(222)_{\mathrm{LZO}}$ reflection, with 2θ=28.6° (not shown). Next to the substrate $(111)_{\mathrm{YSZ}}$ reflection at 2θ=30°, we detected, in the 1300°C heat-treated sample, a notable shoulder, absent in 900°C treated samples. Despite being difficult to resolve due to the nearby intense and wide substrate peak, it was already sufficient to prove that LZO grows cube on cube on top of YSZ, i.e. $(001)_{\mathrm{LZO}}[100]||(001)_{\mathrm{YSZ}}[100]$ ¶. This epitaxial relation gives a lattice mismatch ϵ=-4.45% (2 YSZ unit cells $2a_{YSZ}$=10.3 Å, are matched to one LZO unit cell a_{LZO}=10.78 Å).

In conclusion, our findings show the formation of epitaxial LZO grown from the interfacial reactivity of the YSZ substrate in contact with LSMO at 1300°C. In fact, a subtle indication of LZO formation, not yet at expenses of LSMO formation, is already detected at large annealings (24 h) at 1000°C. The reaction between YSZ and LSMO grown with different methods and subject to different heat treatments has produced a large body of work, mainly prompted by the great interest of the LSMO/YSZ cathode-solid electrolyte system for Solid Oxide Fuel Cells (SOFCs) [184–187]. It is generally accepted that long annealing times and high temperatures can yield an evaporation or diffusion of Mn into YSZ, along with the reaction of La with (Yttrium doped) zirconia [185, 188]. Insulating and with 1000 times less ionic conductivity than YSZ, LZO severely hampers the adequate operation of SOFCs. Consequently, in both the search for ferromagnetic self-assembled nanostructures,

¶Alternatively, the fact that no peak appeared at any other ϕ value different from the substrate ϕ value yields the same conclusion.

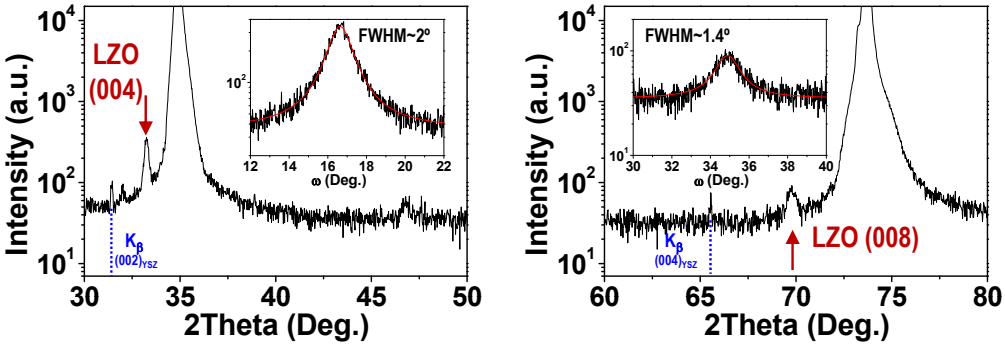

Fig. 3.31: *Zoomed-in θ-2θ scans from Fig. 3.30 (b). The peaks marked with red arrows indicate the* $(004)_{\mathrm{LZO}}$ *and* $(008)_{\mathrm{LZO}}$ *reflections. The rocking curves of those two peaks are displayed in the insets of the graphs.*

and for SOFC applications, it is of considerable relevance to determine the experimental conditions at which this reaction occurs.

3.4.2 Morphology of self-assembled LSMO nanoislands on YSZ

So far we have discussed the evolution of the LSMO self-assembled nanoisland system and illustrated the general trends in island thickness and lateral size distribution. The crystallographic orientations of two island populations, the predominant out-of-plane $(001)_{\mathrm{LSMO}}$ and the less abundant $(111)_{\mathrm{LSMO}}$ [in the following named $(001)_{\mathrm{LSMO}}$-oriented and $(111)_{\mathrm{LSMO}}$-oriented nanoislands], were also determined. In this section we will focus on the detailed individual morphology of the LSMO nanoislands. This knowledge will be necessary for later studies on the magnetic properties of the nanoislands.

Main morphologies of LSMO nanoislands on YSZ

Fig. 3.32 summarizes the general aspect of the standard system of self-assembled LSMO nanoislands grown from a 0.03 M solution at 900°C for 3 h. The $1.5\ \mu\mathrm{m} \times\ 1.5\ \mu\mathrm{m}$ AFM image in Fig. 3.32 (a) shows the nanoisland ensemble, which consists of a majority of square-base nanoislands and also includes one triangular structure. The truncated edges of the triangle are a common feature of these structures. The line profile in Fig. 3.32 (b) evidences typical nanoisland sizes with thickness $t\sim$20-35 nm and lateral size $D\sim$120 nm. These values are approximate due to the AFM tip-nanoisland convolution, which also precludes resolving the actual angle of the island facets.

The geometry and facets of the nanoislands may be derived from cross-section TEM images such as the low magnification TEM micrograph in Fig. 3.33 (top row). The high resolution (HR) low magnification images in the lower panel display two individual LSMO islands: Fig. 3.33 (a) shows the truncated pyramid morphology of a square-base $(001)_{\mathrm{LSMO}}$-oriented island and, next to it, Fig. 3.33 (b) displays a large flat $(111)_{\mathrm{LSMO}}$-oriented nanoisland, i.e. triangle-based. The inclined facets in (a) are found to be the $(111)_{\mathrm{LSMO}}$ crystallographic planes, as deduced from the projected $\sim$55° angle of the facet with respect to the [001]-substrate horizontal direction. The square-base $(001)_{\mathrm{LSMO}}$-oriented nanoislands are thus truncated pyramids limited by lateral $(111)_{\mathrm{LSMO}}$ facets and top and bottom

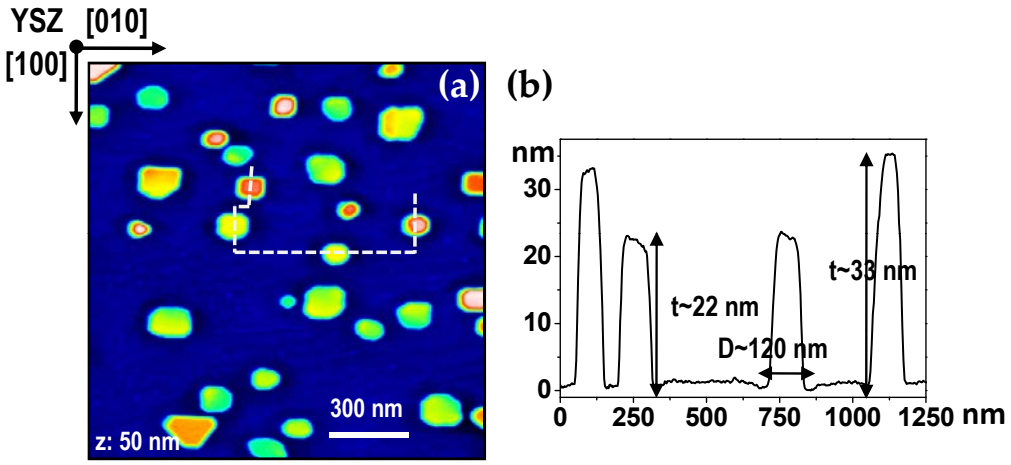

Fig. 3.32: *(a) 1.5μm $\times$ 1.5μm AFM topography image of a 0.03 M 900°C 3 h treated LSMO on YSZ self-assembled nanoisland system. (b) Line profile corresponding to the dashed line in (a), showing the typical nanoisland sizes.*

$(001)_{\mathrm{LSMO}}$ planes. Regarding the triangular islands, Fig. 3.34 (a) shows the TEM image of a $(111)_{\mathrm{LSMO}}$-oriented nanoisland, seen along the $[-110]_{\mathrm{LSMO}}$ direction. The projected lateral facets of the image are in agreement with $(1-1-1)_{\mathrm{LSMO}}$ and $(001)_{\mathrm{LSMO}}$ crystallographic planes, as indicated in the image. TEM image analysis are thus consistent with $(111)_{\mathrm{LSMO}}$ top facets laterally bounded by $\{1-11\}_{\mathrm{LSMO}}$ planes at ~70.5° from the top plane, truncated at the edges by $(001)_{\mathrm{LSMO}}$ facets. A top-view drawing of the nanoisland orientation is sketched in the lower panel. Fig. 3.34 (b) shows a 3D model of the $(111)_{\mathrm{LSMO}}$-oriented LSMO nanoisland, displaying its facets and the epitaxial relationship with respect to YSZ.

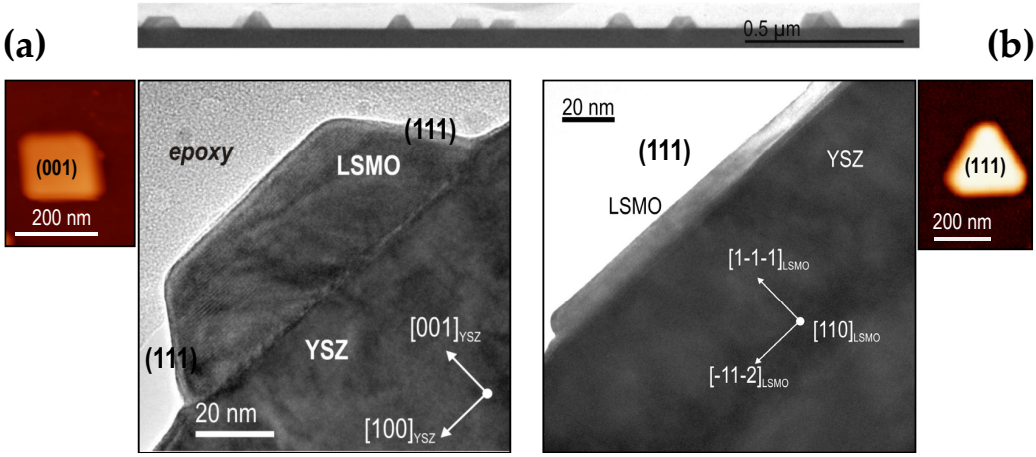

Fig. 3.33: *(Top-row) Low resolution TEM cross-section image of a collection of self-asssembled LSMO nanoislands on YSZ. (a)&(b) HR low magnification cross-section images of (a), a $(001)_{LSMO}$-oriented nanoisland, exhibiting a truncated pyramid geometry shaped by (111) lateral facets, and (b), a $(111)_{LSMO}$-oriented nanoisland. The YSZ substrate and the LSMO island are viewed along the [010] and [110] zone axes, respectively. The AFM images next to the TEM images indicate the in-plane morphology of each of the islands. TEM images courtesy of P. Abellán.*

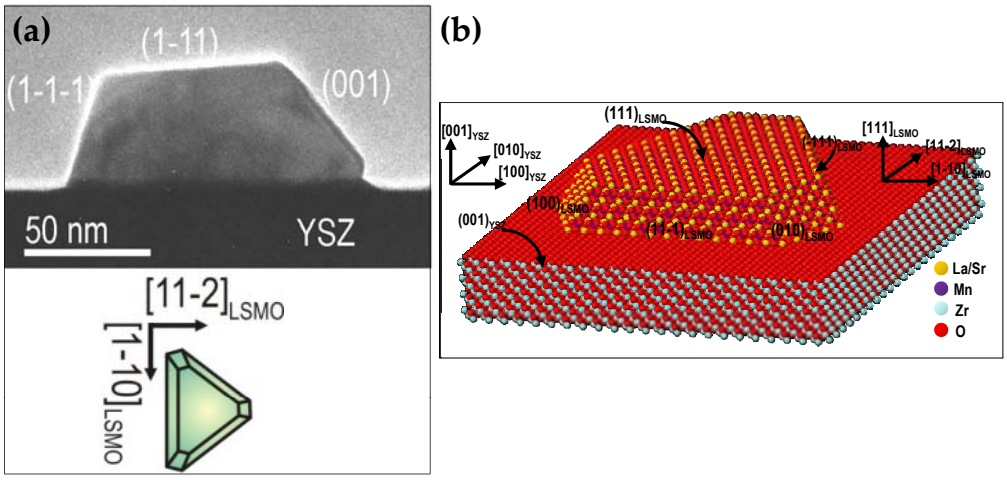

Fig. 3.34: *(a) TEM image of a* $(111)_{\mathrm{LSMO}}$*-oriented nanoisland showing its facets. The nanoisland is seen along the* $[-110]_{\mathrm{LSMO}}$ *direction. Courtesy of P. Abellán. A top-view drawing of the nanoisland is sketched below. (b) 3D model for the* $(111)_{LSMO}$*-oriented island showing its facets and its epitaxial relationship with respect to the substrate. Note that the truncated edges correspond to* $\{100\}$ *planes. The simulation is done using the program 'Rhodius' from Universidad de Cádiz [189, 190] (courtesy of Prof. J. Arbiol).*

The above results concern the main structures observed in the LSMO/ YSZ system under standard treatment conditions, i.e. 900°C annealing for 1 to 3 h. However, the LSMO/YSZ system exhibits an alternative island morphology which can arise from identical processing conditions as the ones just mentioned. Fig. 3.35 illustrates this fact: it shows two $1.5\ \mu\mathrm{m} \times 1.5\ \mu\mathrm{m}$ AFM images, (a) and (b), of two samples grown from 0.03 M solutions processed at 900°C for 1 h. While in (a) we obtain the previously described arrangement of well separated triangular and square-base islands, Fig. 3.35 (b) displays a much denser assembly featuring square islands which appear rotated by 45° with respect to the square islands of Fig. 3.35 (a). Strictly speaking, the base of these new islands is not necessarily squared, but it shows a trend towards a rectangular shape. For the sake of simplicity, however, we are going to name the squares from sample (a) *regular-squares* and those in (b) *rotated-squares*. The difference in morphology is apparent in the amplitude images (a') and (b'). Interestingly, XRD pole figure measurements for the sample featuring rotated-squares gave exactly the same epitaxial relationship as the one discussed for regular-square $(001)_{\mathrm{LSMO}}$-oriented nanoislands, i.e.$(001)_{\mathrm{LSMO}}[110]||(001)_{\mathrm{YSZ}}[010]$. This is illustrated in the sketches of Figs. 3.35 (a") and (b"). As a result of having the same crystallographic orientation it follows that the oblique facets of the rotated-squares cannot be the $(111)_{\mathrm{LSMO}}$ facets, as in the case of the regular-square nanoislands. Simulations of the system were done in collaboration with Prof. J. Arbiol using the *Rhodius* simulation tool from UCA (Universidad de Cádiz) [189, 190]. A number of possibilities including the $\{101\}$ and $\{201\}$ family of planes were revealed as possible options for the inclined facets of the rotated-squares. However, TEM cross-section studies would be required for confirmation. In brief, in this alternative configuration, the crystallographic orientation of nanoislands remains the same and only the morphology of the islands changes, accompanied by a qualitative change in the self-assembly, which proceeds via formation of smaller and closely spaced nanoislands.

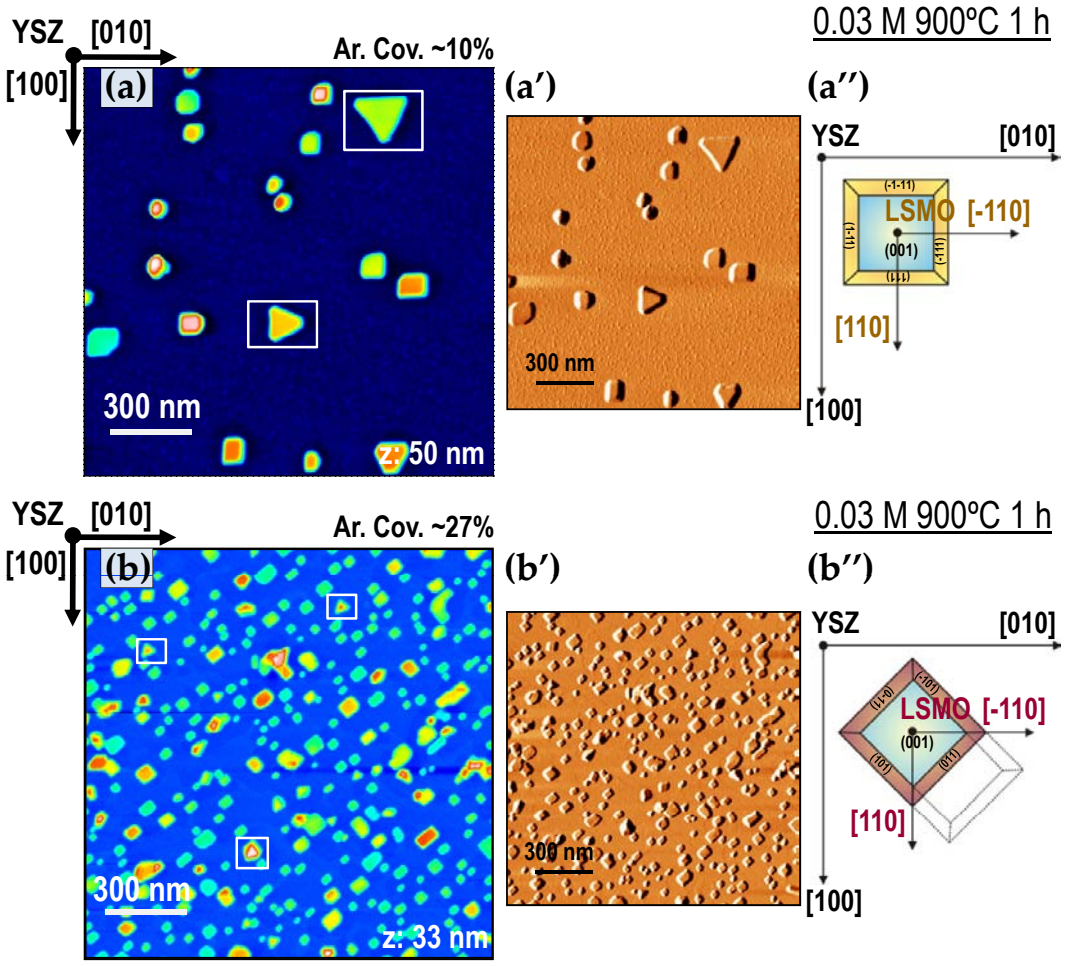

Fig. 3.35: *Morphological differences exhibited by LSMO nanoisland ensembles after identical growth processing. (a)&(a') 1.5μm × 1.5μm AFM topography and amplitude images, respectively, of the sample with $(001)_{LSMO}$-oriented regular-squares. It exhibits some $(111)_{LSMO}$-oriented islands (triangles) as well. The area coverage is in the 10-15% range. (b)&(b') 1.5μm × 1.5μm AFM topography and amplitude images, respectively, of the sample featuring closely packed rotated-square islands, 45° rotated with respect to the regular-square islands in (a). Some very few triangular islands may also be detected, far smaller than their (a) image counterparts (inside white squares). Area coverage ranges between 25-35%. The epitaxial arrangement of the square-base nanoislands in both samples is identical, as sketched in (a") and (b"). Nonetheless, the truncated square pyramids in (a") display $(111)_{LSMO}$ lateral facets, while the islands in (b") show different facets. One of the possibilities, the {101} family of planes, is indicated in (b").*

Study of the possible mechanisms driving the LSMO nanoisland morphologies on YSZ

In order to examine the driving force responsible for the regular and rotated-square nanoisland shapes, we first considered the substrate surface. The critical role of the substrate surface in the self-assembly of epitaxial nanoislands is a widely accepted issue, yet not always well understood. Surface defects, step kinks and edges, typically provide preferential nucleation sites, and also may influence the growth kinetics of the first formed nuclei [191, 192]. The morphology of the substrate surface will also affect the stress distributions within a nanostructure and, consequently, its relaxation mechanisms. For instance, the formation of dislocations will vary for islands nucleated on a flat terrace or on a kink. These issues have been investigated by Hesse and co-workers, also in oxide heteroepitaxial systems. Their studies show the impact of substrate pits and steps on the morphology and domain distribution of oxide nanoislands, as compared to islands grown on perfectly flat YSZ substrates [176, 193, 194].

In an attempt to associate our observed LSMO morphologies to some underlying substrate pattern, we analyzed the YSZ substrate surface characteristics. Fig. 3.36 shows the AFM images of four LSMO/YSZ nanostructured samples. In them, either rotated-square [(a) and (b)] or regular-square [(c) and (d)] nanoisland are present, after identical growth processing. We can also identify a few triangles. AFM topography images ($1\ \mu m \times 1\ \mu m$, at the center of the figure) are thresholded, i.e. their z scale is reduced in order to better see the height distribution within the substrate surface. This makes the island morphology blurry, and therefore we have included the phase images corresponding to each sample ($0.5\ \mu m \times 0.5\ \mu m$, in gray). The latter images clearly display the distinct island morphologies. The surface steps in the images exhibit one unit cell heights. An example is given for Fig. 3.36 (a).

An analysis of Fig. 3.36 (a), reveals remarkably large substrate terraces, $\lambda \sim 400$ nm wide, displaying plenty of kinks and holes. Note also that most of the nanoislands are located at the edges of substrate steps. A very different landscape emerges from Fig. 3.36 (b), where substrate terraces are very narrow and smooth, and hence the islands occupy more than one terrace. Although, again, island nucleation is likely to happen at the steps edges, the large size of the structure with respect to the terrace width makes this point difficult to confirm. Still, the interaction between island and substrate is clearly revealed in the curving of the substrate step at nanoislands locations, (some of this bending is signaled with arrows). Note that a similar influence of the island on the substrate terrace is apparent in Fig. 3.36 (c): the substrate steps near an island curve towards the high level side. Furthermore, $\sim$5 u.c. high trenches develop around the islands, as revealed by the dark halos surrounding the structures, and by the line profile displayed at the left of the image. Previous works suggest that these trenches develop via diffusion of surface molecules from the immediate surroundings towards the nanostructures [193, 194]. In any case, it appears that both in Figs. 3.36 (b) and (c) the substrate surface morphology and the effect of the island presence on the substrate steps are comparable. Despite similar substrate-nanoisland interaction one sample features rotated-square islands and the other regular-square structures. An intermediate terrace width is found in Fig. 3.36 (d), where the bending of the substrate due to the presence of islands also occurs. Note how in this case, as the island size is slightly smaller than the terrace width, one can clearly see that the nanoisland sits on the step edge, which curves at the sides of the structure. It is not difficult to imagine, in a subsequent evolutionary stage, the complete receding of the step to yield a similar situation as that observed in Fig. 3.36 (c).

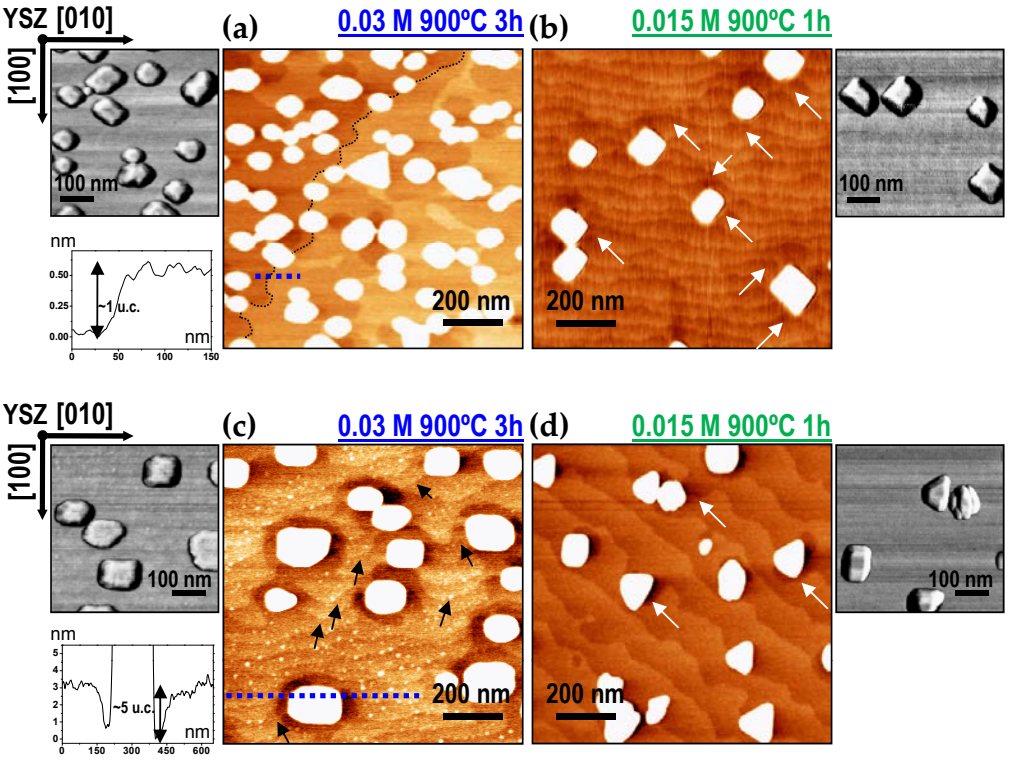

Fig. 3.36: *Two 0.03 M 900°C 3 h and other two 0.015 M 900°C 1 h samples featuring either rotated-square (top row) and regular-square island (bottom row) morphologies. The $1\mu m \times 1\mu m$ AFM topography images, in the center, are thresholded in order to emphasize the underlying substrates' step-terrace structure. Phase images at the sides of the topography images, $0.5\mu m \times 0.5\mu m$, in grey, show the different nanoisland shapes, either rotated or regular-square. Substrate terraces vary from wide in (a) to very narrow in (b) and (c). They display 1 u.c. of step height, exemplified by the line scan in (a) (blue dashed line marks the exact place of the profile). In sample (c) islands appear surrounded by ∼5 u.c. high trenches, depicted in the corresponding line profile. Little arrows throughout the images indicate some of the substrate step bending.*

From the above results we deduce that the specific substrate step-terrace morphology is not a determining factor deciding whether rotated-square or regular-square island morphologies will occur. This is suggested by the fact that nanoisland-substrate interactions appear to be independent of the nanoisland shape.

Once we have ruled out the substrate surface as the driving force for a specific nanoisland shape, we need now to consider the nanoislands by themselves. The fact that nanoislands from samples grown after the same treatment show either $\{111\}_{LSMO}$ or $\{101\}_{LSMO}$ crystallographic planes (supposing we have the latter family of planes in the rotated-square nanoislands) suggests that the surface energies of these facets might be of comparable magnitude. No surface free energy values for different $La_{0.7}Sr_{0.3}MnO_3$ crystal planes are reported in the literature. For similar compounds such as $La_{1-x}Ca_xMnO_3$, however, no strong differences are reported for the energies of low index crystal planes, with values that vary very slightly from one crystal plane to another and which further depend on the specific chemical termination [whether Mn-terminated or La/(Ca,Sr) terminated] [158].

Within the hypothesis of two energetically close scenarios one would in principle expect both nanoisland morphologies to coexist on the same sample. This situation, however, was very rarely observed in the more than three dozens of processed samples. This observation underlines the relevance of island-island interaction (in addition to the similarity in surface free energies of the LSMO facets): once the system has opted for a certain nanoisland morphology, either regular or rotated-square, this will be the shape of all of the nanoislands[‖]. To corroborate this picture it is useful to verify whether one island morphology may be closer to the thermodynamic equilibrium than the other. For that purpose we studied early and advanced evolution stages of the system by moving away from the 900°C 1-3 h heat treatments presented so far, as we explain next.

Fig. 3.37 shows the experimental results of LSMO on YSZ self-assembled nanoisland systems at advanced stages [$T \geq$900°C, (a) and (b)] and fairly initial stages [(c) and (d)] of its evolution. As also done in Fig. 3.36, we threshold the AFM topography images, and we also provide zoomed-in phase images that reveal the morphology of the nanoislands. The first thing we notice is that all samples, whether in the initial or in the advanced stage, exhibit the rotated-square nanoisland morphology. In fact, the examples shown in Fig. 3.29, annealed at $T \geq$1000°C, already showed this rotated-square morphology. Therefore, we can dismiss the hypothesis that there is a gradual shape evolution from a less stable configuration towards a more stable equilibrium configuration. Nevertheless, further experiments are required to prove if regular-squares are never achieved at the extreme conditions, i.e. at high temperatures and long annealing times, and at low temperatures and short annealing times. At present, we do not have enough statistics to rule out such possibility. Concerning the substrate surface, note that the high T and long annealing in Fig. 3.37 (a) results in a strong step meandering, with step heights as large as $\sim$5 u.c.; these again emphasize the redistribution of substrate material in this nanostructured system, as we already observed in Fig. 3.36 (c). Remarkably, although the substrate behavior was similar in Fig. 3.36 (c), the nanoisland shape was regular-square, while here it displays rotated-square shape. This once more confirms that the substrate morphology does not determine the nanoisland shape.

In summary, in this section we have presented the study of the LSMO nanoisland

[‖] When talking about the different nanoisland morphologies we are only considering $(001)_{\mathrm{LSMO}}$-oriented islands, i.e. not the triangular islands. Triangles have a different crystallographic orientation, and thus their formation is decided at the nucleation stage.

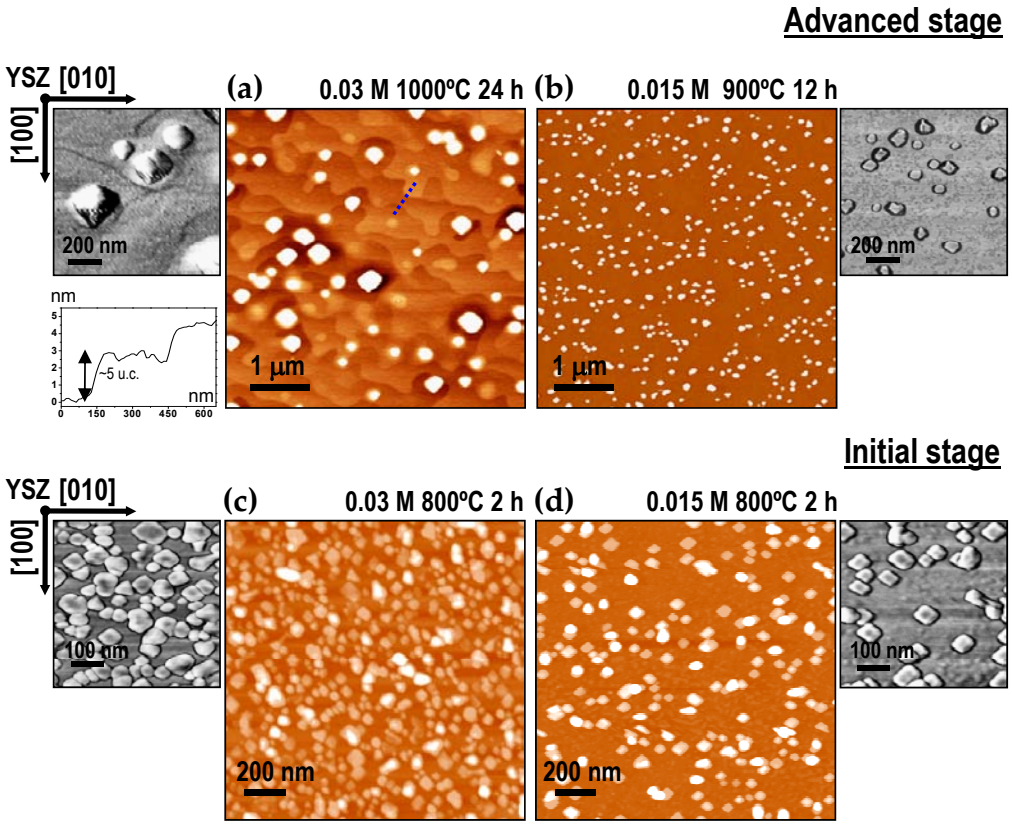

Fig. 3.37: *Comparison of the nanoisland morphologies obtained at advanced stages (top row) and initial stages of the system evolution (bottom row). All of the examples feature rotated-square nanoislands. AFM topography images (in the center of the figure) are thresholded in order to observe the underlying substrate morphology while, at their sides, phase images illustrate the nanoisland shape. High T and long annealing times in (a) result in the substrate terrace meandering and in the building of steps as high ∼5 u.c. In (b), although clean, the substrate does not form a clear step-terrace structure. Finally, the initial evolution stage and the density of the system imaged in (c) and (d) suggest that there may be considerable amount of material left on the substrate.*

morphology on YSZ. We have shown that $(001)_{\mathrm{LSMO}}$-oriented and $(111)_{\mathrm{LSMO}}$-oriented nanoislands display square-base truncated pyramid and triangular-base shapes, respectively, faceted along well-defined crystallographic planes. We have also demonstrated that $(001)_{\mathrm{LSMO}}$-oriented nanoislands exhibit two possible morphologies, either regular-square or rotated-square. The crystallographic orientation of both nanoislands is identical, which indicates that they are shaped by different LSMO lateral facets. Our results also show that both $(001)_{\mathrm{LSMO}}$ configurations appear under identical processing conditions, suggesting they are energetically close. These two morphologies do not appear to coexist, which suggests that island-island interaction may play a key role. Additionally, we have shown that the nanoisland morphology, whether regular or rotated-square, does not depend on the substrate morphology. Surface steps, when treated at high T and/or for long times, undergo strong bending and meandering, attaining heights that are well above one unit cell. Finally, there appears not to be an 'initial stage' or 'advanced stage' morphology, although a more exhaustive study would be necessary to conclusively correlate the influence of the heat treatment on the final nanoisland configuration.

3.4.3 Magnetic Characterization of LSMO on YSZ self-assembled nanoislands

After having investigated the growth aspects of CSD-derived self-assembled LSMO nanoislands grown on YSZ, we now turn to the study of their macroscopic magnetic properties. The present section will focus on the macroscopic magnetic properties of the LSMO on YSZ nanoisland system, while the nanoscale magnetic behavior will be addressed in the following chapters.

Magnetization loops and Curie Temperature

Macroscopic magnetization measurements were carried out in a SQUID magnetometer (Quantum Design MPMS-XL7) at temperatures between 10 K to 300 K and varying magnetic fields from 0 T to 7 T. Fig. 3.38 shows the in-plane isothermal magnetization loops measured for a collection of epitaxial LSMO nanoislands grown on YSZ from a 0.015 M solution, heat treated at 900°C for 1 h [see the appearance of the system in Fig. 3.19 (b)]. We have plotted the SQUID measured signal, i.e. the magnetic moment m, against the in-plane applied field H. The substrate diamagnetic response (M linear dependency against H) has been subtracted in order to extract the ferromagnetic (FM) behavior specific to the LSMO nanoislands. Note that we measure m values below 2×10^{-5} emu, near the effective resolution limit of our measurements, which we found to be in the $\sim 10^{-6}$ emu range. Recall that 0.015 M yields an ultra-thin FM layer with $t_{eq}\sim$1.5 ($\pm$0.5) nm (see Fig. 3.20). For higher concentrations, the signal to noise ratio improves (Fig. 3.40 shows a representative example of a 0.03 M sample). The bottom row of Fig. 3.38 displays the magnified view of the center of the loops, to better appreciate the M vs H dependency. Coercive fields H_C decrease from $\sim$200 Oe at 35 K, down to $\sim$150 Oe at 110 K, and $\sim$20 Oe at 300 K. The saturation and remanence magnetic moment, as well as the coercive field inferred from Fig. 3.38, are summarized in Tab. 3.2.

In Fig. 3.39 we show the saturation magnetization values M_S deduced from the hysteresis loops for a number of samples with nanoislands grown from distinct concentrations. Here $M_S = \frac{m_s}{V} = \frac{m_s}{St_{eq}}$, with m_s the saturation magnetic moment, S the substrate surface

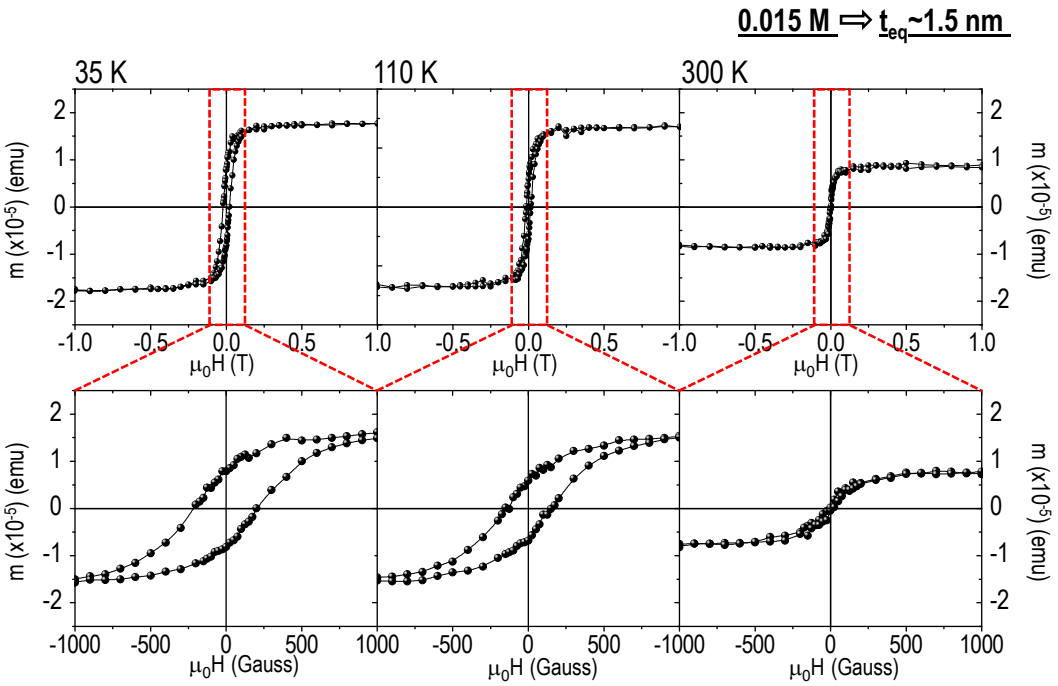

Fig. 3.38: *Isothermal magnetization loops for various temperatures measured with SQUID. The bottom row displays a magnified view of the center of each loop. The sample of self-assembled LSMO nanoislands was grown from a 0.015 M precursor solution, i.e. t_{eq}~1.5 nm, treated at 900°C for 1 h, see Fig. 3.19 (b).*

T (K)	$\mathbf{m}_S(\times 10^{-5})$ (emu)	$\mathbf{m}_r(\times 10^{-5})$ (emu)	$\mathbf{H}_C$ (Oe)
35	1.8	0.8	214
110	1.7	0.7	150
300	0.86	0.2	20

Tab. 3.2: *Magnetic moment and coercive field values inferred from Fig. 3.38.*

(5 mm $\times$ 5 mm) and t_{eq} the equivalent film thickness. The large error bars in Fig. 3.39 associated to M_S, are given by the expression $\Delta M_S = \left|\frac{\partial M_S(t_{eq})}{\partial t_{eq}}\right| = \frac{m_s}{St_{eq}^2}\Delta t_{eq}$, i.e. they originate from the large uncertainty in the estimate of the t_{eq} values (see Tab. 3.1). For comparison, we have plotted bulk LSMO M_S values at different temperatures, taken from the work of Park et al. [19]. In addition to the expected decrease of M_S with T, we observe that the saturation magnetization values of the LSMO nanoisland ensemble are not far from the reported values for bulk LSMO, which is a remarkable fact considering the island nanometric dimensions, typically below $t\sim$40 nm and $D\sim$200 nm in thickness and lateral size, respectively. Only for 300 K the measured magnetization seems to diverge more substantially from the values reported for bulk LSMO. It is also worth emphasizing the general trend of decreasing magnetic signal with decreasing solution concentration. We shall go back to discussing this point later in the section. Let's also remark that the 0.03 M LSMO ultra-thin films on STO and LAO studied at the beginning of this chapter exhibited saturation magnetizations in the order of ~230 kA/m at 35 K, which is more than a factor 2 smaller than the M_S values obtained for LSMO nanoislands on YSZ, grown from 0.015 M (~480 kA/m at 35 K) and 0.03 M (~465 kA/m at 110 K) solutions. Tab. 3.3 collects the data which yield the plot in Fig. 3.39.

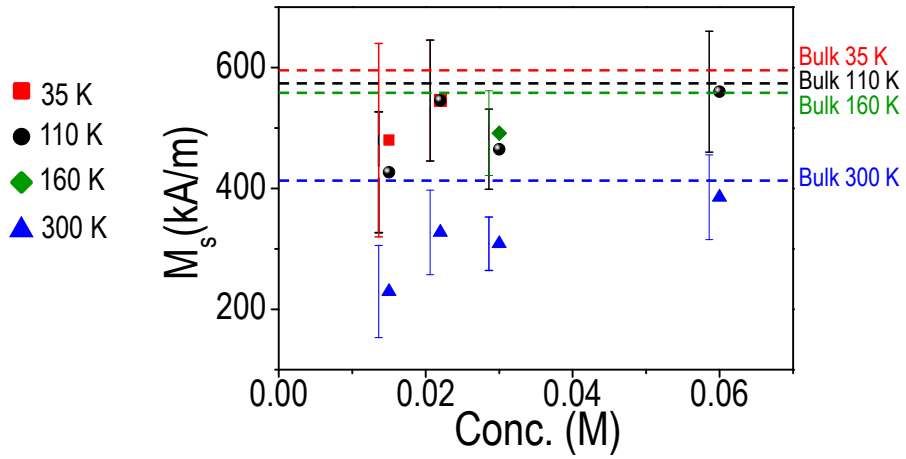

Fig. 3.39: *In-plane M_S values for various temperatures, of different self-assembled LSMO nanoislands on YSZ. The horizontal axis indicates the precursor concentration. The plotted data are listed in Tab. 3.3. The dashed lines indicate the bulk LSMO M_S values from the work of Park et al. [19].*

Fig. 3.40 shows the magnetization curves measured at 110 K for a 900°C 3 h sample grown from a 0.03 M solution [see Fig. 3.32 (a)], both with in-plane and out-of-plane applied field. The two hysteresis loops in Fig. 3.40 reveal that the easy magnetization axis of our system of self-assembled epitaxial LSMO nanoislands lies within the sample plane. An in-plane easy axis is expected in ferromagnetic thin films, due to the strong shape anisotropy [195]. Such a behavior is not straightforward in 3D objects, nor in compressively strained nanoscale systems. As a matter of fact, thin LSMO films grown under compressive strains have been reported to exhibit an out-of-plane easy magnetization axis as a consequence of the magnetoelastic contribution [27, 28, 196]. Nevertheless, in our LSMO nanoislands, the nominal $\epsilon\sim$-6% compressive strain is relaxed, and, on the other hand, although, strictly speaking, they are 3D objects, they are rather flat islands with typical D/t values larger than 4. The overall behavior, in the end, is that it results easier to satu-

Conc. (M)	$\mathbf{t}_{eq}$ (nm)	$\Delta\mathbf{t}_{eq}$ (nm)	**T** (K)	$\mathbf{m}_S(\times\mathbf{10}^{-5})$ (emu)	$\mathbf{M}_S$ $(\frac{\text{emu}}{\text{cm}^3})$	$\Delta\mathbf{M}_S$ $(\frac{\text{emu}}{\text{cm}^3})$	$\Delta\mathbf{M}_{S,rd.}$ $(\frac{\text{emu}}{\text{cm}^3})$	$\mathbf{H}_C$ (Oe)	**No.Samp.** _
0.015	1.5	0.5	35	1.8	480	160	200	200	1
			110	1.6	427	142	100	130	2
			300	0.86	229.3	76	80	20	1
0.022	2.2	0.5	35	3.1	563	128	100	155	1
			110	2.9	527.3	120	100	115	1
			300	1.8	327	74	70	20	1
0.03	3.5	0.5	110	4.07	465	66	70	115	3
			160	4.3	491	70	70	90	1
			300	2.7	309	44	40	20	2
0.06	5.5	1	110	7.7	560	102	100	100	1
			300	5.3	386	70	70	30	1

Tab. 3.3: *In-plane saturation magnetic moment* $\mathrm{m_s}$ *and magnetization* $\mathrm{M_s}$ *values for a set of different solution concentrations, measured by SQUID.* ΔM_S *is the error associated to* $\mathrm{M_S}$*, due to the uncertainty in the* $\mathrm{t_{eq}}$ *equivalent thickness estimation.* $\Delta M_{S,rd.}$ *represents the error rounded up to a single significant figure. 1 emu/cm*^{3}*= 1 kA/m.*

rate the system with an in-plane applied magnetic field than with an out-of-plane field. In order to determine which in-plane direction is the easy magnetization axis, we conducted Ferromagnetic Resonance experiments, which we shall discuss in the next section.

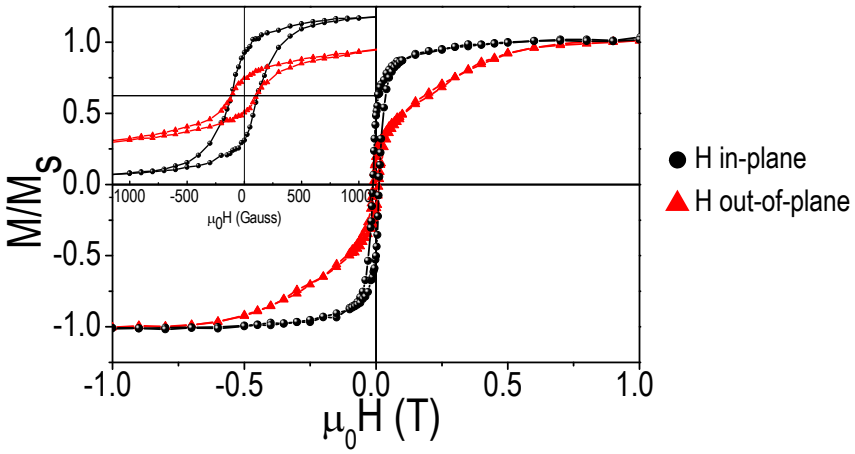

Fig. 3.40: *Normalized magnetization vs H loops at T=110 K for magnetic fields applied in-plane (black dots) and out-of-plane (red triangles), indicating that the easy axis of the self-assembled LSMO nanoisland system lies within the sample plane. The sample was grown from 0.03 M solution, heat-treated at 900°C 3 h. A magnified view of the center of the cycles is given in the inset.*

Fig. 3.41 shows the temperature dependence of the saturation magnetization of LSMO on YSZ nanoislands grown from 0.015 M and 0.03 M precursor solutions. The Curie temperature deduced from the plots, T_c∼350±5 K, is close to that of bulk LSMO (T_C∼360 K [82]), which is quite a remarkable result for sub-200 nm wide ∼20-30 nm thick nanostructures. This high T_C value can be correlated to the absence of strain within the islands

-deduced from XRD and TEM investigations- and also to the non-invasive self-assembly growth process, which prevents the degradation of the magnetic properties caused by ion implantation or radiation damage induced by nanolithography processes [66]. A T_C ∼350 K value was also measured for the 0.06 M nanostructured sample (not shown).

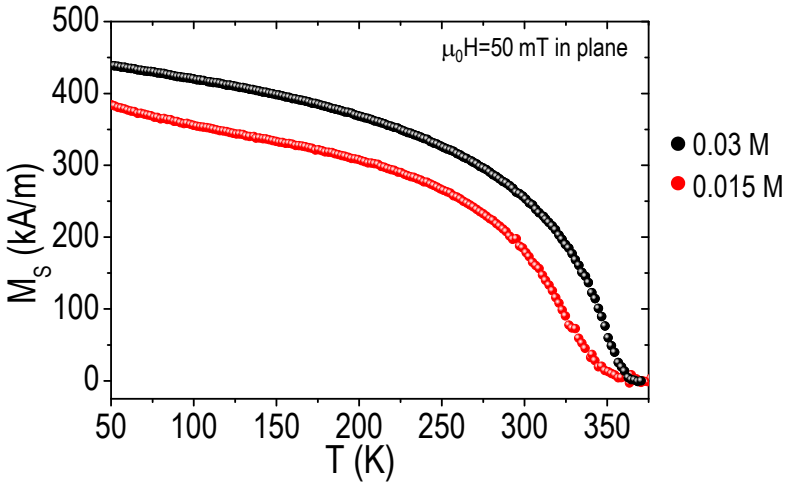

Fig. 3.41: *Saturation magnetization as a function of temperature for two LSMO on YSZ nanoisland samples grown from 0.015 M and 0.03 M precursor solutions. T_C takes a value close to 350 K. A 50 mT in-plane magnetic field was applied.*

It is noteworthy that the magnetic signal plotted in Fig. 3.41 is larger in the case of the 0.03 M sample, consistent with the general trend that emerges from Fig. 3.39, which shows larger M_S values for increasing concentration values. For smaller precursor solution concentrations, the general tendency is to have smaller self-assembled nanoislands, i.e. increased surface to bulk ratios. Lower magnetic signals could thus be related to the presence of a ferromagnetic dead layer. As already mentioned for LSMO on STO and LAO, the existence of ferromagnetic dead layers is associated to free surfaces and interfaces of manganite thin films and nanostructures. Such surface and interface layers are precisely the places where the lattice symmetry is broken, defects and non-stoichiometries may be important, and the Mn^{3+}-O^{2-}-Mn^{4+} angles distort with respect to the bulk [25, 26, 197].

Fig. 3.42 shows the volume fraction within an individual LSMO nanoisland which would be non ferromagnetic, plotted as a function of D for specific t values. We have considered the last 1 nm or 2 nm of the nanoisland to be a ferromagnetic dead layer. The calculations are done for $(001)_{\mathrm{LSMO}}$-oriented regular-square islands (the island sketch is plotted next to the graph of Fig. 3.42). We have derived the non-FM volume by multiplying the dead layer thickness (assuming an homogeneously thick layer) to the area of the square-base truncated pyramid. As it follows from the plot, the larger the island (larger t and D), the smaller is the non-ferromagnetic fraction. If we take, for instance, a common D value of 120 nm, the percentage of non-FM volume can vary from an upper limit of ∼44% (if we consider a 2 nm dead layer in a t=10 nm thick island), to a lower limit of ∼11% (for a t=30 nm island and taking a 1 nm thick dead layer). These two limits are indicated in Fig. 3.42. The difference between the magnetization of a 0.03 M derived LSMO nanoisland system (M_S∼465 kA/m at T=110 K, see Fig. 3.39 and Tab. 3.3) and that of bulk LSMO from Park et al. (∼575.25 kA/m at T=110 K) [19] gives a non-FM volume of ∼20%, which is within the

range of our calculated non-FM volume fractions. We will further comment on the dead layer in the context of the LSMO nanoisland nanoscale analysis of Chapters 4 and 5.

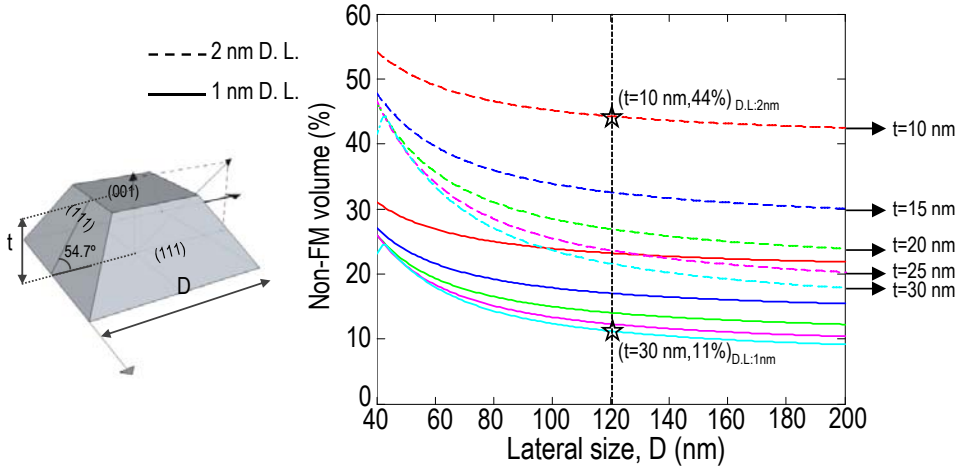

Fig. 3.42: *Non-FM volume percentage within a $(001)_{LSMO}$-oriented nanoisland, considering 1 nm (dashed lines) and 2 nm (solid lines) thick FM dead layers (D. L.). The different colors stand for different island thickness values, i.e. 'red'=10 nm, 'blue'=15 nm and so on. The sketch on the left hand side remarks the nanoisland geometry.*

In-plane magnetic anisotropy and magnetocrystalline anisotropy constant measurement through FMR

Ferromagnetic Resonance (FMR) experiments were conducted to study the in-plane magnetic anisotropy of the system of self-assembled LSMO nanoislands on YSZ. These measurements were performed in a Bruker ESP 300 spectrometer operated at 9.5 GHz in a rectangular X-band cavity operating in the TE102 mode. The FMR spectra reported here were done at 150 K keeping the applied field, H, in the sample plane. A representative 0.03 M 900°C/ 2 h sample, like the one imaged in Fig. 3.21 (a) was measured. Hence, a sample consisting of regular-square pyramidal nanoislands. The results here presented are the outcome of the collaboration with Dr. C. A. Ramos and Dr. R. D. Zysler from *Centro Atómico* and *Instituto Balseiro* in Bariloche, Argentina. Fig. 3.43 shows the measured in-plane angular dependence of the resonant field H_r. This value is obtained at each angle by fitting the FMR spectra with a Lorentzian lineshape. Experimental data show a clear angular dependence of H_r at 150 K. Note that a minimum in H_r indicates an easy magnetization axis, in this case the [110] axis of the LSMO nanoislands.

To explain the origin of the observed anisotropy we followed a standard formalism [198]. The energy density function is defined as follows, developing up to the first order the magnetocrystalline anisotropy term:

$$E = -\mu_0 \vec{H}\vec{M} + \frac{\mu_0}{2} M^2 (N_x \alpha_x^2 + N_y \alpha_y^2 + N_z \alpha_z^2) + K_1 (\alpha_x^2 \alpha_y^2 + \alpha_x^2 \alpha_z^2 + \alpha_y^2 \alpha_z^2) \qquad (3.2)$$

where the first term represents the Zeeman energy, the second is the magnetostatic contribution (N_x, N_y, N_z are the demagnetizing factors) and the third is the cubic crystalline anisotropy, with α_i the direction cosines of the magnetization $\vec{M}$. In this in-plane configuration, no magnetoelastic contribution should be expected since the strain exerted by the

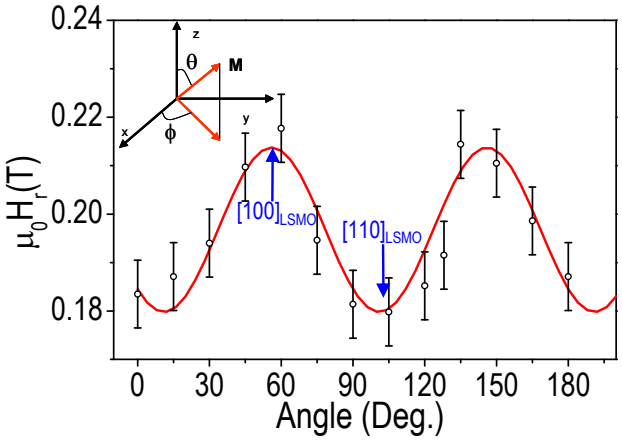

Fig. 3.43: *FMR results. Open symbols represent the measured in-plane dependence of the resonant field H_r at 150 K. The solid line is the fitting to the experimental data according to Eq. 3.4. The inset shows the coordinate system used. The H_r minima, when the field is applied parallel to the $[110]_{LSMO}$ direction, indicate an easy magnetization axis.*

substrate on the pseudocubic LSMO is isotropic [195]. Moreover, we can rule out any possible deviation from a truly isotropic in-plane strain because nanoislands are fully relaxed. Concerning the magnetostatic contribution, we estimated the demagnetizing field of a flat square-based pyramid magnetized perpendicularly to its base and found $N_\perp = 0.70 \pm 0.05$ for island aspect-ratio *D/t* in the range of 4±1, which are the typical values found for this kind of sample. Considering $N_x + N_y + N_z = 1$ ($N_x = N_y = N_\parallel \sim 0.15$) it turns out that the effective shape demagnetizing factor for the applied field, $\vec{H}$, parallel to the pyramid base, depends only on the difference $N_\perp - N_\parallel \equiv \Delta N$. We rewrite Eq. 3.2 using the coordinate systems sketched in the inset of Fig. 3.43:

$$E = \mu_0 M H[\sin\theta\cos(\phi - \phi_H)] + \frac{\mu_0}{2} M^2 \Delta N \cos^2\theta + \frac{K_1}{4}(\sin^4\theta \sin^2 2\phi + \sin^2 2\theta) \qquad (3.3)$$

where (θ, ϕ) define the position of $\vec{M}$ (inset in Fig. 3.43), and $\vec{H}$ is applied in the *xy* plane at an angle ϕ_H with respect to the [100] axis. From the conditions $\frac{dE}{d\theta} = 0$ and $\frac{dE}{d\phi} = 0$ we reach the corresponding equilibrium positions: $\theta = \frac{\pi}{2}$ and, by assuming $K_1/M << \mu_0 H$, $\phi = \phi_H$, thus indicating that $\vec{M}$ lies in the *xy* plane and that it is parallel to the applied field. Evaluating the second derivative of Eq. 3.3 at the equilibrium positions $\theta = \frac{\pi}{2}$ and $\phi = \phi_H$, and replacing the result in the Smit-Beljers equation [198], we obtain the FMR condition for our system of nanoislands:

$$\left(\frac{\omega}{\gamma}\right)^2 = \left[\mu_0 H + \mu_0 \Delta N\ M + \frac{2K_1}{M}\left(1 - \frac{1}{2}\sin^2 2\phi\right)\right]\left(\mu_0 H + \frac{2K_1}{M}\cos 4\phi\right) \qquad (3.4)$$

where ω/γ=0.34 T, $\omega = 2\pi\nu$ with ν=9.5 GHz the X-band microwave frequency used, and γ is the gyromagnetic factor for LSMO. The fitting of the experimental data to the Eq. 3.4 (solid line in Fig. 3.43) yields the values $\mu_0 \Delta N\ M(150\ K) = (0.393 \pm 0.004)$T and $2K_1/M(150\ K) = -(0.021 \pm 0.002)$T. Our numerical estimation of the flat pyramids' effective demagnetizing field gives $\mu_0 \Delta N\ M(150\ K) = (0.3 \pm 0.1)$T, where we have introduced the measured saturation magnetization at 150 K $M = 0.95 \times (465 \pm 70)$ kA/m, reduced a 5% from the 110 K value listed in Tab. 3.3 **. Thus both values compare well

**We did not take directly the M_S value at 150 K from the *M(T)* curve in Fig. 3.41 because it corresponds to a

and prove the validity of the assumptions made in the treatment. On the other hand, the value for the magnetocrystalline anisotropy constant K_1 is deduced from $2K_1/M$, giving $K_1(150K) = -(5\pm1)$ kJ/m^3. This result is in the order of what it is reported in literature for LSMO films grown along the (001) plane which show the [110] in-plane easy axis [90, 199]. To our knowledge, this is the first reported shape anisotropy study for LSMO nanoislands, along with the first measurement of K_1 in such nanoscale systems.

In conclusion, regarding the macroscopic magnetic properties of self-assembled LSMO nanoislands on YSZ, we have shown that the nanoisland ensemble exhibits clear ferromagnetic behavior, with in-plane anisotropy, saturation magnetizations not far from the reported LSMO bulk values (especially at low temperatures), and T_C∼350 K, i.e. well above room temperature, and close to the T_C∼360 K of bulk LSMO. Such values are not straightforward to obtain in sub-micrometer magnetic oxide nanostructures: on one hand, their processing relies typically on e-beam lithography and/or ion milling procedures, that were found to lower the T_C due to radiation damage and ion implantation [66]. The spontaneous self-assembly process described in this work avoids these detrimental effects. On the other hand, the influence of strain on the magnetic properties, widely claimed to cause lower T_C values, is also avoided: LSMO nanoislands show a highly crystalline strain-relaxed structure. We have also discussed the possible role of a ferromagnetic dead layer, which could account for the lowering of the magnetization signals measured in the nanoisland ensembles. Finally, we have analyzed the role of different magnetic anisotropy contributions in the overall anisotropy of the self-assembled LSMO system, which has been proved to display an in-plane $[110]_{\mathrm{LSMO}}$ magnetic anisotropy. This highlights the influence of the magnetocrystalline anisotropy (with $< 111 >_{\mathrm{LSMO}}$ easy axis), and that of the shape anisotropy, due to the platelet-like nanoisland shape. To the best of our knowledge, no LSMO nanoislands with lateral sizes below ∼200 nm and bearing the ferromagnetic properties presented in this work have been reported up to date.

3.5 LSMO on MgO

In the present section we investigate a different oxide heterostructure, again consisting of two very different compounds: perovskite type LSMO is now grown on MgO single crystal, a well known binary oxide with rocksalt structure. The difference in lattice parameter between LSMO and MgO results in a nominal tensile mismatch of +8.8%. Similarly to what we have seen concerning the LSMO/YSZ heteroepitaxy, a homogeneous dispersion of self-assembled nanoislands is also obtained for LSMO on MgO. However, and at variance with the previous case, the ferromagnetic nature of the LSMO nanodots appears now largely supressed. Also, the particular nanoisland self-assembly observed here, with nanoislands decorating MgO step edges, appears dominated by island-substrate interaction. In order to shed light into these facts, and further motivated by the intrinsic microstructural richness of this system, a detailed TEM characterization of the LSMO/MgO interface has been carried out in parallel to the present work, in the context of a recent PhD thesis within our group [160].

single sample. Rather than that, we used the *M(T)* curve to extrapolate the decrease of *M* with *T*, but taking the more realistic averaged value of M_S at 110 K from Tab. 3.3

3.5.1 General view of the system

Our knowledge of CSD-grown LSMO on YSZ paved the way for the fabrication of self-assembled LSMO nanoislands on MgO substrates. By using LSMO precursor solution concentrations in the range of 0.015 M to 0.06 M (in Mn), we achieved a homogeneous self-assembly of LSMO nanoislands on MgO, covering the whole 5 mm $\times$ 5 mm substrate. Fig. 3.44 shows the result after processing a 0.03 M LSMO precursor solution deposited on a MgO substrate at 900°C for 3 h. The 1 µm $\times$ 1 µm AFM topography image, in Fig. 3.44 (a), displays a high concentration of square and rectangular-base nanoislands, with thickness t typically below 10 nm and widths D in the 40-60 nm range. The area coverage for this sample is $\sim$35%. The amount of material calculated from AFM volume analysis is comparable to what we obtained from growing 0.03 M solutions onto YSZ substrates. This was expected, since identical spin-coating conditions were used, and the same wettability of the solution with respect to the MgO was measured (recall the Experimental procedure description in Chapter 2). Hence, the *Concentration* vs *Equivalent thickness* relation plotted in Fig. 3.20 equally holds for this system.

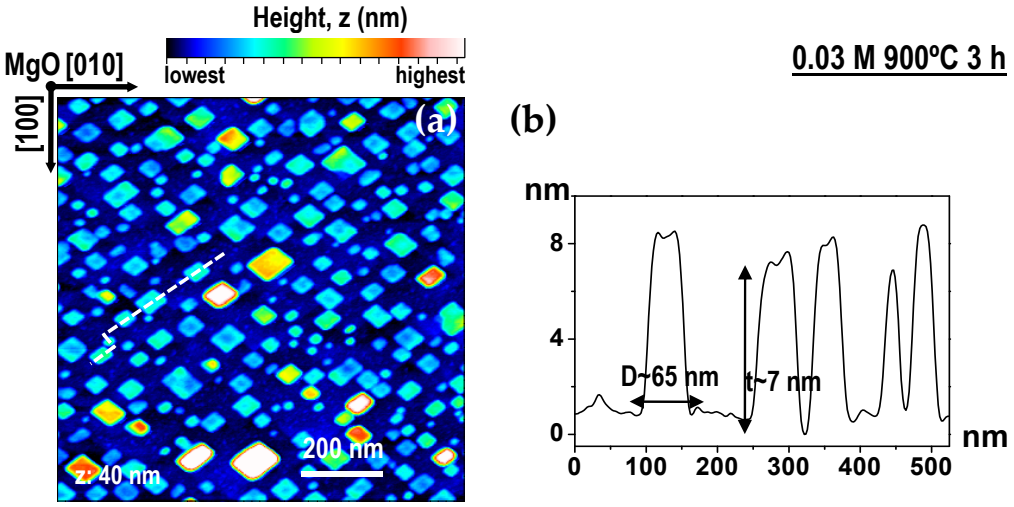

Fig. 3.44: *(a) 1µm $\times$ 1µm AFM topography image of self-assembled LSMO nanoislands grown on MgO from a 0.03 M solution, heat-treated at 900°C for 3 h. (b) Line profile corresponding to the dashed line in (a), showing the typical island sizes.*

A statistical study of nanoisland sizes gives the thickness t and lateral size D distributions plotted in Fig. 3.45 (a). Some very few islands ($\sim$3% in the AFM image of Fig. 3.44) exhibit t values of $\sim$30-40 nm. If we neglect them, the thickness distribution appears centered in $t\sim$7 nm values, with a remarkably narrow dispersion (a standard deviation of $\sim$2 nm is measured). The lateral sizes are in the order of $D\sim$50 ($\pm$20) nm, which gives aspect ratios of around $D/t\sim$7. These high aspect ratio values underline, once more, the tendency of solution-derived heteroepitaxial systems to give nanoislands with widths larger than thicknesses, a trend already highlighted in the LSMO/YSZ case. The Z-contrast STEM image in Fig. 3.45 (b) further illustrates the lateral size vs thickness relation. Recall that the intensity in a STEM micrograph is proportional to the Z atomic number of the imaged element (the higher the Z, the brighter the contrast). Nanoislands are thus seen as bright structures against the darker MgO substrate (Z_{La}:57, Z_{Sr}:38, Z_{Mn}:25 and Z_{Mg}:12).

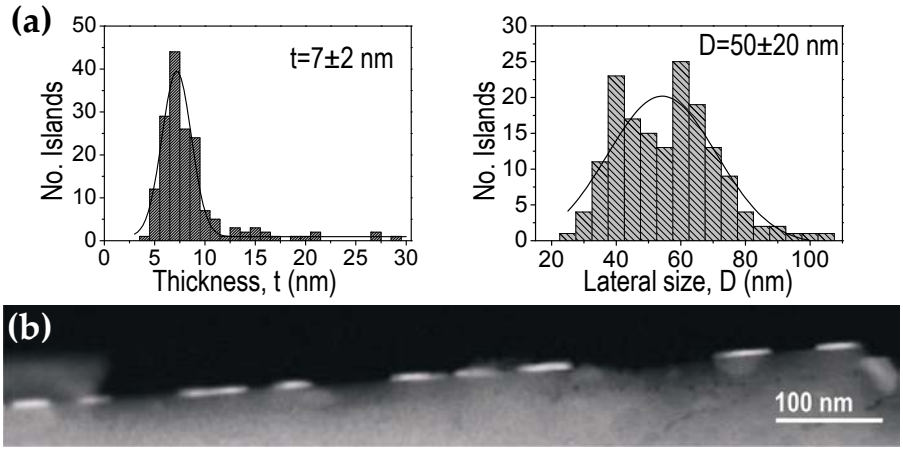

Fig. 3.45: *(a)* t *and* D *histograms showing the island size distribution. The values correspond to the sample shown in Fig. 3.44. (b) Low magnification STEM image showing 9 platelet-like LSMO nanoislands (in bright contrast). STEM image courtesy of P. Abellán.*

Crystallographic orientation

We combined XRD θ-2θ scans with pole figure measurements recorded with a 2D detector in order to assess the overall crystallographic orientation of the nanoislands. A $(001)_{LSMO}$ out-of-plane orientation emerges both from the θ-2θ scan and from the pole figure of the $(011)_{LSMO}$ reflection, which appears at χ=45°. From the simultaneous measurement of the $(111)_{MgO}$ reflection, rotated 45° in ϕ with respect to the $(011)_{LSMO}$ spots, we deduce that nanoislands withstand a cube-on-cube epitaxy, i.e. $(001)_{\mathrm{LSMO}}[100]||(001)_{\mathrm{MgO}}[100]$. It is with such interface arrangement that the lattice mismatch between islands and substrate is minimum (although still considerably high, $\sim$8.8%). Note that this epitaxial relation is general, i.e. we measured it for all LSMO on MgO nanostructured templates with solution concentrations ranging from 0.015 M to 0.06 M, and annealings from 1 h to 24 h at temperatures between 900°C and 1000°C. It is also worth noting that the LSMO poles [see Fig. 3.46 (b)] exhibit a large spread in χ, suggesting a certain degree of misorientation among the nanostructures.

As a matter of fact, by tuning the contrast and the intensity of the pole figure we can actually distinguish the fine structure, which consists of five well-resolved spots [Fig. 3.47 (a)]. We further performed a more detailed ϕ scan around a single $(011)_{\mathrm{LSMO}}$ reflection using smaller steps ($\Delta\phi$=0.5° instead of the standard $\Delta\phi$=2°). The result, plotted in Fig. 3.47 (b), unambiguously shows a central spot (corresponding to perfect cube-on-cube epitaxy) surrounded by four satellite peaks. The latter appear displaced, both in χ and ϕ, by 2°-5°, with the maximum intensity at a value of 4($\pm$0.5)° both for in-plane and out-of-plane disorientation values. A detailed HRTEM investigation of the LSMO/MgO interface has evidenced the presence of dislocations with Burgers vectors $\vec{b}=\frac{a}{2}[100]$ and $\vec{b}=\frac{a}{2}[001]$, producing a rough and defective interface [160, 200]. While $\vec{b}=\frac{a}{2}[100]$ dislocations accommodate the high nominal tensile strain between LSMO and MgO, it is demonstrated that the $\vec{b}=\frac{a}{2}[001]$ dislocations account for rigid body rotations of the LSMO nanoislands. In particular, islands with out-of-plane tilts of $\sim$2°, $\sim$4°, and a maximum of $\sim$5°, along with nanoislands with perfect cube-on-cube epitaxy (no rotation), have been observed [160]. A magnified view of the LSMO/MgO interface, including three dislocations, is shown in the HRTEM

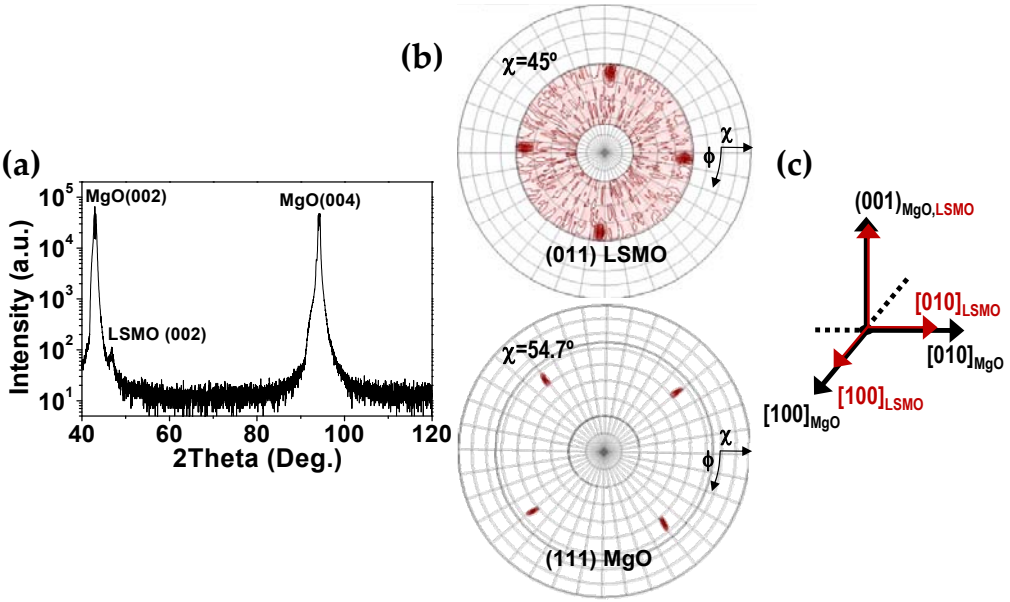

Fig. 3.46: *(a) $\theta - 2\theta$ scan of a LSMO nanoisland ensemble on MgO. The $(002)_{LSMO}$ reflection is observed at 2θ=46.9°. (b) Pole figure measurements of the same sample giving the in-plane cube-on-cube interfacial arrangement. (c) Schematic diagram of the LSMO on MgO heteroepitaxy. The sample measured in the figure was 0.03 M, heat-treated at 900°C for 1 h.*

micrograph of Fig. 3.47 (c). Note that No. 3 consists of two superimposed dislocations, i.e. $\vec{b}=\frac{a}{2}[100]$ and $\vec{b}=\frac{a}{2}[001]$, while each No. 4 and 5 only exhibit the strain-accommodating partial dislocation, $\vec{b}=\frac{a}{2}[100]$. The dislocations responsible for the out-of-plane tilt result in a net rotation about the in-plane <110> directions. This explains, by taking into account the two possible tilt senses, the four satellite LSMO poles detected in the pole figure measurements [200].

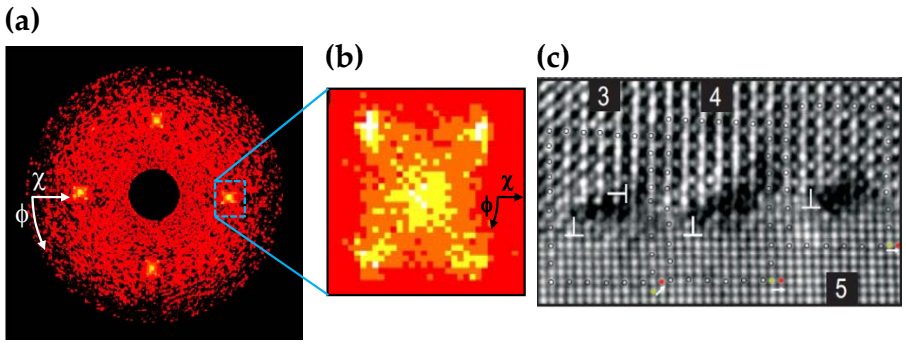

Fig. 3.47: *(a) $(011)_{\mathrm{LSMO}}$ pole figure. The step used was $\Delta\phi$=2°. (b) The phi-scan measurement of a single $(011)_{\mathrm{LSMO}}$ reflection, using a $\Delta\phi$=0.5° step, further reveals the fine structure of a single reflection, consisting of one central and four satellite peaks. The maximum intensity both in ϕ and in χ is measured at 4°$\pm$ 0.5°. (c) Detailed HRTEM image of the LSMO/MgO interface, featuring misfit accommodating dislocations (symbol $\perp$) and a dislocation responsible for nanoisland rotation (symbol $\dashv$). HRTEM image courtesy of P. Abellán and M.J. Casanove.*

Nanoisland morphology

Fig. 3.48 (a) shows the *Z*-contrast STEM cross-section image of a LSMO nanoisland on MgO, seen along the $[100]_{\mathrm{MgO}}$ direction (which is also the $[100]_{\mathrm{LSMO}}$ direction). The good crystalline quality is evident from the clear arrangement of the atomic columns within the island. Note that the brighter central part of the island, indicating a thicker specimen, is a consequence of the in-plane rotated-square nanoisland morphology [see Fig. 3.44 (a)]. Arrowheads point at surface steps, which adopt half unit cell heights at the nanoisland/substrate interface [160]. The top facet is clearly a $(001)_{\mathrm{LSMO}}$ plane, as expected from AFM topography images and XRD results. The projection of the lateral facets into the observation plane falls at 90° with respect to the substrate horizontal line. Two possible nanoisland shapes would yield this projection: either a *boxed-shape* island with $\{110\}_{\mathrm{LSMO}}$ lateral planes, or a *truncated pyramid* with $\{111\}_{\mathrm{LSMO}}$ oblique planes, truncated at the corners by $\{100\}_{\mathrm{LSMO}}$ facets. We have schematically illustrated both possibilities in Fig. 3.48 (b).

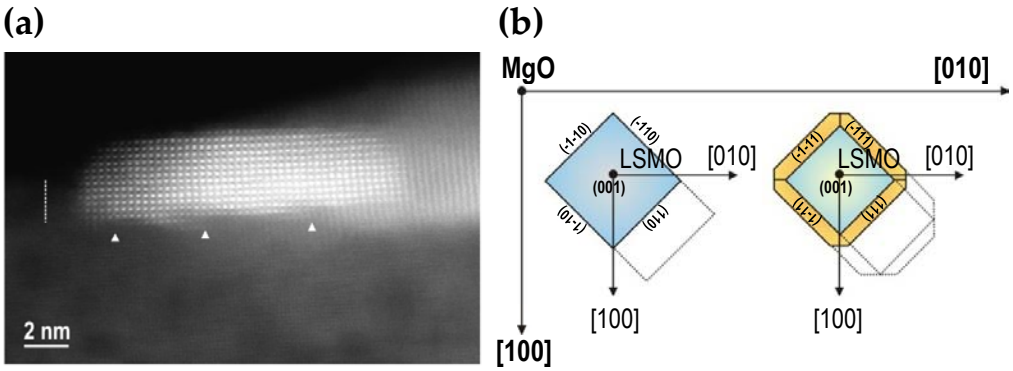

Fig. 3.48: *(a) HAADF-STEM image of a LSMO on MgO nanoisland viewed along the [100] direction. The arrowheads mark the substrate steps. (b) Sketch of the two possible island morphologies according to the STEM results. The epitaxial relationship and the nanoisland facets are indicated. STEM image courtesy of P. Abellán.*

Evolution of the LSMO on MgO nanostructured system. The role of the substrate morphology in the nanoisland self-assembly

In Fig. 3.49 we compare $5\ \mu\mathrm{m} \times 5\ \mu\mathrm{m}$ AFM images of two samples: one heat-treated at 900°C for 1 h, the other at 1000°C for 24 h. The solution concentration was 0.03 M for both. Analogous conditions resulted in a substantial evolution of the LSMO/YSZ system [recall Fig. 3.21, Fig. 3.23, and Fig. 3.29] but do not trigger a notable change in the present case. The area coverage is very similar, as well as the thickness distribution (*z* scale is around 60 nm). Nanoislands may appear slightly more rounded in the high *T* sample, which is expected from the enhanced atomic diffusion. If we look at the substrate surface in Figs. 3.49 (a') and (b') (by saturating the island contrast), we can see the effect of the different thermal annealings. Well-defined substrate steps are apparent in the 3D image of both samples. In Fig. 3.49 (a) the terraces along the <110>$_{MgO}$ directions feature sharp edges and kinks. These terraces are still observable in the sample of Fig. 3.49 (b), although they appear more rounded by the effect of atomic diffusion at high temperatures (a few have

been marked with white dotted lines). Note also that small square holes have developed, and that islands sit at their rims and at the terrace edges.

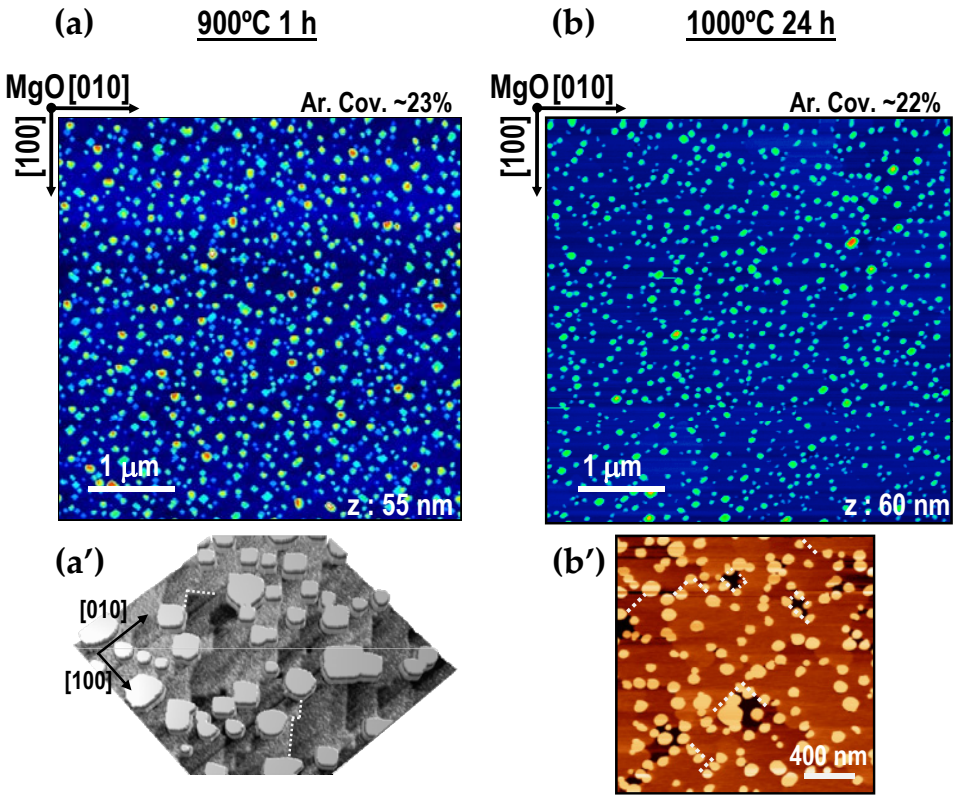

Fig. 3.49: *5$\mu m \times 5\mu m$ AFM topography images of LSMO on MgO self-assembled nanoislands resulting after (a) 900°C 1 h and (b) 1000°C 24 h heat treatments. Solution concentrations of 0.03 M were used. (a')&(b') 1$\mu m \times 1\mu m$ and 2$\mu m \times 2\mu m$ topography details of the step edges, aligned along the <110>$_{MgO}$ directions, showing the preferential location of nanoislands at step edges and rims.*

As we already stated in Chapter 2, upon thermal treatments at 900°C, MgO does not form well-defined steps. This is shown again in the AFM topography image of the bare substrate in Fig. 3.50 (a). After the deposition of 0.03 M LSMO precursor solution and the subsequent heat treatment (also at 900°C, but just for 1 h), however, a well defined step-terrace morphology develops, with the surface steps running along the <110>$_{MgO}$ directions. It is also worth emphasizing that samples featuring LSMO nanoislands grown at 900°C for 1 h on substrates with no previous heat treatment exhibit <110>$_{MgO}$ aligned steps in identical manner. At higher temperatures, as shown in Fig. 3.50 (b), terraces adopt a rounder shape at the kinks and edges but we may still detect the <110>$_{MgO}$ directions that they follow. In the 900°C 1 h sample we observe 0.5, 1, and 1.5 u.c. step heights which increase up to 5 and even 6 u.c. at high temperatures, due to step-bunching. Note how, in both cases, the observed step-terrace configuration is intimately linked to the distribution of the nanoislands, which preferentially locate at the kinks and terrace edges. See, for instance, in Fig. 3.50 (b), how the decoration pattern formed by nanoislands is determined by their positioning on top of substrate edges. Besides, in the totality of nanostructured LSMO on MgO samples processed at $T \leq 1000$°C (around 15), we always observed a rotated-square

island morphology, i.e. with its edges parallel to the substrate terrace edges. All of this is in remarkable contrast to what we discussed for the case of LSMO nanoislands on YSZ, where we saw the nanoisland disposition and morphology to be independent of the substrate step-terrace structure.

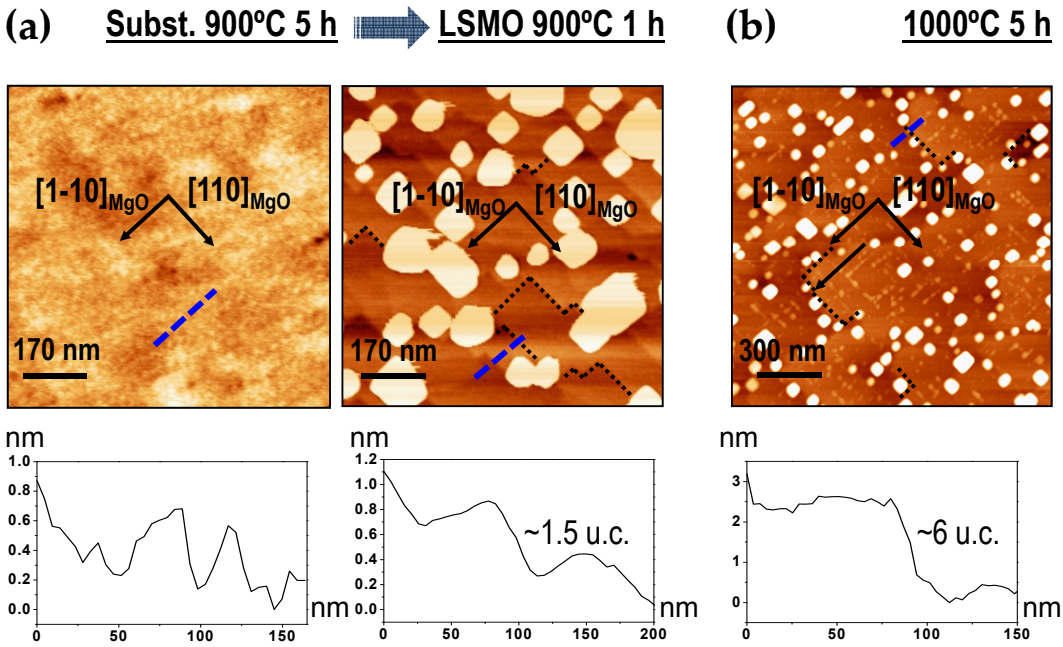

Fig. 3.50: *(a) MgO bare substrate after 900°C 5 h annealing under flowing oxygen (left), and after the subsequent deposition and growth of LSMO 0.03 M at 900°C for 1 h (right). The well-defined step-terrace morphology occurs only after the LSMO deposition. (b) Another sample after deposition of LSMO and annealing at 1000°C for 5 h. Square and rectangular-base nanoislands decorate the underlying step edges. Dotted black lines indicate some of the MgO terraces. The blue dashed lines correspond to the line profiles of the substrate steps below.*

The presence of sharp edges on the surface of substrates has been proved an efficient way of directing the self-assembly of nanostructures in heteroepitaxial systems. Nanoislands are seen to preferentially locate at those edges under specific conditions. These preferential location sites or *edges* can be found in naturally occurring surface steps [200], at the rims of holes...etc, or can be made deliberately by different lithography techniques [201], focused ion beam [202], or even using more exotic approaches like nanoindentation [172]. This provides for an effective strategy for the control of nanoisland positioning, as required in many nanotechnology applications. Lagally and co-workers explained these experimental facts by theoretically predicting the appearance of certain local energy minima at either concave or convex places of otherwise flat substrates [201]. A nanostructure may either relax or increase its elastic strain energy by locating at a curved site. The competition between this elastic strain relaxation and the interface energy of the nanostructure, both dependent upon the curvature of the underlying site, are at the origin of the appearance of the local energy minima, where nanoislands preferentially locate [201].

We now examine how the system behaves if we push it to temperatures as high as 1300°C for 5 h, as we did for the LSMO on YSZ self-assembled nanoislands in section 3.4.1. Fig. 3.51 reveals that for LSMO on MgO, the system undergoes a remarkable transforma-

tion. Note that the AFM image of Fig. 3.51 (a) is the same size as the images in Figs. 3.49 (a) and (b), 5 µm × 5 µm, but now it features very few and large triangular-base nanoislands (t∼60 nm, D∼380 nm) which stand on top of a leaf-like substrate surface pattern. This surface is far from atomically flat, featuring holes in the 5-15 nm range [see the line profile of Fig. 3.51 (b)]. Within the different 'terraces' perfectly squared holes develop, as expected from a cubic material, although these holes, remarkably, follow the <110>$_{MgO}$ directions. Note that, at lower temperatures, we have seen such orientations to be the ones adopted by terraces. Moreover, we have also identified the presence of small holes at 1000°C, which could be the precursors of the actual structures.

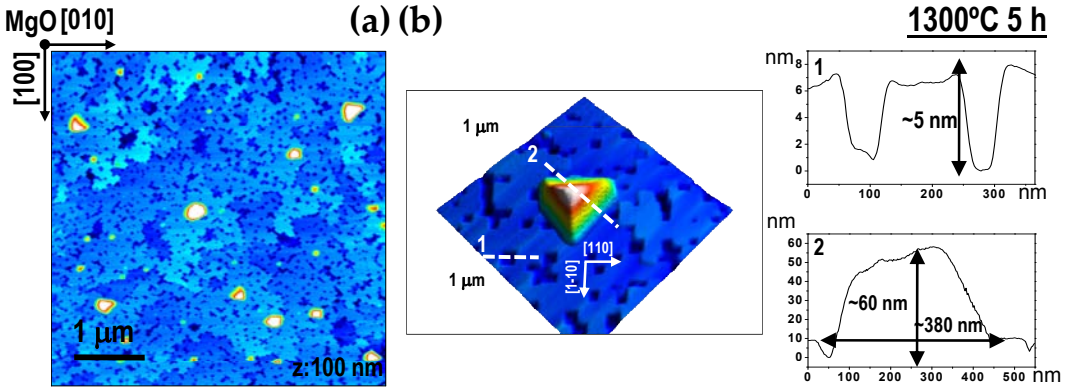

Fig. 3.51: *(a) 5µm × 5µm AFM topography image showing the transformation of substrate and LSMO nanoislands when the heat treatment (0.03 M solution) is performed at 1300°C for 5 h. (b) A 3D detail of a single island, as large as 380 nm in lateral size. The dashed lines numbered* 1 *and* 2 *correspond to the line scans on the right.*

The θ-2θ and pole figure measurements of the 1300°C treated system, displayed in Fig. 3.52, reveal that, despite the striking morphological difference, nanoislands hold the same epitaxial relationship as the LSMO on MgO nanoislands heat-treated at $T\leq$1000°C: they grow epitaxially and cube-on-cube on top of MgO. Due to their different shape with respect to the square islands discussed before, it follows that their facets are also different, which should be verified by TEM cross-section studies. It is also worth mentioning that, for these high T samples, the spread in χ of the LSMO poles is far smaller, as it is deduced from comparing the pole figures in Fig. 3.46 and Fig. 3.52. This result suggests that, after the 1300°C annealing, these new islands do not exhibit the 2° to 5° tilts.

Further experiments are needed to shed light into the striking morphological transformation we observe in the LSMO/MgO heteroepitaxy upon 1300°C annealings. MgO is thermodynamically stable at 1300°C and ambient pressure [203] and so it is in principle not expected that it should undergo such a change. Also, 1300°C were not enough to produce a comparable evolution of the LSMO/YSZ heteroepitaxy, despite in this case a chemical reaction was also involved. It would be thus necessary to investigate the intermediate stages between 1000°C (where no transformation is observed) up to 1300°C. Also it would be interesting to study the effect of these high T treatments on bare MgO substrates, in order to assess the role of the LSMO nanoislands on the observed transformation.

In summary, throughout this section we have shown the general features of self-assembled LSMO nanoislands on MgO. Compared to LSMO on YSZ, when grown onto MgO, nanoislands exhibit smaller sizes, with a majority of them displaying thicknesses below

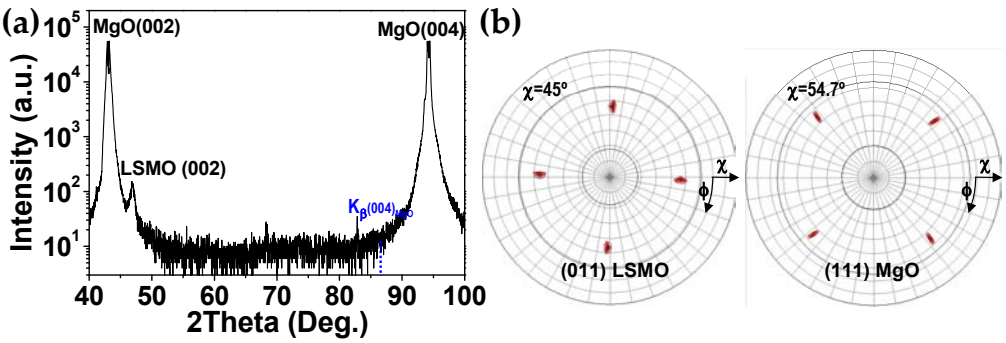

Fig. 3.52: *XRD study of self-assembled LSMO nanoislands on MgO, (0.03 M, 1300°C 5 h). (a) $\theta - 2\theta$ scan showing the out-of-plane $(002)_{LSMO}$ reflection. (b) Pole figures confirm the cube-on-cube epitaxial relationship.*

10 nm and lateral sizes in the ∼50 nm range. As already seen for LSMO/YSZ, LSMO on MgO nanoislands are also highly crystalline structures. They grow cube-on-cube, with a tendency towards out-of-plane tilting, as seen by X-ray pole figure analysis. In contrast to LSMO nanoislands on YSZ, which showed various morphologies, their shape when grown onto MgO is always the same, rotated squares with edges parallel to the substrate <110> step-edges. Moreover, nanoislands exhibit the tendency to locate on the these step edges. When subject to 1300°C the system undergoes a radical change, characterized by the morphological transformation of the substrate and of the islands, which exhibit very large sizes around t∼60 nm and D∼350 nm.

3.5.2 Magnetic properties

We have already anticipated that LSMO/MgO nanostructured templates exhibit highly supressed magnetic properties. This is in striking contrast with our findings concerning LSMO nanoislands on YSZ (see section 3.4.3). Fig. 3.53 displays the isothermal magnetization loops (field applied in-plane) for two identically grown nanostructured LSMO samples, one on YSZ (at 110 K), the other on MgO (at 77 K). The saturation magnetic moment, m_S, of the MgO sample is less than half the m_S value for the YSZ sample (∼1.7 $\times 10^{-5}$ emu against ∼4 $\times 10^{-5}$ emu). In terms of magnetization, the value for LSMO nanoislands on MgO is around M_S∼194±30 kA/m. This means a decrease in magnetization close to ∼60% with respect to LSMO nanoislands on YSZ [taking the averaged M_S value (0.03M, 110 K) in Tab. 3.3], and around ∼66% if we take bulk LSMO value at 110 K [19]. Note also that the MgO value in Fig. 3.53 was measured at 77 K, so it is expected to further decrease at 110 K, the temperature at which LSMO/YSZ was measured.

The temperature dependence of the magnetic moment for a system of LSMO nanoislands on MgO (0.03 M 900°C 3 h, full dots) is plotted in Fig. 3.54. For comparison, we also plot the temperature dependence of two bare substrates, a MgO and a YSZ single crystal, both heat treated at 900°C, the same as the LSMO/MgO nanostructured sample. The temperature dependence of the LSMO/MgO system shows no ferromagnetic behavior. On the contrary, it exhibits the same trend as the bare MgO substrate, with a paramagnetic to diamagnetic transition at around 50 K. The main difference between the two curves is a less negative (diamagnetic) signal in the case of the LSMO/MgO sample, which can be explained by the weak (and positive) ferromagnetic signal slightly shifting the magnetic

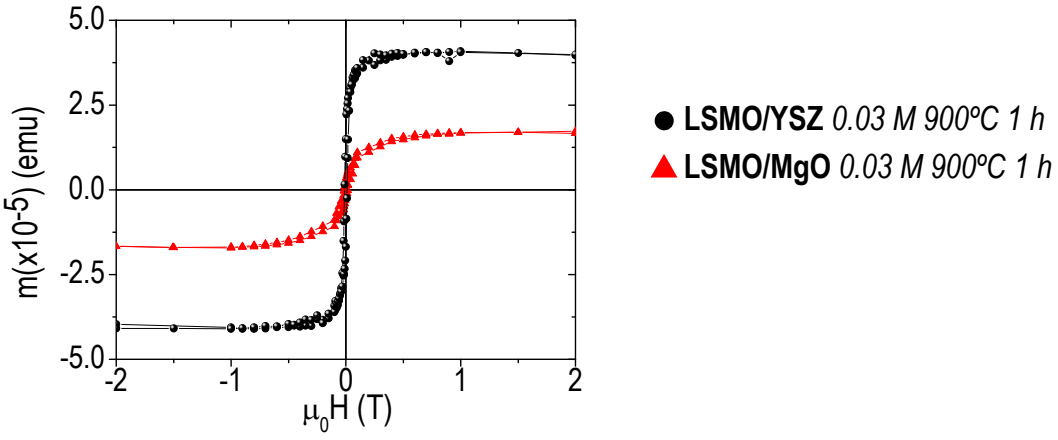

Fig. 3.53: *Isothermal magnetization loops for two identically grown LSMO self-assembled nanoisland samples, one on YSZ (at 110 K), the other on MgO (at 77 K). The latter shows a highly depressed magnetic behavior. Magnetic field was applied in-plane.*

moment with respect to the bare MgO substrate sample. Concerning the YSZ substrate, we measure a similar temperature dependence of the magnetic moment, although the diamagnetic signal at T∼250 K is around four times weaker than the diamagnetic signal of MgO (∼0.25×10^{-5} emu vs ∼1×10^{-5} emu, in absolute values). In conclusion, the low ferromagnetic signal exhibited by the LSMO islands on MgO, along with the large substrate diamagnetic signal, preclude measuring the collective FM behavior and thus the T_C value of the LSMO nanoislands on MgO.

Regarding the paramagnetic to diamagnetic transition measured for MgO and YSZ, it is worth noting that these single crystal substrates are known to contain several impurities such as calcium, aluminum, silicon, chromium or iron [204–207]. A recent work by Khalid and co-workers analyzes the paramagnetic and ferromagnetic signals measured in nominally diamagnetic single crystals, finding that the various impurities within the substrates account for such signals. In particular, for the case of MgO, they ascribe the low T paramagnetic signal of the temperature dependent magnetization to magnetic ions occupying lattice sites [208]. Whether the weak ferromagnetic signal measured in LSMO/MgO (Fig. 3.53) is solely the result of magnetic impurities within the MgO substrate is, however, unlikely. The M vs H behavior measured for bare substrates (not shown) did not give the ferromagnetic signal shown in Fig. 3.53. Also, the temperature dependence for LSMO/MgO of Fig. 3.54, although weak, shows a certain positive contribution not present in the bare MgO substrate.

3.5.3 Strain state of LSMO nanoislands on MgO

In section 3.3 of this chapter we already mentioned that the dependence of magnetic and electric properties with strain is a widely investigated issue, although still controversial in its application to the mixed-valence manganite compounds [22–25, 65, 162–165]. Therefore, the effects of accommodating a much higher lattice mismatch of ∼8.8%, which we have seen reflected in the highly defective LSMO on MgO interface, could be considered of relevance, regarding the supressed magnetic properties discussed in section 3.5.2. The XRD $\theta-2\theta$ scans of Fig. 3.46, with $(002)_{\mathrm{LSMO}}$ falling at 2θ∼46.9°, show that, overall, the

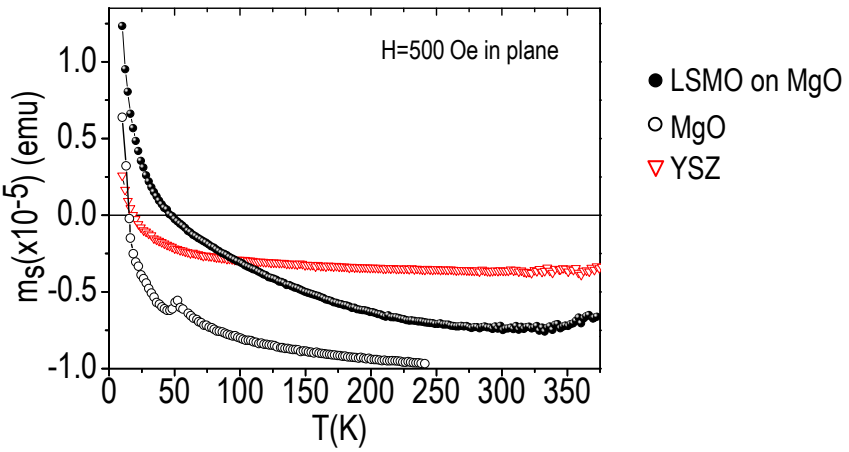

Fig. 3.54: *Magnetic moment as a function of T for: a system of self-assembled LSMO nanoislands on MgO (0.03 M, 900°C 3 h) (full dots); a bare MgO substrate (open dots); a bare YSZ substrate (open triangles). No ferromagnetic behavior is observed for the LSMO on MgO nanostructured system. Instead, we measure the substrates' dependence against T. A field of 500 Oe was applied in-plane in the three measurements.*

lattice parameter of the nanoislands is close to the bulk LSMO value, within the accuracy of our measurement (with error ∼0.2°, i.e. Δa_{LSMO}=±0.1 Å). This relaxation proceeds via a combination of mechanisms, the main being the introduction of misfit dislocations at the LSMO/MgO interface. For LSMO on YSZ we measured almost bulk-like magnetic properties in highly relaxed nanoislands. Nevertheless, nanoislands on MgO appear quite different from the previous case. They are very small and their defective interface therefore constitutes a higher fraction of the nanostructure volume. Detailed TEM investigations of the strain state, including the assessment of the strain fields around dislocation cores, were carried out in order to elucidate their possible impact on the suppressed ferromagnetic properties. We present here the main conclusions of these studies. The reader is directed to reference [160] for a more in-depth analysis concerning the TEM and STEM results.

Fig. 3.55 shows a HRTEM image of a LSMO nanoisland on MgO, and its corresponding ϵ_{xx} and ϵ_{yy} deformation maps, calculated using the Geometric Phase Analysis (GPA) method [209]; *x* stands for the direction parallel to the interface, and *y* for the normal direction. A mean variation of ϵ_{xx}=(-8.1±0.7)% between the island (in green) and the substrate (in red) in Fig. 3.55 (b) accounts for a change in the in-plane lattice parameter of ∼-8.1% between island and substrate. The negative sign points at a decrease in lattice parameter as we go from the substrate (which is taken as reference) towards the island. Considering a fully-relaxed LSMO nanoisland, its parameter variation with respect to the MgO substrate would take the value $(a_{LSMO} - a_{MgO})/a_{MgO}$=-8.1%, i.e. the same as experimentally measured. Similarly, the variation of the out-of-plane parameter displayed in Figs. 3.55 (c) and (e) also points at a complete relaxation within the measurement error [$\epsilon_{yy} = (-8.0 \pm 1.0)\%$]. In conclusion, our nanoisland is fully-relaxed. Additionally to the island relaxation, an island rigid body rotation (i.e. with no involved shear deformations) of 2.2° (±0.6°) was measured (also by GPA, not shown), a common feature of this system of nanoislands, as previously discussed. Finally, note the extreme color contrast variation (from blue to yellow) observed, regularly spaced, at the LSMO/MgO interface [Figs. 3.55 (b) and (c)]. These are the contrasts typically yielded by misfit dislocations.

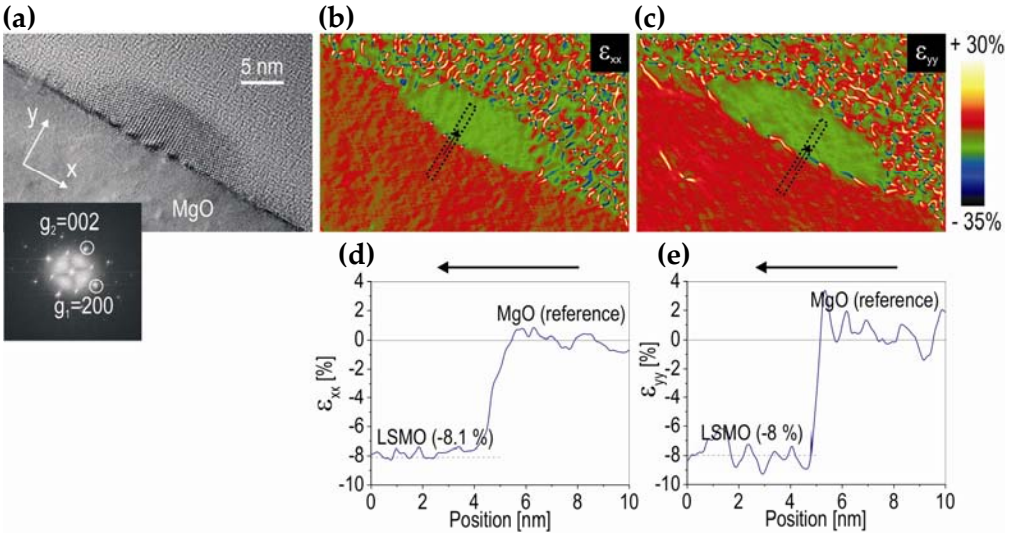

Fig. 3.55: *Strain state of a LSMO nanoisland on MgO assessed by the GPA method. (a) HRTEM image showing the source image for the strain maps calculation. The inset shows the Fourier transform of the image, indicating the (200) and (002) spots selected for the GPA analysis. (b)&(c)* ϵ_{xx} *and* ϵ_{yy} *deformation maps illustrating the in-plane and out-of-plane change in lattice parameter, respectively, by means of the abrupt color change from red to green. It is a negative variation, according to the scale bar, i.e. a compression. (d)&(e) The intensity profiles are calculated along the boxed regions marked in (b) and (c), and quantify the mean change in lattice parameters, in the order of* $\sim$*8%. Courtesy of P. Abellán.*

It is interesting to take a closer look at the strain field around the core of the misfit dislocations. By quantifying the extension of the deformation fields within the islands we can qualitatively evaluate their impact on the magnetization. It is known that the saturation magnetization M_S depends on the product $\lambda_S\sigma$, where λ_S is the magnetostriction constant and σ refers to the stress associated to the strain ϵ. In particular, M_S will tend to decrease if $\lambda_S\sigma$ is <0, and increase otherwise [210, 211]. Fig. 3.56 (a) shows a HRTEM image of a typical LSMO on MgO nanoisland with a number of dislocations at the interface. The relative deformation map (in %) of the in-plane lattice parameter with respect to the substrate associated to one of these dislocations (number *3*), has been calculated by GPA [Fig. 3.56 (b)]. The unstrained MgO substrate, taken as reference, features a green color, meaning $\epsilon_{xx}\sim 0\%$. The green to dark red region defines an in-plane lattice variation towards smaller values (compressive, <0). The greatest compression (-10% with respect to MgO) is around the dislocation core, where the extra half-plane resides. At a height of $\sim$1.5 nm from the core, however, the change in relative deformation is -8%, meaning that the bulk LSMO lattice parameter is recovered (i.e. relaxed structure). In width (direction parallel to the interface), the deformation field extends up to $\sim$1 nm. Opposite to the compressed core, on the substrate side, the light green to purple variation defines a tensile strain (σ>0). Contour lines indicate selected constant values.

Assuming that the measured deformation is purely mechanical (no chemical variations) the elastic stress σ can be inferred from Hooke's law, $\sigma_i = C_{ij}\epsilon'_j$ where C_{ij} (i,j=1,...6) are the elastic stiffness coefficients and ϵ' is the relative deformation of the LSMO lattice within the island with respect to the bulk LSMO lattice. Note that we have written ϵ' to avoid confusion with the macroscopic ϵ handled up to this moment, which accounts for

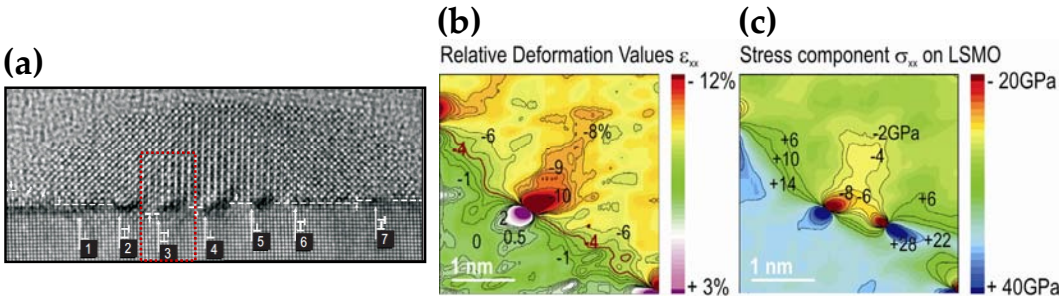

Fig. 3.56: *(a) HRTEM image of a LSMO nanoisland on MgO showing misfit dislocations (numbered) at the interface. (b) ϵ_{xx} deformation map around misfit dislocation number 3, boxed in (a) with dashed lines. Values are relative to the unstrained substrate. (c) σ_{xx} stress distribution of the same area. Note the presence of a stress center, adjacent to the one derived from the dislocation in (b). The source of such stress is another dislocation, now with the extra half-plane parallel to the interface [its presence is indicated in (a)]. Recall the dependency of σ_{xx} with the out-of-plane deformation , i.e. $\sigma_{xx}(\epsilon_{xx}, \epsilon_{yy})$. Courtesy of P. Abellán.*

the deformation of the lattice with respect to the MgO substrate. With the assumption of plane conditions (zero strain along the zone axis z direction) and taking into account that no shear strain was measured, the in-plane stress may be written as $\sigma_{xx} = C_{11}\epsilon'_{xx} + C_{12}\epsilon' yy$, where $xx \equiv 1$ and $yy \equiv 2$. Elastic stiffness coefficient values were taken from the literature for a slightly different LSMO composition ($La_{0.83}Sr_{0.17}MnO_3$) [212]. Full details of the derivation are given in [160] and references therein. The resulting stress map is displayed in Fig. 3.56 (c).

The magnetostriction constant λ_S for LSMO is positive for all temperatures until near T_C with a value $\lambda_S \sim 10^{-4}$ at 90 K [213] (recall that the LSMO on MgO hysteresis cycle plotted in Fig. 3.53 was measured at 77 K). In consequence, a possible degradation of M_S would be expected in the region featuring negative σ values of Fig. 3.56 (c) (where $\lambda_S \sigma < 0$). Such regions, assuming a similarly stressed behavior in the zone-axis direction (not measured) would amount to a volume of $\sim$1.5 nm^3 (1.5 nm$\times$1 nm$\times$1 nm). Considering the misfit dislocations present in a box-shaped LSMO nanoisland of the typically measured sizes, the total volume of the island which could be degraded would only account for the $\sim 4\%$ of the total volume. This seems far too small to justify the 60% magnetization loss measured by SQUID. The strain-induced defective LSMO/MgO interface may contribute to the decrease of M_S, but, in any case, as a secondary effect.

Numbers closer to the measured magnetic signals are deduced from considering the effect of a magnetic dead layer of $\sim$1-2 nm of thickness, surrounding both the nanoisland free and interface surfaces. For a boxed-shape island of typical sizes $t \sim 7$ nm and $D \sim 50$ nm, the amount of volume which would not contribute to the magnetic signal would be between $\sim 32\%$ and $\sim 55\%$, for 1 nm and 2 nm dead layer thicknesses, respectively[††]. Moreover, the presence of such dead layer could be related to a possible Mn-Mg interdiffusion between the nanoislands and the substrate. Indeed, Nakamura and co-workers have reported such interdiffusion in sol-gel derived $\sim$200 nm thick LSMO films, which results in a detrimental effect on the resistivity and magnetization behavior of the films with temperature [214]. Manganese and magnesium have similar ionic radii in octahedral coordination

[††]The dead layer (*d.l.*) volume was calculated by taking the whole area of the parallellepipedic island without the dead layer thickness, i.e. (t-2*d.l.*) and (D-2*d.l.*), and multiplying it by *d.l.*.

(around 0.8 Å) [215, 216], and, besides, it is well known that, within the LSMO lattice, manganese is the most mobile ion [217, 218]. From XRD and TEM studies we obtain that the LSMO nanoisland microstructure agrees with the expected lattice for LSMO, and, consenquently, in case of interdifussion, Mg should occupy the Mn sites as substitutional defects and viceversa [214]. To assess the hypothesis of interdiffusion in our LSMO nanoisland system and clarify its mechanisms, EELS local chemical measurements have been undertaken, in collaboration with J. Aguiar and Prof. N. D. Browning at UC Davis in California, USA. Preliminary results already indicate the presence of manganese within the substrate matrix, and hold promise for sheding light into the particular mechanisms responsible for the chemical interdiffusion and its subsequent impact on the magnetic properties.

3.6 Conclusions of Chapter 3

Throughout this chapter we have presented the main characteristics of the chemically grown LSMO nanoscale systems on perovskite type STO and LAO, on YSZ fluorite, and on MgO rock-salt substrates. Highly crystalline ultra-thin LSMO films below 10 nm of thickness grow onto the perovskite-type substrates, either strained (on STO) or relaxed (on LAO), but in both cases featuring high Curie temperature values T_C∼350 K. These values are very close to the reported bulk LSMO T_C, in contrast with the generally reported trend of depressed T_C for films of such thickness. Transport measurements in a set of varying thickness LSMO samples have shown totally insulating behavior in films with average estimated thickness of t∼3.5 nm. Conversely, a metal-insulator transition was found for films with average thickness above ∼5.5 nm, with the remarkable fact that this transition appears decoupled from the ferromagnetic to paramagnetic transition; we saw that while T_C is always around 350 K, the metal-insulator transition occurs at notably lower values, especially for thinner films. An Anderson type of 2D localization was mentioned as a possible mechanism leading to such behavior. Also, the thin LSMO films here reported showed increased MR values around ∼20%. Similar results have been reported in the literature for largely thicker LSMO nanocomposite films, and argued in those works in terms of structural and chemical disorder in such films. In our case, further investigations are required in order to shed light into the particular mechanisms behind these remarkable results.

The same growth procedure as in the perovskite case, but applied to YSZ and MgO substrates, results in highly uniform self-assembled nanoisland distributions. These nanoislands are crystalline, epitaxial, and present a highly relaxed microstructure attained through the introduction of misfit dislocations at the interface. LSMO on YSZ nanoislands show two main crystallographic orientations, a minority triangle-shaped $(111)_{\mathrm{LSMO}}$ and a majority $(001)_{\mathrm{LSMO}}$ population. The latter population shows two possible morphologies, regular or rotated-square, indicating the similarity of the LSMO facet energies. This is not the case for nanoislands on MgO, which invariably exhibit a rotated-square shape. The nanoisland shape on MgO substrates appears closely related to the substrate morphology, displaying edges parallel to the substrate step edges, along the <110>$_{MgO}$ directions. Nanoislands further show the interaction with the underlying MgO by preferentially locating at the rims of the substrate step terraces. Also, they tend to exhibit out-of-plane tiltings, which is the result of the dislocations found at the LSMO/MgO interface. The magnetic properties of nanoislands on YSZ are the best among the different systems analyzed, featuring the highest magnetic moments, and a T_C comparable to bulk LSMO values. The magnetic anisotropy axis was calculated to be the $[110]_{\mathrm{LSMO}}$, with a magnetocrystalline anisotropy

constant value K_1(150 K)=(-5$\pm$1) kJ/m^3, as measured, for the first time, in LSMO nanoislands. Conversely, LSMO on MgO nanoislands show very faint magnetic signals. We discussed the possible impact of the strain around the misfit dislocation cores on the magnetic properties of the system, concluding that it cannot account for the registered magnetic signal loss. We then argued that a 1 nm to 2 nm thick dead magnetic layer can better explain the suppressed magnetization values. Furthermore, preliminary local chemical analysis indicate a Mg-Mn exchange between substrate and nanoislands, pointing at the potential key role of chemical interdiffusion on the depressed magnetic properties.